Near-field Examination of Sonic/Supersonic Nozzle Flows

A thesis submitted in partial fulfillment of the requirements

for the Degree of

DOCTOR OF PHILOSOPHY

in

Mechanical Engineering

by

ALI JRAISHEH

Under the supervision of

Prof. Vinayak N. Kulkarni

Department of Mechanical Engineering

Indian Institute of Technology Guwahati

Guwahati - 781 039

May 2023

"Stop trying if you want a flawless life ..."

Dedicated to

My Parents, *Brother*, *Sisters* and *My Lovely Wife*

CERTIFICATE

This is to certify that the work presented in the thesis entitled "**Near-field Examination of Sonic/Supersonic Nozzle Flows**" submitted by Ali Jraisheh to the Indian Institute of Technology, Guwahati for the award of the degree of Doctor of Philosophy in Mechanical Engineering is a bona fide record of research work carried out by the student himself under my supervision and have not been submitted elsewhere for any degree or diploma.

Signature: Date:

Supervisor: Prof. Vinayak N. Kulkarni
Department of Mechanical Engineering,
Indian Institute of Technology Guwahati,
Guwahati-781039, Assam, India.

ACKNOWLEDGEMENT

The road we walk is what defines us on the long run, and my road during Ph.D. has been enjoyable, informative, as well as tough. I got to know a lot of people who have helped me be where I am today. Of course, I cannot remember each one of them, but I will try to mention the most impactful.

As sir Issac Newton once said: "If I have seen further, it is by standing on the shoulders of giants." The journey would have been a lot more difficult without Prof. *Vinayak Kulkarni*, who has been a supervisor of my Ph.D. thesis and a big brother for life. His continuous guidance and support were unlimited, and I consider myself extremely fortunate to have met him and worked under his supervision. I extend my appreciation to my mentor back home, Prof. *Hussain Teneh* for his continuous support during my higher studies. He has been an inspiration to me.

I am profoundly thankful for my Doctoral Committee members, Prof. *Ujjwal K. Saha*, Prof. *Pugazhenthi G.* , and Dr. *Dipankar N Basu*. Their insights and constructive comments had an important role in shaping this thesis since the beginning. I had the chance to know Prof. *Ganesh Natarajan* who has extended his help whenever I asked for it, I appreciate his comments to lift the quality of my work. I would also like to appreciate the efforts extended by the Heads of Department during my stay as a Ph.D. student in the department of Mechanical Engineering, Prof *S. K. Dwivedy*, Prof *S. Senthilvelan*, and Prof *K. S. R. Krishna Murthy*, for their dedication for the betterment of the department.

A sincere gratitude is in order to **Damascus University**, the historical organisation that has stood up to every challenge during this vicious war. I am forever grateful for the financial and moral support throughout my stay in India. I would also extend my emotions to my people, the **Syrian people**, they have suffered from ungodly war, and yet were still able to carry on with their lives. I am so proud to have come from such a beautiful place, and I hope peace will find us some day.

When I first arrived to India, I was greeted with the proverb "**Atithi Devo Bhava**", which means "**The Guest is God**". I am still trying to lift myself up to this wonderful greeting, even though after getting to know the real India, I have become one with the people, and I do not want to be a guest anymore, even if this means I am no longer a God. So, this amazing country has embraced me with all my flaws, the people here have been a family for me when I was thousands of miles away from my family. My only hope is that I was a good son of this family, and I know I will never be able to return the favour.

Throughout this journey, I have met a lot of people who have, in many ways, directed my path towards this point. I had the chance to be a part of a great Syrian group on campus, my friends, *Malek, Sami, Moustafa, Ghadir, Mohamed, Nour, and Juana*, all have been a wonderful comfort zone for me. They were the pillar I leaned against when I was in despair, and the cheerful little community to which I escape from all the stress. Special thanks to Dr. *Azd*, who was an inspiration for me during my stay in India, he never failed to support and guide me towards doing the right thing. It is very rare to meet such a great person like *Shuvayan*, he was the first close friend in India. He never saw me as a junior in the lab, rather a friend and a companion. I appreciate his patience and continuous motivation, in both academic life and Basketball games which I totally won. The small Post Graduate lab has given me the chance to meet *Jubajyoti* and *Amrita*, my dear Assamese team while facing all the computational difficulties. I appreciate the lectures of *Jubajyoti* about how to write a code and actually make it work, and I will truly miss every trip we took to that dhaba. Although I do not agree with all the medical prescription of *Amrita*, but I really admire your care and thoughtfulness. I will always remember *Saswati*, who has introduced me to the Assames and Rabha cultures, and was a true, dedicated friend in spite of all the responsibilities she had carried. I wish her all the happiness in her life. I will always remember *Krishan*, he was sitting in my usual spot in the class, and little did I know that irritating coincidence would produce such an honest friendship. I am deeply thankful for *Siddesh*, who has never forgotten the little Syrian he left behind in the lab, it is always wonderful to receive his call and know that he is there for me. There are friends who have grown with me since my childhood, and I fail to tell them apart from my real family. I am deeply grateful for having *Rida & Ammar* in my life, although life has set us apart, but we always get together on those group calls like we are still in the same school. I hope that one day we will be able to reunite and be stupid like we used be. I will always be connected in my heart to *Wessam* no matter how far we are apart, he and his family were the closest thing to my own family. I will never be able to return your favours. Although we do not talk more often, *Ali Mohammad* will always be my roommate and brother, the friendship we have formed throughout the college days will never be limited to time and space. I got the chance to meet *Mahmoud* many years ago, and I still remember every night-out we had, he was the first one to receive me from the airport and see me off when I left. I wish you a great and happy life with *Loreen* and your amazing kids.
I met people from all over India, from different and diverse cultures, they were all equally beautiful and sweet. I cannot mention all the names in one thesis, all the mess workers, the canteen owners, and the sabji sellers, the people who received me as one of them, you will always be in my heart.

I come from a simple and loving family, their unconditional love was the direct reason for my achievements. I am profoundly thankful for being the son of *Yakoob & Najwa*, together they have made a miraculous small family, and I hope that I have been up to your

expectations. My sisters, *Farah, Kinda & Aya*, have provided the love to light my heart, their calls gave me the energy to carry on, no matter how difficult the road was, I am in your debt forever. There are no words in the entire world to describe my love to my brother *Essa*, he was a role model for me, with all his patience, love, commitment, and heart. I am deeply grateful for your support since I was a small kid who did not know how to go to school without you. I wish you a great life with the lovely *Heidi*. I was lucky to have my wonderful in-laws, *Mohammad & George*, we are blessed to have you as part of our little family. I am also immensely happy to be part of my second family, *Rand, Zeina & Ahmad*, they took me as one of them and were equally loving and supportive.

I kept the last acknowledgment to my loving wife, *Nouma*, as her love will always remain in the bottom of my heart. She was the one who supported me, stood by me, believed in me, and most importantly, loved me for who I am. I adore everything about you, all the smiles you put on my face, all the butterflies you made me feel in my heart, and all the delicious food you prepared. I cannot imagine my life without you, and I hope we will be together through thick and thin.

Ali

ABSTRACT

This thesis presents a numerical study on compressible flow within and downstream sonic/supersonic nozzles. It is a close look on the effects of thermodynamics and geometry configuration on the gas flow inside and downstream the ducts. An in-house CFD solver is developed to accommodate the complex flow structure that accompanies the underexpanded jet and impose the proper boundary conditions, in order to simulate the flow field. More focus is drawn to the phenomenon of Mach disk that occurs in case of highly underexpanded flow, its location and height are thoroughly studied and analysed.

In order to more comprehend the factors that influence the freejet, it seemed only plausible to understand the alteration in jet structure with varying upstream geometries. Therefore, nine nozzle shapes are examined in terms of Mach disk location and height, and the resulting sonic line at the nozzle throat. This investigation provides an understanding to the influence of sonic nozzle geometry, and settling chamber over the jet structure, regardless of the viscosity effects. Hence, the inviscid Euler equations are employed for this purpose.

Further, an optimisation algorithm is deployed to construct a supersonic nozzle wall shape that produces a radially-uniform flow at the exit, and for the maximum distance downstream of the exit. Three different nozzle shapes are obtained depending on the mathematical representation of the nozzle wall, the wall shape is found to significantly impact the flow field and its characteristics within and downstream the nozzle. The most feasible nozzle is then fabricated and used in physics-related experiments. The growth of shear layer is also examined, and it is linked to the nozzle wall shape and gas properties.

Moreover, a novel arrangement for an altitude compensating nozzle is proposed to address the problem of operation under different pressure ratios. The idea is to replace the conventional nozzle with a set of parallel rings that would eventually form a supersonic nozzle with bleeding slots. This arrangement is found to be effective in eliminating the low-momentum part of the boundary layer, and maintaining a radially-uniform flow at the nozzle exit, in addition to its ability to alter the nozzle area ratio so that it operates at different altitudes.

It is concluded from the simulations results that sonic and supersonic freejets are widely governed by the thermodynamics properties of the fluid, and the geometrical constraints imposed on the flow. Freejets are found to be sensitive to these factors, and the CFD solver used herein can be a valuable tool to evaluate the complex structure of such flows and a significant addition to the ocean of supersonic flow.

CONTENTS

LIST OF FIGURES

LIST OF TABLES

CHAPTER 1

INTRODUCTION

The rapid advancement in the field of compressible flow has opened vast doors for technology to develop many tools that serve the human and humanity. The freejet, in particular, has been a subject of interest for scientists and researchers from different backgrounds, due to the role it plays in their respective fields.

1.1 Applications of freejet

High-speed gas flows are not limited to specific fields, they have applications in a myriad of areas for scientific and technological advancement. It is found that cooling the spectroscopic sample is an effective solution to obtain highly-resolved molecular spectrum [1]. The process is desired to keep the sample in the gaseous phase and bring to a temperature far below the boiling point. Expanding the gas through a nozzle does not only cool the sample to the desired temperature, but it also converts the random motion, that characterises the hot particles, into well-known directed motion downstream of the nozzle exit. The absorption technique of millimeter wave freejet is also useful in obtaining spectroscopic information on complex molecules in a simple way [2]. Figure 1.1 shows a freejet facility with the supersonic nozzle used to produce a uniform gas flow for spectroscopic purposes.

Moreover, freejets are prominently considered in integrated thrust-vector control [3–5], as they are believed to assist atmospheric flight with air-breathing propulsion systems as well as rockets, launch vehicles, and other space systems. Figure. 1.2 shows a Lockheed F-16 aircraft equipped with Multi-Axis Thrust Vectoring (MATV) and Advanced Vectoring Engine Nozzle (AVEN) taken from [3]. These flows are evident with high-speed aerodynamic testing facilities, and the supersonic nozzles are an important integral part of such facilities [6–8]. Further, freejet expansion along with laser technology were recognised for their potential in studying the structure and reactivity of short-lived chemical intermediates [9]. Freejets are able to cool the intermediates to very low temperatures, so that even complex organic free radicals and molecular ions can be identified and characterised [10]. Since jets are integral

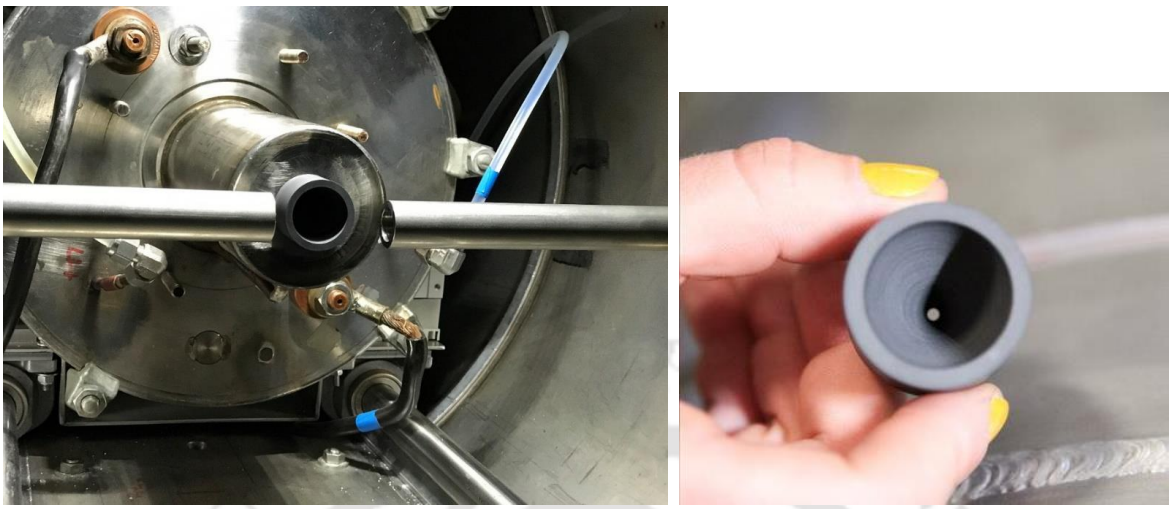

(a) (b)

Figure 1.1: An experimental apparatus for freejet facility: a) The settling chamber and b) The used nozzle.

part of many studies and facilities, it is desirable to understand its structure, and also the design methodology of nozzles which are employed to attain high-Mach number uniform jet. Therefore, this thesis focuses on exploring these flows and understanding the effects of multiple factors, i.e. boundary conditions and geometrical constraints, on the structure and evolution of such jets.

1.2 Dynamics of the freejet

The presence of the freejet in different academic and industrial sectors has made it an interesting topic for the researchers to run a lot of ink. In general, freejet can be defined as the part of the fluid flow which is unbounded by physical boundaries. The literature has intensively elaborated that the main driving factor of the jet structure is the pressure ratio [11–20], be it the exit pressure ratio or the total pressure ratio. Here, total pressure ratio is the ratio of total or stagnation pressure (reservoir pressure) to the back pressure (ambient pressure), whereas exit pressure ratio is the ratio of the pressure at the nozzle exit to the back pressure. It is to be mentioned that total pressure and nozzle exit pressure are related with the isentropic relations through the known Mach number at the exit (Eq. 1.1). Hence, both pressure ratios can be used in the calculations.

$$\frac{P_0}{P} = \left(1 + \frac{\gamma - 1}{2} M^2\right)^{\frac{\gamma}{\gamma - 1}} \tag{1.1}$$

where P_0 is the total pressure, P is the static pressure, γ is the ratio of specific heats, and M is Mach number.

The underexpanded condition of a jet [21] is evident when a gas is released into a receiver,

Figure 1.2: Lockheed Martin F-16 Vista Multi-Axis Thrust Vectoring (MATV) with Advanced Vectoring Engine Nozzle (AVEN) nozzle (taken from [3]).

and it attains higher pressure, at the duct exit, than the receiver pressure, which creates a state of pressure imbalance. Hence, the process of equilibrium takes place out of the nozzle by forming an expansion fan on the nozzle or orifice lip to balance the jet pressure with the ambient pressure. Therefore, the flow continues to expand even after exiting the nozzle or orifice to achieve a balanced state with the ambient pressure. The expansion waves, however, reflect from the free boundaries as weak compression waves coalescing to generate an incident oblique shock, or a barrel shock. However, the gas within the jet continues to expand by decreasing its pressure and increasing its Mach number. Figure 1.3 shows a moderately underexpanded jet, where the diamond or "X" pattern is observed due to regular reflection of the oblique shock. In this figure, (1) is the jet boundary which confines the flow, (2) is the line of pressure equilibrium from which the expansion waves reflect as compression waves, (3) is the reflected shock, (4) is the group of expansion waves which is generated at the nozzle lip, and (5) is the oblique (incident) shock.

When the driving pressure ratio of the jet becomes very high, the flow attains a very low pressure during expansion that cannot be balanced with the ambient pressure by an oblique shock. Hence, a normal shock (also called as Mach disk) appears within the jet to bring the jet pressure up to an adequate value. Figure 1.4 is an illustration for the highly underexpanded jet. In this case, the regular reflection is not enough to achieve a state of equilibrium, and therefore the normal shock or Mach disk (5) is present in the flow field. The presence of Mach disk subsequently leads to appearance of the triple point (8) and slip line (6). At the triple point, Mach disk, oblique shock and reflected shock intersect, while the slip line separates supersonic and subsonic zones downstream of the Mach disk. The shock cells are still visible at this level of underexpansion.

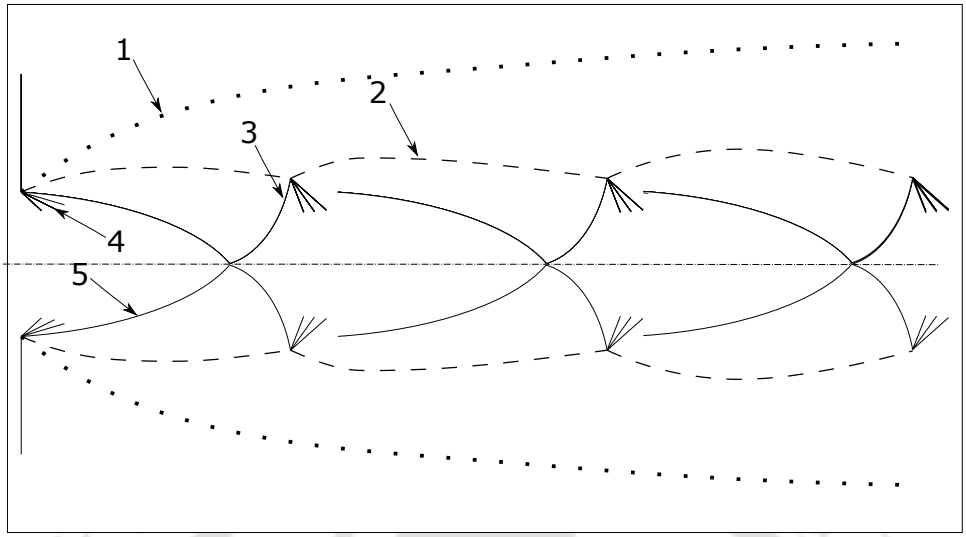

Figure 1.3: The elements of moderately underexpanded sonic jet: (1) jet boundary, (2) pressure equilibrium line, (3) reflected shock, (4) expansion waves, (5) oblique shock.

If the exit pressure ratio is further increased, the consequent jet is termed as extremely underexpanded jet. Figure 1.5 shows such extremely underexpanded jet where the shock cell pattern disappears and the jet becomes entirely a single shock cell structure with a barrel shock, terminated by a Mach disk. Inside this cell, supersonic flow further expands to high Mach numbers.

1.3 Special features of the Freejet and their prediction

Considering the importance of the underexpanded jet in various fields of science and engineering, it attracted the researchers to study different aspects of such jets. A hypothesis of Adamson and Nicholls [11] has suggested that the flow pressure behind the Mach disk almost matches the ambient pressure, and the flow over the axis of a sonic free-jet is similar to the gas expansion in an actual diverging nozzle. Many attempts are reported to construct correlations for the flow features in the near field of the jet, such as the location and height of Mach disk. Some experimental [16, 17, 22–25] and computational [26–29] investigations are part of open literature which help to measure or predict the distance between the nozzle exit and the Mach disk (also known as Mach disk location), and all agree that the exit pressure ratio has the major influence on it.

An experimental and computational work by Wilkes et al. [30] has considered the nitrogen sonic freejet, where planar laser-induced fluorescence (PLIF) method is used to non-intrusively visualize the jet flow. In this phase, the experimental results were compared with the computational results obtained using General Aerodynamic Simulation Program (GASP) in terms of the height and location of Mach disk and the jet wavelength. The wavelength of the jet is defined as the axial distance from the expansion wave at the nozzle lip to the next

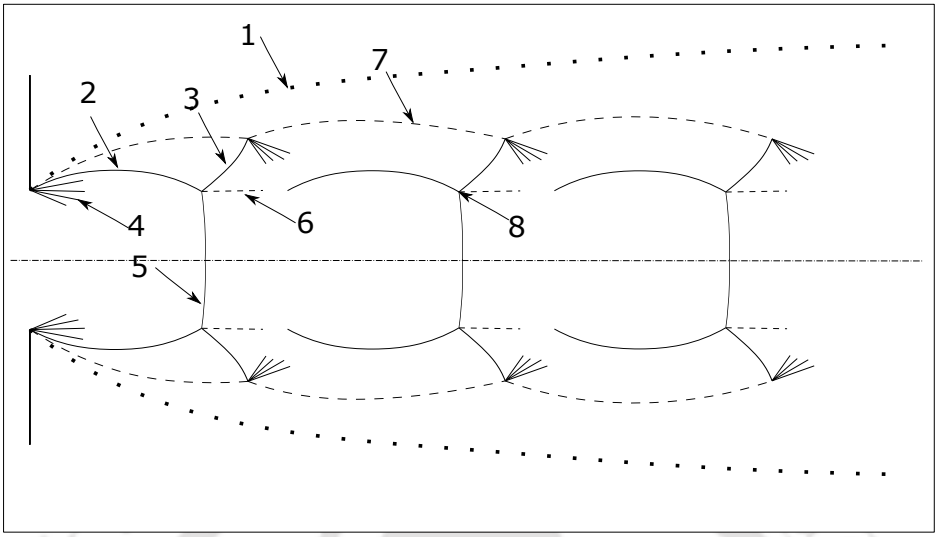

Figure 1.4: The elements of highly underexpanded sonic jet: (1) jet boundary, (2) oblique shock, (3) reflected shock, (4) expansion waves, (5) Mach disk, (6) slip line, (7) pressure equilibrium line, (8) triple point.

expansion fan after the reflected shock. Driftmyer [31] has conducted many experiments on sonic and supersonic nozzles taking into account several Mach numbers, exit pressure ratios and nozzle widths. Based on the experimental measurements varying from $P_0/P_b = 29.4$ to $P_0/P_b = 915.6$ for air, (Eq. 1.2) is suggested to predict the location of Mach disk:

$$\frac{X_M}{D} = (\frac{1}{j+1}\gamma M_e^2 \frac{P_e}{P_b})^{\frac{1}{j+1}} (\gamma M_e)^{j-1} \tag{1.2}$$

where j takes the value of 0 for 2-D flows and 1 for axisymmetric flows, X_M is the distance between the nozzle exit and Mach disk, D is the nozzle diameter, P_e and P_b are the exit and back pressure, respectively, and M_e is the exit Mach number.
Further, Addy [12] has carried out experiments on sonic orifices with various shapes, total pressure ratios and Reynolds numbers. It is evident that jet structure is influenced by the shape of the nozzle as it affects the expansion trend and possibly forms shock waves. Subsequently, two empirical relations were proposed to estimate Mach disk diameter for both, converging contoured sonic nozzle in (Eq. 1.3), and sharp edge sonic orifice in (Eq. 1.4):

$$\frac{D_M}{D} = 0.36(\frac{P_0}{P_b} - 3.9)^{0.5} \tag{1.3}$$

$$\frac{D_M}{D} = 0.31(\frac{P_0}{P_b} - 5.0)^{0.5} \tag{1.4}$$

where D_M is the diameter of Mach disk and P_0 is the total pressure.
It is noticed that Eqs. (1.3) and (1.4) do not explicitly include the nature of the gas. How-

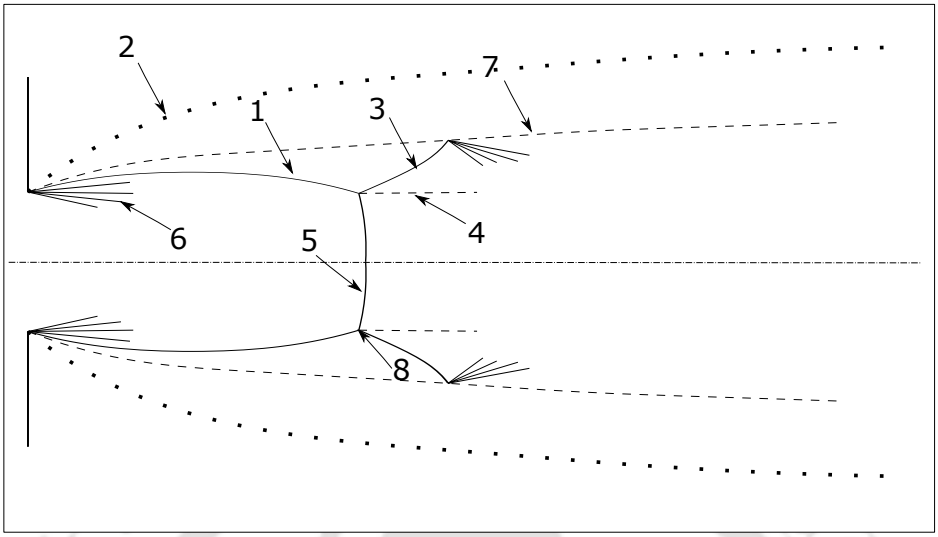

Figure 1.5: The elements of extremely underexpanded sonic jet: (1) oblique shock, (2) jet boundary, (3) reflected shock, (4) slip line, (5) Mach disk, (6) expansion waves, (7) pressure equilibrium line, (8) triple point.

ever, since these formulae deal with the total pressure ratio (P_0/P_b), the specific heat ratio (γ) is implicitly included since it is essential to convert the total pressure ratio to exit pressure ratio. Thus, the variation of gas properties affects the location and height of the normal shock as well as the free boundaries of the jet.

It is known that there are different flow features in the near-field region of the jet, corresponding to the level of underexpansion, and it becomes necessary to address the flow properties which influence these elements. The work done by Otobe et al. [32] mentions the importance of the nozzle shape in the case of the sonic freejet and suggests that viscosity has a negligible influence on the jet structure and boundaries in the near-field area. Although some researchers [15, 16, 33, 34] pointed out the independency of Mach disk location from the flowing fluid, γ can be explicitly seen in the Eq. (1.2), which has to be deliberately inspected for the location and height of Mach disk. Moreover, the role of reservoir or stagnation temperature in driving the jet structure is merely brought up in the literature, and it is necessary to be include in the literature. Moreover. first cell or the area between the nozzle exit plane and Mach disk is of specific interest for spectroscopic applications. Potential core resides in this region and it is laterally confined by the shear layer and the barrel shock, and axially by Mach disk. In this area, the flow can be treated as an inviscid compressible flow. The importance of this area comes from its low density, temperature and pressure values, which is convenient for physical aspects such as spectroscopy. It is observed in the works of Aniskin et al. [35, 36] that the inviscid area shows an interesting growth in the case of micro-jets or micro nozzles. However, the information related to regular nozzles are limited to the measurements of the distance between Mach disk and the nozzle. Hence, it becomes important to study the jet boundaries and the area limited by the shear layer for macro jets. Wilkes et al. [30] have explicitly mentioned that they used a laminar model to simulate the

free underexpanded jet, however, the turbulence effects might alter the location and height of the shock wave by the means of dissipation and diffusion. Thus, another important aim is to inspect the impact of turbulence on the near-field area.

1.4 Upstream geometrical configurations

Sonic jet has drawn the interest of many researchers [13, 15, 37–41] in the past century for its importance and involvement in engineering applications like physics [42], chemistry [43], and rocketry [44, 45]. As mentioned previously, the main parameter that governs the jet structure is the pressure ratio[12, 31, 40]. The influencing parameters also include the ratio of specific heats (γ) [41].

Although the flow and gas parameters play an important role in determining the jet shape, the upstream geometrical parameters are also seen to have an impact on the gas flows [27, 46]. Therefore, it has become a necessity to address the effects of the nozzle geometry on the underexpanded sonic jet. Aleshin et al. [47] experimentally studied the effect of cone angle and degree of contraction on the structure of underexpanded jet. They found that Mach disk diameter decreases as the cone angle increases from 5 to 60 degrees, then the diameter remains constant. Further, the maximum height of the first cell in the jet was not significantly influenced by the cone angle. However, they deduced that conical angle of a contracted nozzle has a major impact on the first cell in the underexpanded sonic jet. Addy [12] performed a number of experiments on six different shapes of sonic orifice with different pressure ratios and Reynolds numbers. The flow field was visualised using 10-microseconds-shadowgraphs photos to examine Mach disk location and diameter. Choking characteristics and mass flow rate were found to differ for different nozzle shapes. Further, two correlations to calculate Mach disk diameter were established (Eq. 1.3 and Eq. 1.4). The fact that evaluating Mach disk diameter follows different paths for different nozzle shapes manifests the importance of nozzle and upstream geometry in the formation of jet structure. Alam et al. [48] numerically studied the effect of nozzle geometry on the discharge coefficient and sonic line. They simulated different contoured shapes, conically converging, and conically diverging nozzles. It was found that nozzle geometry affects the discharge coefficient significantly. Further, when the radius of contoured nozzle increases, the sonic line moves upstream, and when the converging angle increases in conical nozzles, the sonic line shifts downstream the nozzle exit. Chauhan et al. [49] examined the impact of the aspect ratio of an elliptical sonic orifice on the flow field downstream of the nozzle exit, while maintaining the exit area. They also varied the pressure ratio across the nozzle to modify the level of underexpansion. They concluded that elliptical nozzles with higher aspect ratio have the higher mixing rate when the jet is moderately underexpanded. However, when the flow becomes extremely underexpanded and Mach disk forms, nozzles with lower aspect ratio showed better mixing. Hatanaka and Saito [27] performed a number of experiments

and numerical simulations to study the influence of nozzle geometry as well as the plenum chamber on the emitted jet. They found that flow pattern upstream of the orifice affects the jet, and the contraction of the fluid at the nozzle causes the jet to divert toward the nozzle axis. Further, it was seen that flow contraction reduces the mass flow rate and impacts the jet structure which includes maximum cell height, length and the diameter of Mach disk. Menon and Skews [50] investigated the effect of nozzle geometry on the formation of barrel shock. They performed simulations on contoured, converged conical, and diverged conical nozzles. They found that barrel shock takes place at lower pressure ratio when using a contoured nozzle comparing to conical nozzles. Further, the contoured nozzle produced the highest Mach disk in the pressure ratio range 2.0 through 10.0, and with increasing pressure ratio, the curvature of Mach disk in the flow direction increased. The fluid contraction (vena-contracta) phenomenon was observed for the sharp-edged nozzles, which narrows the jet boundary and shifts the minimum height of the jet downstream the orifice exit. Chen et al. [51] studied the underexpanded nitrogen gas injected into sodium-gas heat exchanger channel using LES. They compared the jet structure resulting from circular, rectangular, and square orifices. It was found that using rectangular and square nozzle shape would push the Mach disk further downstream and decrease its diameter. It was also seen that nozzle aspect ratio has a significant effect over the jet elements such as Mach disk location and diameter, and jet diameter, the latter was seen to increase the most when using rectangular and square nozzle shape. Samsam-Khayani et al. [52] visualised the flow field downstream a nozzle exit using Z-type schlieren to examine the influence of boundary conditions and nozzle geometry on the jet structure. They noted that diameter of Mach disk increased, in case of overexpanded jet, along with increasing pressure ratio to reach a saturation point after which it decreased for converging-diverging nozzle with large exit diameter. However, it remained constant when using a nozzle of small exit diameter.

A previous work by Jraisheh et al. [41] described the influence of boundary condition, at the sonic nozzle inlet, on the elements of underexpanded jet, assuming a contoured nozzle geometry that attains a uniform flow at the throat. However, it is evident from the literature cited that nozzle and settling chamber geometry play a significant role in developing the jet elements in the near-field region (a few diameters downstream the nozzle exit). Moreover, the contraction of the fluid (vena-contracta) happens when the nozzle has a sharp edge. It causes the jet diameter to shrink downstream the nozzle exit and then expand rather than expanding immediately from the nozzle lip. The complex structure of underexpanded jet includes Mach disk, which is a Mach reflection of the barrel shock.

Considering the importance of upstream geometry on the jet structure, it is desirable to perform simulations for possible upstream geometries and understand their impact.

1.5 Supersonic nozzle optimisation

Nozzles are also standard sources of freejet where the jet flow is expected to be uniform for the desired application. Such supersonic/hypersonic freejet testing facility is essential for various applications like rocketry, combustion experiments, study of gas condensation [53–55], spectroscopy of radioactive atoms [56], spectroscopy of molecules in non Local Thermal Equilibrium (non-LTE) conditions [42], gas phase reaction kinetics at very low temperature for astrophysical applications of neutral [57] or charged [58] species using either continuous [59] or pulsed [60–62] operating de Laval nozzles, etc. Supersonic freejet is specifically characterized with a complicated compressible flow region and sophisticated shock-wave structure [63]. Producing such a flow for a desirable application is usually achieved by accelerating a high pressure gas through a convergent-divergent (C-D) nozzle [64]. Here, the convergent part accelerates the gas from the stagnation state to the sonic state at the nozzle throat. Then the divergent part carries out further isentropic expansion of the flow to the supersonic or hypersonic state as per (Eq. 1.5)

$$\frac{dA}{A} = (M^2 - 1)\frac{dV}{V} \tag{1.5}$$

where, A is the duct area, M is Mach number and V is the flow velocity.
However, (Eq. 1.5) follows the inviscid one-dimensional approach, ignoring the viscous effects like boundary layer formation at the nozzle wall and the possibility of oblique shock formation due to flow separation, if the flow encounters sudden expansion. Thus, the nozzle design procedure has to account other parameters along with the area ratio. In general, more focus is given to the design of the divergent part due to the possibility of shock formation [65]. But the diverging section should be cautiously designed where flow spherically expands outwards from throat to exit and achieves the desired properties. The most prominent requirement in many freejet applications is the radially-uniform flow at the nozzle exit which has to be accounted while designing the nozzle. It is known that rockets require a radially-uniform flow at the exit since it corresponds to the maximum thrust thrust [66]. Radially-uniform flow at the exit is also required in case of thrust vector control in order to correct the trajectory precisely. Further, in case of absorption spectroscopy, non-diverging exit flow is desirable to reduce the line-width [42, 56]. Hence, a nozzle contour, for a non-diverging and radially-uniform flow at the outlet, has attracted the designers to take into account the shape of the wall along with the nozzle area ratio.
de Laval nozzle, or contoured nozzle, is a convergent-divergent duct, carefully designed to obtain a perfectly expanded (that is, neither under nor over-expanded) freejet characterized by a spatial uniformity at the outlet of the nozzle [43]. But there are many challenges which nozzle designers encounter before achieving such ideal radially-uniform flow at the exit. These challenges include non-uniform radial distribution of the gas velocity. A major reason for this challenge is the nozzle wall based boundary layer which continues to grow further downstream as the shear layer, and introduces non-uniformity in the flow field. Another

difficulty would be having shock or expansion fan at the exit in an over or under expanded condition. Having these flow features at the nozzle exit disturbs the flow and introduces flow property variation in the normal direction. Besides these, an important point about the contoured nozzle is that a nozzle designed for a particular exit Mach number can not be used for any other Mach numbers due to the dependency of Mach number on the local area ratio [67]. The above-mentioned challenges motivated designers to adopt or evolve different methodologies to achieve contoured nozzle designs and then to verify the optimised shapes [68].

Atkinson and Smith [43] used the Method of Characteristics (MoC) to construct the nozzle contour in three parts; part-I, immediately downstream the throat, where most of the expansion occurs and it is steeper than the other parts, part-II where the flow acts like a source flow that still has finite radial velocity, and part-III which turns the flow towards the exit and brings it to the desired Mach number in a uniform manner. In this design, a certain distance was added to the nozzle geometry to account for the displacement thickness, δ^*, of the boundary layer. This method is proved to be effective to construct a contoured nozzle. Lemos et al. [69] used the same method (MoC) to optimise and fabricate the contoured nozzle. Then they conducted experiments using these nozzles having exit Mach number of 3.0 and 6.0. They were able to maintain a quasi-uniform flow for almost one radius downstream the nozzle exit. Importance of matching the jet pressure with the back pressure was asserted to sustain a radially-uniform flow downstream the exit which would be free from expansion fans and oblique shocks. Schmid and Veisz [70] suggested that a high density flow through a short duct with a small area ratio is a way to produce a jet with a thin boundary layer. They observed a sharp edge jet for multiple Laval nozzles through the measurement of density profile at the nozzle exit for different nozzle angles. It has been concluded that the small divergence angles (less than 10°) do not affect the jet divergence, rather it gets influenced by the area ratio. Munday et al. [71] pointed out the problem of supersonic aircraft nozzle design, where attached flat plates are employed to form a polyhedral wall. Such design simplifies the problem, although it creates a sharp-edged throat. They experimented with a conical C-D nozzle with different operating conditions, and concluded that a conical supersonic nozzle would generate two patterns of diamond-configuration shock, one of them is generated at the sharp-edged throat, and the other is due to the divergence angle of the nozzle lip. Allman and Hoffman [72] employed three methods of optimisation, multidimensional line search, the method of steepest descent, and Newton's method, to construct a nozzle wall using a second-order polynomial. The objective here was to arrive at a nozzle with maximum thrust, assuming isentropic expansion of a perfect gas. They achieved the set objective but for a limited range of pressure ratios. Hence it was suggested to allow more degrees of freedom for the polynomial for further improvement. Yu et al. [73] developed a novel plasma nozzle, including the throat size and depth of convergent and divergent parts to enhance the processing capability of plasma torch. Their computational optimisation process was based on ANSYS Fluent for the logical choice of geometry, suitable for plasma processing footprint

and the aerodynamic properties. This design was tested using CFD and then employed in the experiment which showed 5% improvement in the efficiency of plasma delivery system than the original design. The improvement was further seen in the velocity and temperature distribution, and their values at the throat area. Tani and Ohmaru [74] have used hybrid numerical method, involving Navier-Stokes (N-S) and Direct Simulation Monte Carlo (DSMC), to study the surface pressure and heat transfer resulting from impinging rocket nozzle gas plum on a surface or plum-plum interaction. Yu et al. [75] have proposed a new approach for an inverse nozzle design depending on pressure distribution requirements and based on convolutional neural network (CNN) technology. They have concluded that the proposed model can predict accurately by training and hyperparameters optimization, and the pressure distribution is highly dependent on the nozzle contour smoothness, which in turn can be improved using a regularization term. Paul P et al. [76] have performed a numerical examination on an optimised nozzle performance with a varying pintle profile geometry, while maintaining the nozzle and pintle shapes up to the throat without changing. The results have shown a better performance of curved pintle with highest base curvature with regard to base pressure and thrust output. At higher pressure ratio, a pintle with an inclined base performed better in terms of overall thrust coefficient because of the higher contribution from momentum thrust. Bagy et al. [77] have used a Computer-Aided Design (CAD) model in an optimisation process to improve the nozzle propulsive performance, considering the full geometry of the aft-engine body. This study resulted in an optimised nozzle and cowl shape for a turbofan separate-jet engine. Heath et al. [78] have implemented aerodynamic shape optimisation technique to reduce the pressure disturbance near the propulsion system. The process included a gradient-based optimisation along with FUN3D framework to reduce the compression and/or expansion in the near-field area. Rao [79] developed an analytical method to design a contoured rocket nozzle which corresponds to zero back pressure with maximum thrust utilizing the concept of characteristics lines. In the view of the importance to design a contoured nozzle, it is desirable to arrive at an algorithm to design a nozzle which can deliver a uniform flow for various applications.

Shear layer at nozzle exit Beyond the efforts for designing the contoured nozzle, researchers also considered the importance of shear layer at the nozzle exit. In the second half of the last century, the interest in shear layer, originated from nozzle flow, has increased, initially due to near wake problem in turbines, and later on because of its important role in supersonic combustion [80]. There have been extensive studies [81] to explore the transition from laminar to turbulent shear layer that separates two supersonic streams, and the laminar free-of-periodic-oscillation shear layers. The spread rate of shear layer was found to be slower in supersonic jet than it in incompressible shear layer [82]. This difference is found to be partially related to the density ratio between both sides of the shear layer, especially when the supersonic jet is spreading in a quiescent medium. But the main reason for the slower spread is the different formation processes for shear layer, as it widely depends on its instability in the case of supersonic jet. That is, the supersonic shear layer contains large

coherent structures formed at the earlier stages of instability. Further, the experimental results of Dimotakis [83] show that the dynamics of compressible shear layer does not only depend on the density and velocity ratio, rather it is related to the earlier growth and initial conditions of the boundary layer. In this context, the experiment of Batt [84] revealed that turbulent boundary layer results in a shear layer with more growth rate of thickness and entrainment compared to the undisturbed boundary layer.
In mixing shear layer, Papamoschou and Roshko [80] coined the concept of convective Mach number, which is the "intrinsic" Mach number when it comes to the effects on shear layer transition. In the case of jet propagating in still gas, convective Mach number is proven to be the same Mach number of the jet. Fourguette et al. [85] have experimentally probed the evolution of shear layer of an axisymmetric supersonic jet, while matching the exit pressure with back pressure using laser-based Rayleigh scattering techniques. Their findings suggest that the structures in compressible shear layer move in three-dimensional manner, and this aspect gives more three-dimensionality to compressible shear layer compared to the incompressible shear layer. Rossmann et al. [86] have examined the supersonic shear layer with different compressibilities and convective Mach numbers, numerically and experimentally. It was found that a higher compressibility rate would hamper the growth rate, and it would produce larger structures, while these structures hardly appear in a shear layer of moderate compressibility. The work of Ma et al. [87] focused on the geometrical effect on the growth trend of a confined subsonic-supersonic shear layer. The influencing factors were found to be the combustion chamber height, the splitter plate thickness, and the supersonic nozzle exit diameter. The interaction between the shock train within the supersonic jet and the shear layer was seen to increase its thickness locally. Another work of Ma et al. [88] was to investigate the growth of shear layer between subsonic and supersonic streams in a wind tunnel. It showed that the pressure difference between the streams induces the shear layer to deflect towards the low pressure stream, and hence triggers the shear layer transition. Davis and Kumar [89] have observed that freejet shear layer is characterized by abrupt growth near the nozzle exit, afterwhich it maintains a linear growth for certain region. In this region, the growth rate is seen to decrease.
As noted from the literature, there is distinct dynamics of shear layer, and it is governed by many parameters. However, the growth of boundary layer within the nozzle actively affects the growth of the shear layer downstream of the exit plane.

1.6 Altitude compensating nozzle

After tackling the challenges to achieve a supersonic flow suitable for the required application, it occurs that the nozzle designed for a specific Mach number of pressure ratio operates ideally under design conditions. (Equation 1.5) governs the output of the nozzle, and therefore a fixed geometry produces an ideal flow with fixed properties. Hence, going through the tiresome procedure of building an optimised nozzle will only be ideal for a single case. This

issue appears in many applications as the need for reliable and affordable means to produce a supersonic/hypersonic jet has rapidly increased with the evolution of space flights. The nozzle that produces such jets is the integral part of turbojet or rocket engine. But the high speed nozzles are also required for understanding chemical processes or for spectroscopic measurements. These applications were mentioned in Section 1.1.

A previous study by Munday et al. [71] has shown that a conical nozzle differs from smoothly-contoured nozzle by two aspects. Firstly, the conical nozzle has a sharp throat which causes the formation of a shock wave within the nozzle, hence making it impossible to achieve a shock-free operation. Secondly, the continuously-diverging wall causes the flow to gain a certain radial velocity at the nozzle exit, i.e., the flow would be directed outwards at the exit plane. Each of these two aspects creates a diamond shock, which introduces a double-diamond configuration within the jet, regardless of it being underexpanded, overexpanded, or ideally-expanded. Moreover, Perumal and Rathakrishnan [90] experimentally proved that, for circular jet, the length of supersonic jet core, or the inviscid core, is highly dependent on the exit pressure ratio (ratio of nozzle exit pressure to back pressure). Many applications [42, 91] require this supersonic core to be as uniform and long as possible, and therefore it becomes crucial to grasp the influence of other factors on the jet core, including the nozzle wall shape. Rao [92] constructed the diverging part of a nozzle contour, for optimum thrust performance, by integrating an arc immediately downstream the throat with a quadratic Bezier curve to form a bell contoured nozzle. Similar methodology was found suitable to obtain an optimised Scramjet nozzle [93] for a fixed combustor outlet. Recently, Brahmachary and Ogawa [94] used a multi-point multi-objective optimisation technique to address the impact of geometrical parameters on the intake performance of a Busemann-based Scramjet, in the sense of compression efficiency and drag reduction. Further, Aerodynamic Shape Optimisation (ASO) can also be a useful tool to obtain a nozzle geometry that provides both efficient propulsion and low-noise performance. It is evident that CFD-based ASO can be computationally cumbersome [95], and therefore, before feeding the problem to a more sophisticated solver, it is more efficient to study the influencing factors using a low-fidelity approach. Heath et al. [78] used a one-dimensional gas dynamics solver, along with the method of characteristics, to build a nozzle wall geometry, and then introduced a plug to reduce the noise. Here, the objective was to reduce the pressure disturbance at and downstream of the nozzle exit which would in turn reduce the noise, and this reduction is important for supersonic flight approval. Davidenko et al. [96] considered a direct optimisation for the maximum thrust nozzle shape with a center body for different nozzle lengths and diameters. Variation of the diameter of center body was found to change the thrust for both inviscid as well as viscous wall boundary conditions. Mason and Broadhurst [97] employed Monte Carlo based mathematical model to solve the problem of gas misalignment while using multiple nozzles on a single rocket motor, since the thrust alignment is not an issue in case of a single nozzle. This approach is based on a series of random selections that start from pre-defined probability distribution.

Among the available choices, Conventional Bell (CB) nozzle is one of the most efficient nozzle for rocket flights. Nevertheless, its efficiency is widely dependent on the pressure ratio, and it appears to operate efficiently under certain conditions whereas its efficiency drops when the pressure ratio changes. The rocket nozzle, generally, is designed to perform between a fixed chamber pressure and a varying back pressure, and this would alter the efficiency of the nozzle while operating at off-design conditions (off-design back pressure). Hence, Altitude Compensating Nozzles (ACN) are introduced [98], including the dual-bell nozzle [99] and the fixed geometry nozzle, that support a controlled separation from the nozzle wall, at a desired "effective" area ratio. Dual-bell ACN tackles the problem of the varying pressure ratio, whether the two bells are fixed or the second bell forms a nozzle skirt for high altitude conditions. This nozzle utilizes the first bell when the pressure ratio is low, i.e, at low altitudes, and includes the second bell when the back pressure drops, leading to increase in pressure ratio, at high altitudes, so as to maintain the ideal expansion at all operating conditions. The operation of a dual-bell nozzle is sketched in the schematic Fig. 1.6. That is, the rocket nozzle efficiency is considered to be higher when all the streamlines are normal to the exit cross-section [100]. This condition corresponds to the ideal expansion of the nozzle.

Furthermore, bleeding slots in supersonic flow ducts have been used to reduce the boundary layer separation from adverse effects of shock wave-boundary layer interaction. The bleeding holes introduce different effects on the duct flow according to their width, length and angle [101]. Researchers have proved that, introducing bleed slots in the supersonic inlets can suppress the shock-induced separation resulting from the interaction between turbulent boundary layer and normal shock [102]. It is evident that the presence of multiple bleed slots could "improve" the boundary layer by drawing off the low momentum part of the fluid, which in turn increases the the average kinetic energy carried by the boundary layer, and hence making it less vulnerable for separation [103]. Moreover, as it is desired to control the growth of boundary layer in the inlets [104], it is also important to mitigate its effect at the outlet or within the nozzle. Further, Weiss and Olivier [105] concluded that, despite the loss in mass flow rate caused by the bleeding system, the static pressure gradient strengthens due to the bleeding. However, the total pressure recovery is less efficient in this system because of the mass loss.

It can be noticed from the literature that the nozzle shape optimisation is highly desirable in many engineering and research applications [106]. But, it must be noted that the design of optimum solid nozzle is based on fixed operating conditions and any change in these conditions would alter the nozzle performance. Hence, for getting the optimum performance, there is requirement of a separate solid nozzle for each nozzle operating condition. Besides, a nozzle that is designed for a specific pressure ratio can only operate ideally at that pressure ratio. A rocket nozzle, for example, experiences a variety of back pressures from launching to exiting earth atmosphere. Moreover, a spectroscopic experiment may require different flow parameters, which necessitates different exit Mach number each time. These requirements

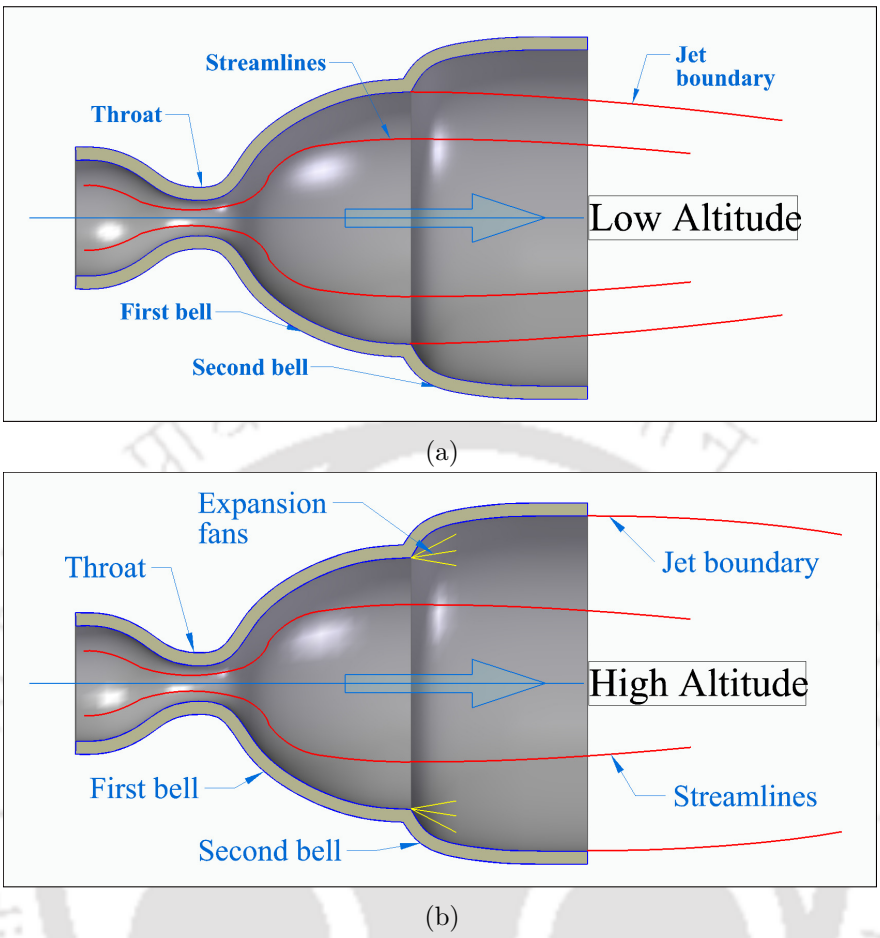

Figure 1.6: A schematic figure of the operation of a dual-bell nozzle: (a) Low altitude operation and (b) High altitude operation.

demand supersonic nozzles with adjustable area ratio (mostly exit area), and that is why ACNs were adapted for many applications. The available ACNs have a few limitations like operating in a small range of pressure ratio (dual-bell nozzle operates optimally on two pressure ratios). Hence, it is proposed to apply the concept of multiple area ratios on a wider range, by introducing more than two stages of operation. Therefore, ringed nozzle would possibly solve the issue of varying back pressure due to variation in altitude and produce jets with varying parameters as per the laboratory requirements. A sectional $3D$ view of the suggested arrangement is shown in Fig. 1.7. Such arrangement is also effective for nozzle wall-based boundary layer control through suction of low momentum flow. It is believed that the ringed nozzle introduces different advantages to the jet, which correspond to the requirement of different applications. Various arrangements of the rings are possible by altering the gap width among them, which help in controlling the boundary layer growth. Compensation for the change in the external pressure can also be obtained by re-arranging the existing rings to alter the nozzle area ratio, which is the leading parameter that corresponds to the pressure ratio. This can be done by adding or removing one ring or

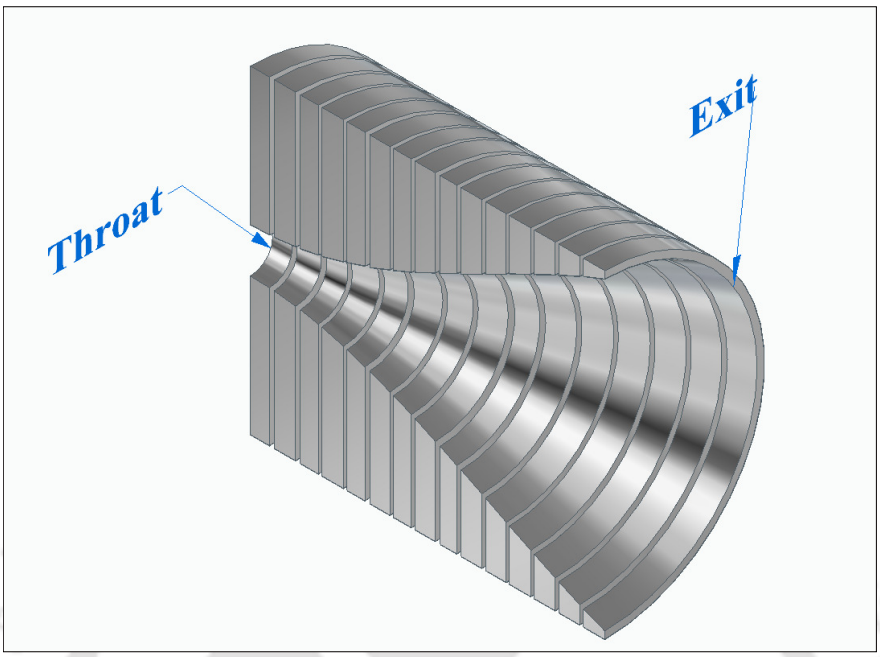

Figure 1.7: A $3D$ view of the ringed nozzle arrangement.

more at the nozzle exit, or can be achieved by fabricating the rings from flexible materials that allow area adjustment. Moreover, reduction of nozzle weight or lesser material requirement is an added advantage of the stacked-rings nozzle along with its adaptability for different operating conditions. Further, unlike solid nozzle, designed for optimum performance, it is possible to use the same set of rings for different operating conditions to achieve the optimum performance by adjusting their geometric parameters. In case of the spectroscopic studies, there is indeed a requirement of optimum nozzle for uniform flow at the exit along with the larger inviscid core. Hence, initial objective of current study is to propose a novel ringed nozzle design or nozzle shape, for such applications [42, 57–62], using steepest descent optimisation algorithm for a minimum exit radial velocity [42]. Such studies are desirable to reduce the number of optimum nozzles required for each operating condition. Hence, the current approach is mainly proposed as a proof-of-concept, and to assist laboratory studies that demand such requirement. However, argon is prominently used in those investigations [42], therefore argon is used in the present studies as well. Thus, current proposition targets replacement of the rigid nozzle wall with a stack of rings to introduce flexibility in the design as to form different nozzle shapes. The proposed nozzle is designed through optimization process and tested using CFD to provide an insight on its utility.

1.7 Research motivations

The literature shows an increasing interest in the elements and structure of supersonic free-jet. Researchers target the characteristics of Mach disk including its location and height, the geometric constraints are also found to determine the flow features upon leaving the

nozzle, and hence influencing the jet structure. Further, there have been many attempts to construct a supersonic nozzle shape to obtain a uniform flow for different applications. Also, there has been an interest in the shear layer between a supersonic stream and a still gas. Furthermore, many attempts are directed to overcome the problem of operating under varying conditions.

It is seen that many works were aimed to study the underexpanded sonic gas flows and their characteristics, in particular, Mach disk. However, the point at which the regular shock reflection turns into Mach reflection, forming Mach disk, is not addressed, and it is found to be critical in defining the jet structure. Further, most of the works tend to use air as a flowing gas, while merely mentioning the effect of temperature on the flow features. Therefore, it is crucial to investigate how other gases behave under different conditions, including varying temperature.

While more focus is directed on the impact of fluid properties, it is evident that upstream geometry has significant effects on the flow field downstream, especially in high-speed flows. Some studies have considered the shape of settling chamber and others targeted the nozzle geometry upstream of the throat. Hence, it is important to address the changes in jet structure that accompany the varying upstream geometry.

Supersonic nozzle is an important instrument in many facilities, from laboratory purposes to propelling systems. It is demanded to provide customised gas flows corresponding to the desired application. Many methodologies are proposed to achieve an optimal design of such nozzles, but most of them employ the Method of Characteristics for this purpose. While MoC provides a robust design for the nozzle in rockets and wind tunnels, it is found to have limitations with respect to the geometric constraints of the nozzle and high Mach numbers (more than 8.0). Thus, more attention is required to construct an optimal shock-free nozzle wall for different applications, while avoiding the troublesome two-dimensional flow equations. Further, the shear layer evolution of the jet exiting such nozzle is linked to the nozzle shape and boundary layer growth within the nozzle, and hence this relation needs to be attended.

Amongst the challenges that face the atmospheric and space flights, operating under varying ambient conditions is found to be of high importance. It affects the motor efficiency and increases the fuel consumption. A few designs, including dual-bell nozzle, are proposed in the literature to address this problem, and they are found to be helpful in many scenarios. Nevertheless, more improvement is required, especially that dual-bell nozzle has ideal performance in two states, whereas varying altitude calls for varying geometry. Therefore, innovative designs have to be in place to tackle the continuous technological advancement.

1.8 Research objectives

In the view of the detailed literature review, following objectives are set for the current studies:

- Developing a compressible flow solver, and validating its ability to capture the complex structure of the freejet and supersonic nozzle flow.
- Examining the characteristics of the freejet, emanating from a sonic orifice at Mach number of unity, within an exit pressure ratio range of 1.0 to 20.0, considering three gases with varying temperature.
- Evaluating the point at which the regular shock reflection transforms into Mach reflection (with Mach stem, or Mach disk) in the case of sonic freejet.
- Addressing the influence of upstream geometry (settling chamber geometry) on the structure of sonic jet produced from orifices with different geometries.
- Developing an optimised supersonic nozzle shape to produce radially-uniform flow, and avoid flow separation.
- Studying supersonic shear layer evolution, between supersonic jet and a stagnant gas.
- Exploring and examining a novel altitude compensating nozzle, the ringed nozzle, for the purpose of operating under varying pressure ratios.

1.9 Organisation of thesis

The remainder of the thesis is organised as follows. Chapter 2 sheds the light on the equations that governs the compressible flow, in addition to an overview of the imposed boundary conditions. Chapter 3 comprises the investigation pertaining the sonic freejet and its characteristics with varying flow properties. The impact of varying upstream geometry on the structure of sonic freejet is addressed in Chapter 4. Chapter 5 describes the optimisation algorithm used to obtain a shock-free supersonic nozzle with a radially-uniform outflow, with an insight on shear layer evolution. Chapter 6 proposes an innovative design for a possible altitude compensating nozzle that is able to provide a solution for flight under varying conditions. Lastly, Chapter 7 discusses the salient contributions of the thesis and directions for future research.

CHAPTER 2

NUMERICAL METHODOLOGY

Abstract

As the flow field analysis is done computationally, therefore, the necessary numerical methodology used is discussed in this chapter. The details of the one-dimensional compressible flow solver are provided, along the optimisation method used to create a supersonic nozzle. Further, the governing equations employed in the CFD solver are mentioned, and the boundary conditions imposed at different boundaries are elaborated.

2.1 One-dimensional flow solver

Various techniques are suggested by many researchers to arrive at an optimum configuration of a nozzle for a given operating condition. Some of those techniques rely on Method of Characteristics (MoC) which has its own limitations while implementing for high Mach number nozzles. The optimisation techniques which consider CFD simulations for each optimisation cycle solve partial differential equations multiple times to achieve an optimal aerodynamic shape, and it is a computationally-expensive process. But, it seems more conventional to perform a simpler analysis before conducting any experiment or computationally-expensive simulations. Therefore, a computer program based on one-dimensional gas dynamics relations is developed to generate and optimise the nozzle wall shape. The process adapted for this outcome is discussed in this section.

While initialising the optimisation process for arriving at a desired nozzle shape, the nozzle length is divided into equal discrete points, and the initial guess for the nozzle wall shape is assumed to be the basic conical nozzle with the required dimensions. The flow properties across each point are obtained from the quasi one-dimensional gas dynamics relations using the inlet conditions at the throat. This method of estimation of flow properties is based on inviscid flow assumption. The inputs for the program are nozzle dimensions, type of gas, and the total temperature. At each point, Mach number is calculated by using Eq. 2.1 which is

based on the area ratio of this point:

$$\left(\frac{A}{A*}\right)^2 = \frac{1}{M}\left(\frac{2}{\gamma+1}(1+\frac{\gamma-1}{2}M^2)\right)^{\frac{\gamma+1}{\gamma-1}} \tag{2.1}$$

Having found Mach number, the static temperature at each discrete point is computed using isentropic relation (Eq. 2.2):

$$\frac{T_0}{T} = 1 + \frac{\gamma-1}{2}M^2 \tag{2.2}$$

The local speed of sound and subsequently the total velocity of the flow at every division are calculated as:

$$a = \sqrt{\gamma\ RT} \qquad \& \qquad V = M.a \tag{2.3}$$

As the main object of the algorithm is to find the radial velocity at the nozzle exit, the inclination angle of the nozzle lip is obtained as: $\theta = tan^{-1}(dy/dx)$ for the last segment of the nozzle length. The total velocity is then multiplied by $sin\theta$ to calculate the radial velocity at the nozzle exit plane. Thus, obtained exit radial velocity is the objective function considered in the optimisation algorithm. This algorithm is summarised in Fig. 2.1. The

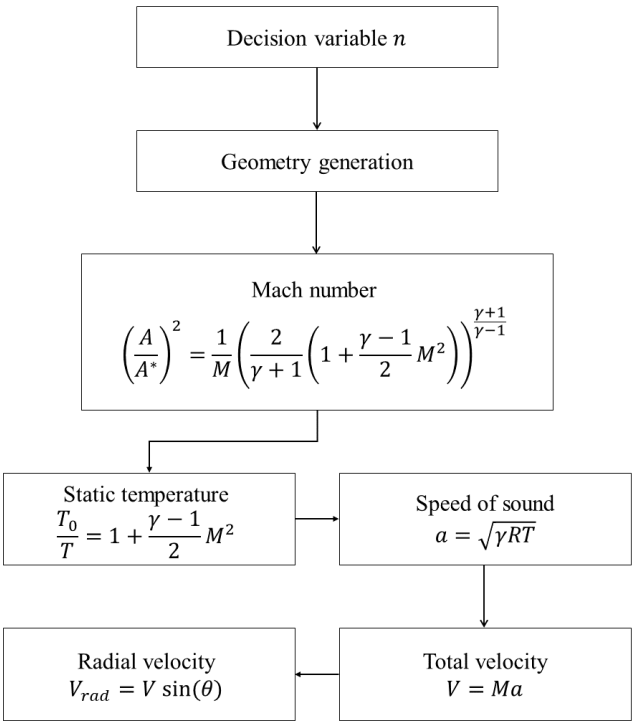

Figure 2.1: The sequence of solving in the one-dimensional flow solver.

steepest descent gradient technique is coupled with this flow solver to achieve an optimal, shock-free, nozzle shape (more on that in Section 2.2).

It is known that the viscous effects are inevitable in the case of high-speed flows. The boundary layer at the wall compresses the flow towards the axis, which might divert the flow inwards and create a negative radial velocity within or at the exit of the nozzle. Hence, the objective function, $V_{rad,ex}$, obtained with the assumption of inviscid flow, should be higher than zero so as to account for the formation of boundary layer, and overcome its diverting effect. Moreover, for the given constraints of length, throat diameter and exit diameter, the optimisation process may suggest a shape with a large initial divergence in the divergent part. The sudden expansion, immediately downstream of the throat, with large divergence angle, causes the flow to turn into itself within the nozzle, and hence, there is a possibility of shock formation in the nozzle. For this reason, the initial angle of divergence should be considered as a design parameter. In the current solver, the constraint of the initial angle of divergence is imposed as a penalty function, whenever necessary, which contains a penalty factor. This factor prevents the initial angle of divergence from exceeding a certain value prescribed by the user and decides the importance of the initial angle and the exit radial velocity according to the requirements of the nozzle design. Treating the problem with such function relaxes the weightage of exit radial velocity by giving a high weightage to the initial angle.

2.2 Optimisation algorithm

Optimisation processes are often employed to satisfy one or more specific requirements, called objective functions. The process includes determining the optimal value of the influencing factor (or factors), called decision variables. One of the objectives of the current investigation is to construct a supersonic nozzle shape, capable of producing a uniform flow. Therefore, gradient based steepest descent [107] is adopted to achieve this nozzle shape optimisation. This method is conventionally used to approach the minimum of a function by iterating in the direction of the negative gradient. The objective function, in the radially-uniform flow case, is the minimum value of overall radial velocity at the exit plane of the nozzle ($V_{rad,ex}$). The decision variables in this case are coordinates of control points of the Bézier curve which represents the nozzle wall shape. Third and fourth-order Bézier curves are used as the mathematical representations of the nozzle wall, as they provide sufficient control points for creating the shape. The mathematical expression of such curves is given in Eq. (2.4):

$$B(t) = \sum_{i=0}^{n} \begin{pmatrix} n \\ i \end{pmatrix} (1-u)^{n-i} u^i P_i \tag{2.4}$$

where $0 < u < 1$ and n is the order of the curve which is chosen to be 3 or 4 in the present work. Here, control points are P_i. It may be noted that the Bézier curve represents only diverging part of the nozzle which is considered for shape optimisation. Hence the inlet of this nozzle starts from the sonic throat. When fourth order Bézier curve is chosen for representation, it accounts five control points, out of which first and last points correspond

to inlet and exit of nozzle. Therefore, the coordinates of these points remain fixed as per the inlet and outlet diameters of the nozzle. But the other three control points change their coordinates in the process of optimisation. In case of third order Bézier curve representation, out of four available control points, two points remain fixed at the nozzle boundaries, and the other two points act as control points.

During the optimisation, at every value of the decision variable, the gradient of the objective function is computed and checked whether or not it is less than a pre-defined small value (ϵ). Upon satisfying this condition, the iteration is terminated and the decision variable, corresponding to the converged solution, is considered to be optimal. If this condition is not satisfied, then the decision variable is perturbed according to the following equation:

$$x_{n+1} = x_n - \alpha.\nabla f\,(x_n) \tag{2.5}$$

where α is the step size of imposed perturbation and it plays an important role in finding the optimum value of objective function. When α is considered constant, it should be kept to a small value to ensure the smooth convergence, whereas in the general case, α is decided by 1-D search method according to the requirements of the problem. The outcomes of these methods are discussed in the results, as the value of α influences the optimisation algorithm which may in turn alter the resulting geometry. The necessary gradient calculation for the steepest descent optimisation method is done using forward finite difference approximation as follows:

$$\nabla f = \frac{f_{n+1} - f_n}{x_{n+1} - x_n} \tag{2.6}$$

The optimisation algorithm of steepest gradient descent is illustrated in Fig. 2.2.

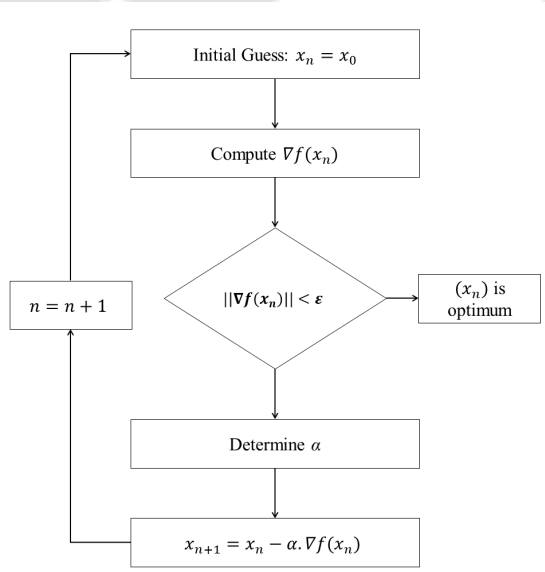

Figure 2.2: The algorithm of the steepest gradient descent optimisation method.

2.3 CFD solver formulation

In order to probe and visualise the flow field, governing equations for the inviscid or viscous fluid flow are solved using finite volume formulation. In this section, we give an insight over the mathematical expressions of these governing equations which represent the conservation laws viz. mass, momentum, and energy. Since all of the simulations are performed axisymmetrically, all of the equations herein are in axisymmetric form (Eq. 2.7). Navier-Stokes equations have been used to represent the viscous flow, whereas Euler's equations are used to model inviscid flow. To account for turbulent effects, $k-\epsilon$ model is employed.

In fact, the conservation laws for both viscous and inviscid flow may be expressed in the vector form as:

$$\frac{\partial \mathbf{A}}{\partial \mathrm{t}} + \frac{\partial \mathbf{B}}{\partial \mathrm{x}} + \frac{\partial \mathbf{C}}{\partial \mathrm{y}} + \frac{\partial \mathbf{D}}{\partial \mathrm{x}} + \frac{\partial \mathbf{F}}{\partial \mathrm{y}} + \mathbf{S_I} - \mathbf{S_V} = 0 \tag{2.7}$$

where,

$$\mathbf{A} = \begin{bmatrix} \rho \\ \rho u \\ \rho v \\ \rho E \end{bmatrix}; \quad \mathbf{B} = \begin{bmatrix} \rho u \\ \rho u^2 + p \\ \rho uv \\ \rho u\left(E + \frac{p}{\rho}\right) \end{bmatrix}; \quad \mathbf{C} = \begin{bmatrix} \rho v \\ \rho uv \\ \rho v^2 + p \\ \rho v\left(E + \frac{p}{\rho}\right) \end{bmatrix}$$

$$\mathbf{D} = \begin{bmatrix} 0 \\ \tau_{xx} \\ \tau_{xy} \\ u\tau_{xx} + v\tau_{xy} - q_x \end{bmatrix}; \quad \mathbf{F} = \begin{bmatrix} 0 \\ \tau_{xy} \\ \tau_{yy} \\ u\tau_{xy} + v\tau_{yy} - q_y \end{bmatrix}$$

the vectors $\mathbf{S_I}$ and $\mathbf{S_V}$ are the inviscid and viscous source terms, respectively, and are relevant only for axisymmetric flows. These may be expressed as:

$$\mathbf{S_I} = \frac{1}{y}\begin{bmatrix} \rho v \\ \rho uv \\ \rho v^2 \\ \rho v(E + \frac{p}{\rho}) \end{bmatrix}$$

$$\mathbf{S_V} = \frac{1}{y}\begin{bmatrix} 0 \\ \tau_{xy} - \frac{2}{3}y\frac{\partial}{\partial x}(\mu v/y) \\ \tau_{yy} - \tau_{\theta\theta} - \frac{2v}{3y}\mu - \frac{2}{3}y\frac{\partial}{\partial y}(\mu v/y) \\ u\tau_{xy} + v\tau_{yy} - q_y - \frac{2\mu v^2}{3y} - \frac{2y}{3}\frac{\partial}{\partial y}(\mu v^2/y) - \frac{2y}{3}\frac{\partial}{\partial x}(\mu uv/y) \end{bmatrix}$$

where,

$$q_x = -k\frac{\partial T}{\partial x}; \qquad q_y = -k\frac{\partial T}{\partial y} \tag{2.8}$$

$$\tau_{xx} = \mu\Big(\frac{4}{3}\frac{\partial u}{\partial x} - \frac{2}{3}\frac{\partial v}{\partial y}\Big); \qquad \tau_{yy} = \mu\Big(\frac{4}{3}\frac{\partial v}{\partial y} - \frac{2}{3}\frac{\partial u}{\partial x}\Big); \qquad \tau_{xy} = \mu\Big(\frac{\partial u}{\partial y} + \frac{\partial v}{\partial x}\Big) \tag{2.9}$$

$$\tau_{\theta\theta} = \mu\Big(-\frac{2}{3}\Big(\frac{\partial u}{\partial x} + \frac{\partial v}{\partial y}\Big) + \frac{4v}{3y}\Big)$$

It is to be mentioned that in Eq. 2.7, **A** is the vector of conserved variables: mass, momentum and energy; and **B** and **C** represent the inviscid fluxes while **D** and **F** represent the viscous fluxes. The terms q_x and q_y are x and y components of heat flux whereas τ_{xx}, τ_{yy} and τ_{xy} are the components of the symmetric viscous stress tensor, and they are functions of the velocity gradients. Here, k is the thermal conductivity of the fluid and μ refers to the dynamic viscosity of the fluid which is evaluated using Sutherland's equation as:

$$\mu = \mu_{ref}\Big(\frac{T}{T_{ref}}\Big)^{3/2}\Big(\frac{T_{ref} + S}{T + S}\Big) \tag{2.10}$$

where, T_{ref} and μ_{ref} refer to the reference temperature and dynamic viscosity and are equal to 273.15 K and 17.17×10^{-6} Ns/m^2, respectively. Here, S is the Sutherland's constant for air (S=110.56). The equation of state (Eq. Eq. 2.11) closes the set of equations with the assumption of perfect gas.

$$p = \rho RT \tag{2.11}$$

where, p, ρ and T refer to pressure, density and temperature, respectively whereas R is the gas constant.

The in-house CFD solver solves Euler's equations while simulating for inviscid flow and solves the Navier-Stokes equations for laminar viscous flows.

2.4 Finite volume formulation

To partition the computational domain, a finite number of non-overlapping control volumes are used. These control volumes, also known as cells, allow the integration of the governing equations discussed in the previous section to be carried out on a per-cell basis. As a result, the integral representation of the governing equations can be expressed as:

$$\int_\Omega \Big(\frac{\partial \mathbf{U}}{\partial \mathrm{t}} + \frac{\partial(\mathbf{F_I} - \mathbf{F_V})}{\partial \mathrm{x}} + \frac{\partial(\mathbf{G_I} - \mathbf{G_V})}{\partial \mathrm{y}} + \alpha(\mathbf{S_I} - \mathbf{S_V})\Big) d\Omega = 0 \tag{2.12}$$

where, Ω is the volume of a cell. The equation can now be arranged as,

$$\int_\Omega \frac{\partial \mathbf{U}}{\partial \mathrm{t}} d\Omega = -\int_\Omega \Big(\frac{\partial(\mathbf{F_I} - \mathbf{F_V})}{\partial \mathrm{x}} + \frac{\partial(\mathbf{G_I} - \mathbf{G_V})}{\partial \mathrm{y}} + \alpha(\mathbf{S_I} - \mathbf{S_V})\Big) d\Omega \tag{2.13}$$

To approximate the various terms in Eq. 2.13:

The temporal term may be discretised as,

$$\int_\Omega \frac{\partial \mathbf{U}}{\partial t} d\Omega = \frac{\partial}{\partial t} \int_\Omega \mathbf{U} d\Omega = \frac{d}{dt}(\overline{\mathbf{U}} d\Omega) = \Omega \frac{d\overline{\mathbf{U}}}{dt} \tag{2.14}$$

where we define $\overline{\mathbf{U}} = \frac{\int_\Omega \mathbf{U} d\Omega}{\int_\Omega d\Omega}$ as a cell averaged value at the centroid of a cell. The RHS of Eq. 2.13 may be written as,

$$\int_\Omega \Big(\frac{\partial(\mathbf{F_I} - \mathbf{F_V})}{\partial x} + \frac{\partial(\mathbf{G_I} - \mathbf{G_V})}{\partial y} + \alpha(\mathbf{S_I} - \mathbf{S_V}) \Big) d\Omega = \int_\Omega (\nabla \cdot (\mathbf{H_I} - \mathbf{H_V}) + \alpha(\mathbf{S_I} - \mathbf{S_V})) d\Omega \tag{2.15}$$

Defining the vector $\mathbf{H}$ as,

$$\mathbf{H} = \mathbf{H_I} - \mathbf{H_V} \tag{2.16}$$

and employing the Gauss Divergence theorem gives,

$$\int_\Omega \nabla \cdot \mathbf{H} \; d\Omega = \int_S \mathbf{H} \cdot \hat{n} \; dS \tag{2.17}$$

The control volume is surrounded by a bounding surface denoted by the symbol S, with $\hat{n}$ representing the unit normal to this surface. To obtain a discrete approximation of the surface integral, we can use the following method:

$$\int_S \mathbf{H} \cdot \hat{n} \; dS = \sum_J \mathbf{H_J} \cdot \hat{n}_J \Delta S_J = \sum_J \mathbf{H}_{\perp \mathbf{J}} \Delta S_J \tag{2.18}$$

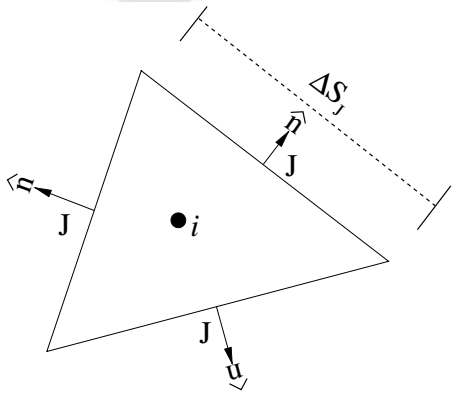

Figure 2.3: Cell nomenclature

where the summation is over faces J of the control volume. In Eq.2.18, ΔS_J represents the length of the face J of a control volume while $\mathbf{H}$ refers to the total flux normal to the face and includes both inviscid and viscous contribution.

$$\mathbf{H}_{\perp} = \mathbf{H}_{\mathbf{I}\perp} - \mathbf{H}_{\mathbf{V}\perp}$$

$$\mathbf{H}_{\perp} = \begin{bmatrix} \rho u_{\perp} \\ \rho u u_{\perp} + p n_x \\ \rho v u_{\perp} + p n_y \\ (\rho e + p) u_{\perp} \end{bmatrix} - \begin{bmatrix} 0 \\ n_x \tau_{xx} + n_y \tau_{xy} \\ n_x \tau_{yx} + n_y \tau_{yy} \\ n_x \theta_x + n_y \theta_y \end{bmatrix} \tag{2.19}$$

Here, $u_{\perp} = u n_x + v n_y$, $\theta_x = u\tau_{xx} + v\tau_{xy} - q_x$, $\theta_y = u\tau_{yx} + v\tau_{yy} - q_y$. The source terms in Eq. 2.15 can also be handled as,

$$\int_{\Omega} \alpha(\mathbf{S_I} - \mathbf{S_V}) d\Omega = \alpha \ \Omega \overline{\mathbf{S}} \tag{2.20}$$

where $\overline{\mathbf{S}} = \overline{\mathbf{S}}_{\mathbf{I}} - \overline{\mathbf{S}}_{\mathbf{V}}$ is the cell-averaged value of the source term which is also lumped at the centroid of the cell. Using these simplifications, the semi-discrete form of the governing conservation laws can be written as,

$$\frac{d\overline{\mathbf{U}}_i}{dt} = -\frac{1}{\Omega_i} \sum_{J \epsilon i} \mathbf{H}_{\perp_J} \Delta S_J - \alpha \overline{\mathbf{S}}_i = \mathbf{R}(\overline{\mathbf{U}}_i) \tag{2.21}$$

Here, summation is over all faces of the cell i and term $\mathbf{R}(\overline{\mathbf{U}}_i)$ is referred to as the residual term. The semi-discrete flux formula takes into account both the viscous and convective flux contributions, which are both evaluated at the midpoint of the face. This is achieved through the use of a single point Gauss quadrature to evaluate the integral. This approach is crucial in ensuring that the flow solver achieves second-order accuracy.

2.5 Inviscid and viscous flux computations

The evaluation of the convective and viscous fluxes in Eq. 2.19 are discussed as follows:

2.5.1 Inviscid flux discretisation

To compute the inviscid flux, an approximate Riemann problem is solved, which is oriented normal to the interface. There are different flux formulations that can be used, such as central and upwind schemes. In this study, we utilize the van Leer [108] and AUSM [109] schemes.

Solution reconstruction

To achieve nominal second-order accuracy, the states necessary for the approximate Riemann solver must be obtained using a linear reconstruction procedure. However, according to the Godunov Barrier theorem [110], using a simple linear interpolation can result in a loss of

monotonicity. Therefore, to ensure monotonic numerical solutions, slope limiters must be employed, which leads to a limited linear reconstruction. This reconstruction defines the left and right states as follows:

$$V_L = V_i + \psi(\nabla V_i \cdot \mathbf{r}_L) \tag{2.22}$$
$$V_R = V_j + \psi(\nabla V_j \cdot \mathbf{r}_R) \tag{2.23}$$

In the above equation, $\mathbf{r}L$ and $\mathbf{r}R$ represent the vectors pointing from the cell centroid towards the face centroid, as illustrated in Figure 2.4. The variables V_L and V_R represent the primitive variables such as density, velocity, pressure, and temperature, while ∇Vi and ∇Vj represent the gradients of V at the cell centers. The cell centroidal gradient can be calculated using either Standard Green Gauss (SGG) reconstruction [111] or Modified Green Gauss (MGG) reconstruction [112].

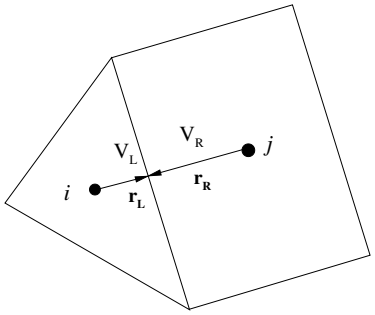

Figure 2.4: Linear reconstruction for the cell centered scheme

In our current solver, we utilize Venkatakrishnan's limiter [111], which ensures good convergence characteristics to steady-state solutions. The limiter function is defined as follows:

$$\psi = \begin{cases} \frac{1}{\Delta^2}\left[\frac{(\Delta_{1,max}^2+\epsilon^2)\Delta_2+2\Delta_2^2\Delta_{1,max}}{\Delta_{1,max}^2+2\Delta_2^2+\Delta_{1,max}\Delta_2+\epsilon^2}\right] & \text{if } \Delta_2 > 0 \\ \frac{1}{\Delta^2}\left[\frac{(\Delta_{1,min}^2+\epsilon^2)\Delta_2+2\Delta_2^2\Delta_{1,max}}{\Delta_{1,max}^2+2\Delta_2^2+\Delta_{1,max}\Delta_2+\epsilon^2}\right] & \text{if } \Delta_2 < 0 \\ 1 & \text{if } \Delta_2 = 0 \end{cases}$$

where $\Delta_{1,max} = V_{max} - V_i$ and $\Delta_{1,min} = V_{min} - V_i$. Here, V_{max} and V_{min} are the maximum and minimum values of all surrounding cells j, including the cell i itself, and are expressed as,

$$V_{max} = max(V_i, max_j V_j)$$

$$V_{min} = min(V_i, min_j V_j)$$

where the term Δ_2 is calculated as,

$$\Delta_2 = |\Delta_2| + 10^{-12} \tag{2.24}$$

Further, the parameter $\epsilon^2 = (K\Delta h)^3$ is the controlling factor for limiting where Δh is a characteristic length scale for the cell. The value of K which is typically chosen between 2 to 10 but an optimal choice depends on the mesh and the problem being solved.

2.5.2 Viscous flux discretisation

Evaluation of the viscous flux at the face requires computations of the first derivatives at the faces. This requires the use of flow quantities at the face mid-points if standard Green Gauss reconstruction is employed. This requires the use of a suitable interpolation procedure and in the present work we use a simple mathematical averaging as defined by,

$$V_J = \frac{1}{2}(V_i + V_j) \tag{2.25}$$

2.6 Temporal discretisation

The governing Ordinary Differential Equations (ODEs) expressed by the semi-discrete finite volume update formula indicated in Equation 2.21 are marched in time using time-marching techniques to obtain the numerical solution. This can be accomplished either until a steady state solution is achieved or for a finite time in the case of unsteady problems. For our current investigation, we employ an explicit time integration scheme that includes the first-order accurate Euler method as well as the more precise Runge-Kutta technique with higher accuracy levels [111]. The first-order accurate Euler method is utilized solely for steady state problems and gives rise to a fully discrete finite volume update that can be expressed as follows:

$$\mathbf{U}_i^{n+1} = \mathbf{U}_i^n - \frac{\Delta t}{\Omega_i} \sum_{J \epsilon i} \mathbf{H}_{\perp J} \Delta S_J - \alpha \overline{\mathbf{S}}_i \tag{2.26}$$

$$\mathbf{U}_i^{n+1} = \mathbf{U}_i^n + \mathbf{R}(\overline{\mathbf{U}}_i)^{(n)}$$

where the quantity n and $n+1$ refer to the current and next time step.

2.7 Boundary conditions

It is well known that CFD results are quiet sensitive for boundary conditions (BCs), and this choice should be decided accurately according to the simulation requirements. For this

purpose, the required boundary conditions are integrated in the in-house CFD solver. These boundary conditions are mentioned here for clarity.

2.7.1 Sonic inlet BC

This kind of BC is used to set the sonic conditions at the inlet of the computational domain. Here, unity Mach number is set along with the critical temperature and pressure (T^* and P^*). It is to be mentioned that the sonic line at this boundary is assumed to be a straight line (the shape of the boundary), and this assumption is widely used in other methods like the Method of Characteristics [67].

2.7.2 Pressure outlet BC

For a complex flow structure that contains subsonic, transonic, and supersonic/hypersonic regions, it is hard to anticipate the flow region at the domain outlet. Therefore, strongly averaged pressure outlet BC is imposed at the outlet of the domain. That is, the static pressure is fixed at the desired value, another flow parameter (temperature in this case) is extrapolated from the cell center adjacent to the boundary, and the density is calculated using the equation of state. Figure 2.5 illustrates the implementation of pressure outlet BC at the domain exit.

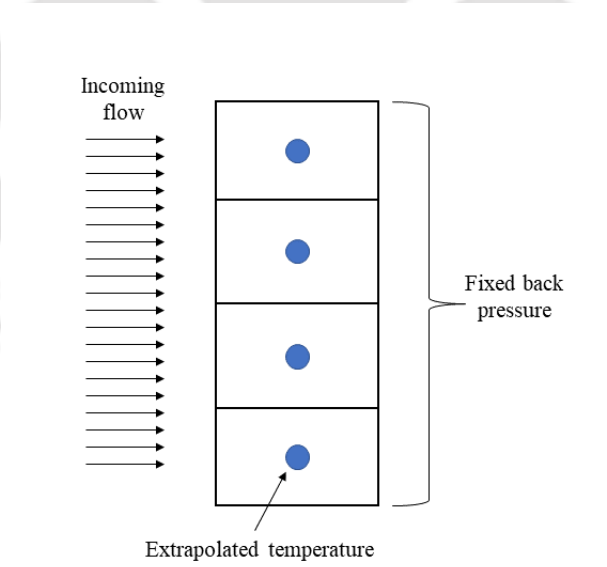

Figure 2.5: Strongly averaged pressure outlet condition.

2.7.3 Pressure inlet BC

To study the effects of the subsonic inlet conditions on the supersonic region of the flow, one has to consider the boundaries from which the flow originates. Hence, in some cases,

the flow inlet is considered to have zero velocity, which corresponds to total conditions, and therefore, the total temperature T_0 and pressure P_0 are imposed at this boundary along with zero velocity.

2.7.4 Wall BC

The wall boundary condition is treated in two manners:

- Viscous wall (No-slip): It is achieved by setting the normal and tangential velocities at the wall to be zero. It is worth to note that, the viscous wall boundary condition, from the perspective of velocity field, actually refers to thermally adiabatic wall in the present case, since the wall temperature gradient is set to zero while imposing this boundary condition.
- Inviscid wall: Imposing this boundary condition is done following the approach of pressure gradient extrapolation, where the normal velocity is set to zero in the inviscid flux.

2.7.5 Symmetry BC

Only half portion of the domain is considered for simulation, in all the current simulations, since it reduces the computational cost of a simulation. For implementing this boundary condition, the velocity normal to the domain boundary (axis of symmetry) is set to zero.

2.8 Conclusions

A novel one-dimensional solver based on the simple gas dynamic relations is developed successfully and then integrated with the steepest descent based optimisation solver. In-house CFD solver is also tuned appropriately to probe the two-dimensional axisymmetric flow field of sonic/supersonic jets.

CHAPTER 3

UNDEREXPANDED SONIC FREEJET

Abstract

Studying the underexpanded jet has been essential for many fields of research as it might occur intentionally or spontaneously wherever a high-speed gas flow is possible. Therefore, an in-house compressible flow solver is employed to simulate an underexpanded sonic freejet. The behavior of the jet is examined in the near-field area, immediately downstream of the nozzle exit plane, to determine the parameters influencing the characteristics of the jet. Mach reflection phenomenon is thoroughly studied and a criterion is defined for the transformation from regular reflection to Mach reflection. Further, the location and height of Mach disk are found to be governed by exit pressure ratio, stagnation temperature, and the type of gas used. Although the temperature does not have a significant impact, the pressure ratio and specific heat ratio (γ) are found to affect the jet structure. The results obtained from the solver are compared with existing experimental results, highlighting the utility of the solver in probing the compressible flow fields.

3.1 Introduction

Underexpansion is a phenomenon that occurs when a gas exits a duct with higher pressure than the back (or ambient) pressure [21]. It is widely found in engineering and research applications such as aerodynamic testing, rocketry, chemical reactions [57], applied physics [56], and even when popping a champagne bottle [113]. This chapter studies the changes that impact the underexpanded sonic jet for diverse boundary conditions, it highlights the role of pressure ratio, temperature, and gas type in altering the location and height of Mach disk. Correlations that are coined previously are closely investigated and compared with the current results and the simulations are found to be useful in probing the near-field area. The influence of pressure ratio is seen to be in good agreement with the literature [11–14]. The ratio of specific heats is also found to govern the flow features, even though it is stated

otherwise in the literature [15, 16, 33, 34]. Moreover, the temperature is considered in the analysis as a driving parameter to examine its effect on the jet structure. For this matter, Section 3.2 shows the computational domain and the mesh independence study, Section 3.3 explains the flow properties, Section 3.4 investigates the transformation from regular reflection to Mach reflection, Section 3.6 examines how Mach disk location changes with gas properties, Section 3.7 studies the influence of these properties on Mach disk diameter, and Section 3.8 concludes the findings.

3.2 Computational domain

A judicious choice for the dimensions of the computational domain is essential as it influences the accuracy of the solution, especially in high-speed flows. The domain is limited to the area downstream of the nozzle exit, which implies the assumption of contoured converging nozzle that delivers a uniform jet. This assumption can be validated by comparing two simulation results from two domains, with and without the nozzle, considering the exact reservoir conditions in both of them. The numerical schlieren images for these simulation are compared in Fig. 3.1. One can notice that there is no fundamental difference between these two results, i.e., the flow profile at the throat of the orifice has no significant effect on the structure downstream. This allows us to neglect the contoured converging nozzle in the considered domain.

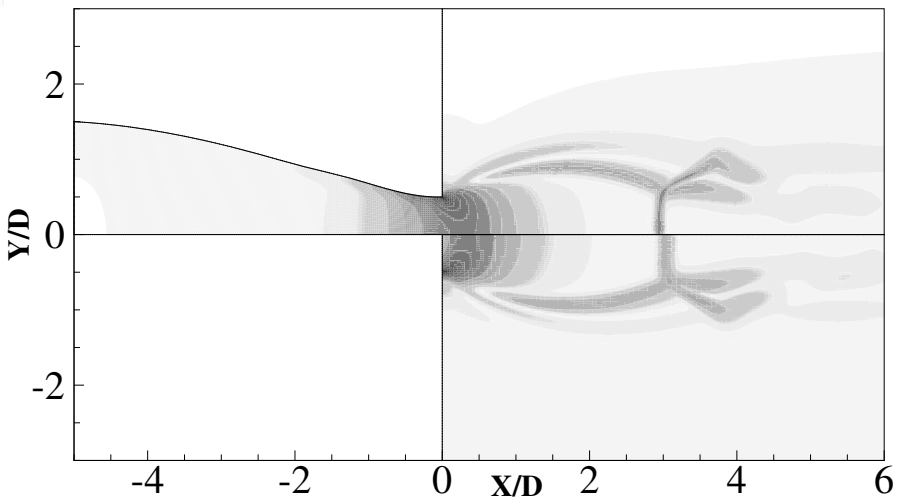

Figure 3.1: Numerical schlieren images for two domains, with a nozzle (upper), and without a nozzle (lower).

The size of the domain is extended to $150D$ in length and $50D$ in width as suggested in the literature [32]. The boundary conditions are shown in Fig. 3.2 where the inlet is set to be at sonic conditions, and the outlet is maintained at a fixed pressure to attain the intended

exit pressure ratio. Bottom wall of the domain is considered as symmetry axis to account for axisymmetricity of the flow and to reduce the computational cost. The complete domain is initialized with the ambient conditions corresponding to the exit-to-back pressure ratio and 300K temperature.

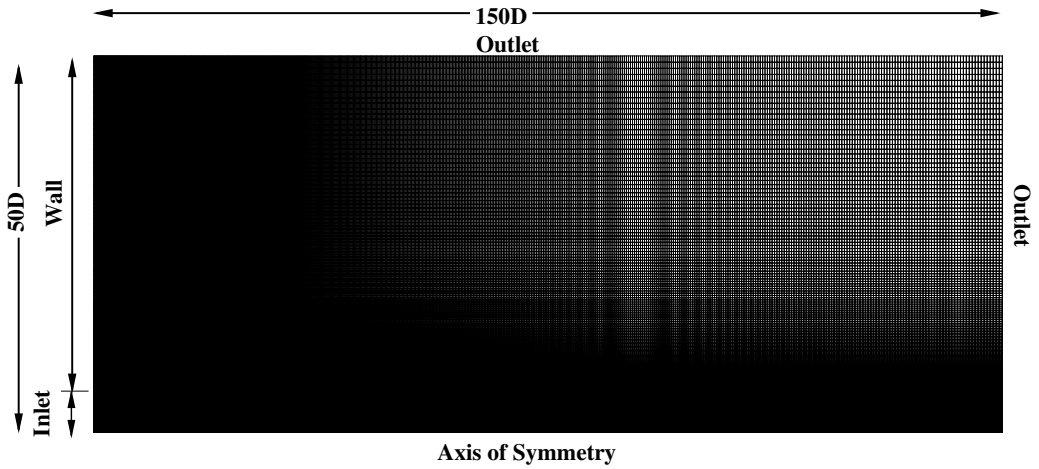

Figure 3.2: Domain and mesh used for the simulations.

Particular care was taken while meshing the domain; the very first mesh considered has the size of 400 nodes along the stream-wise direction and 150 nodes in the normal direction. This mesh is then refined to a level of 800 × 300 nodes, and then to the size of 900 × 330 nodes. Figure 3.3 (a) shows the pressure distribution along the axis using the aforementioned meshes for air free-jet with an exit pressure ratio of 7.0. The distribution is seen to conform along the axis throughout the potential core area. However, a slight change in the solution is noted between the first two meshes at the location of Mach disk, while the distribution becomes independent of the mesh for the latter two. The qualitative difference in the steady state solution obtained in terms of Mach number contours is shown in Fig. 3.3 (b) considering the near-field area for these meshes (900 × 330 and 800 × 300). A good agreement is noticed between their solutions. Hence, the mesh of size 800 × 300 nodes is chosen here-onwards for further analysis with respect to computational time and accuracy of solution.

3.3 Simulation setup

The simulations have been carried out to target the underexpanded sonic jet for Argon as a monoatomic gas ($\gamma = 1.667$), air as a diatomic gas ($\gamma = 1.4$), and carbon dioxide as a triatomic gas ($\gamma = 1.27$) using the in-house laminar compressible flow solver. These simulations are expected to help in the proposed objective of dependence of jet structure on fluid properties. Here, the exit pressure ratio (P_e/P_b) takes different values from 1.5 to 20.0 for each gas. In each case, the static sonic temperature is also varied between 300K and

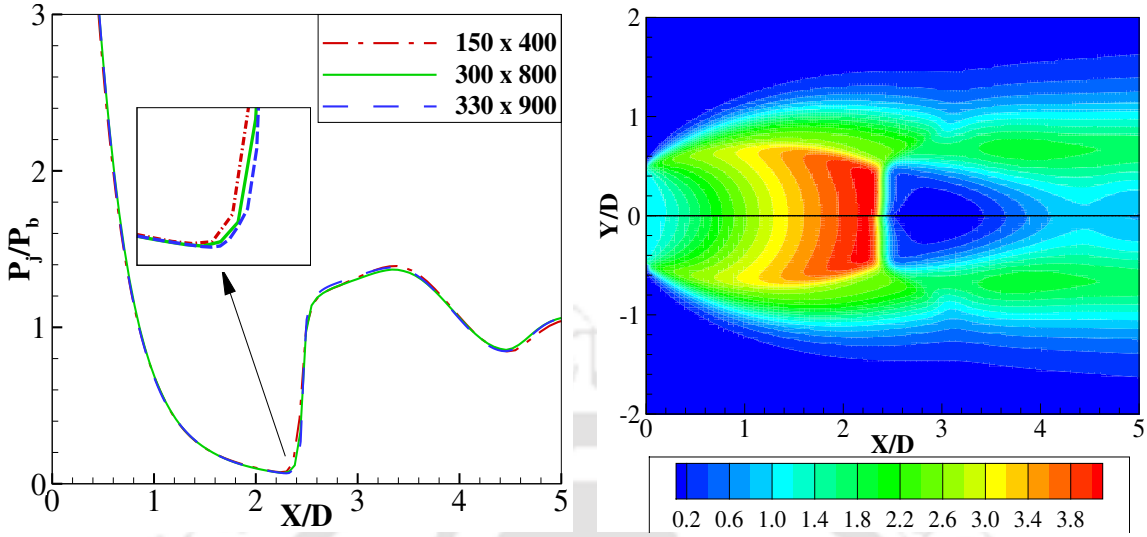

(a) Axial pressure distribution for the three meshes.

(b) Mach number contours for 900 x 330 mesh (top) vs. 800 x 300 mesh (bottom).

Figure 3.3: Mesh independence analysis.

1000K, keeping the higher exit pressure ratio constant as 20.0. The results obtained from these simulations are then analyzed towards present objectives. It may be noted that, for simulation of higher total temperature, perfect gas assumption is expected to be valid due to weak independence of specific heat on temperature [114].

3.4 Apparition of Mach disk

As illustrated in Figs. 1.3, 1.4 and 1.5, underexpanded jet develops different elements and jet structure according to the exit pressure ratio. Hence, further understanding of Mach disk is essential in terms of its appearance and growth. As the jet exits the nozzle, it undergoes the expansion process by decreasing the pressure and increasing Mach number. The presence of oblique shock and its regular reflection from the axis, which is prominent in the underexpanded jet, transforms to Mach reflection at higher values of governing exit pressure ratios. It can be expected that the point of transformation from regular reflection (RR) to Mach reflection (MR) corresponds to zero height (diameter) of Mach disk. Thus, a literature reported correlation given by Eq. (1.3) is utilized to predict the critical value of total pressure ratio beyond which the regular reflection becomes Mach reflection or below which Mach disk does not exist. Hence, for this critical pressure ratio, value of D_M/D is considered to be zero. The total pressure ratio P_0/P_b in this case corresponds to 3.9, which generates a different value of the exit pressure ratio P_e/P_b for each value of γ. Using the isentropic relations [67], the exit pressure ratio values are: 1.9 for Argon, 2.0 for air and 2.15 for CO_2. For the total pressure ratios of value equal and above the critical pressure ratio, Mach disc is expected on the jet axis and the Mach number immediately downstream of it falls to unity or below. Hence, the apparition of Mach disk can be anticipated by plotting Mach number

distribution along the jet axis. In order to certify this proposal, simulations are performed, using the in-house solver with laminar model, around the critical pressure ratios. In the case of carbon dioxide ($\gamma = 1.27$), the simulations are performed for the exit pressure ratios of $1.5, 1.9, 2.15, 2.3$ and 2.5. For air, the simulations are done for $1.5, 1.7, 2.0, 2.25$ and 2.5 pressure ratios, and for Argon, $1.5, 1.7, 1.9, 2.1$ and 2.3. All the simulations are carried out for a sonic inlet temperature of 300K.

The results are shown in Fig. 3.4 for the three gases. Here, a horizontal line is drawn at

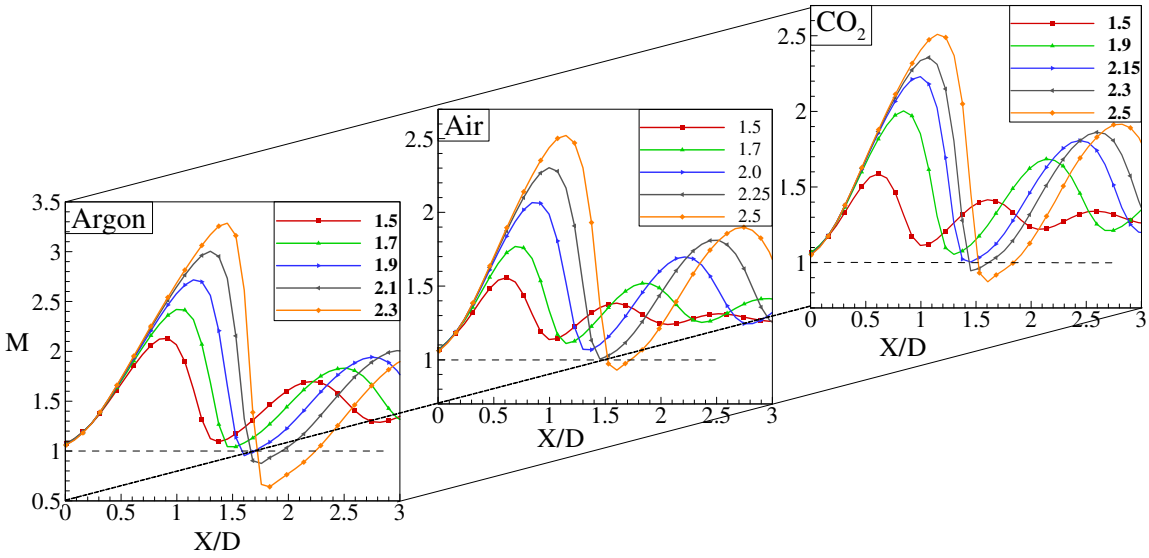

Figure 3.4: Mach number distribution along the jet axis for three gases at different pressure ratios.

$M = 1.0$ as a reference for the normal shock case. Axial Mach number distribution in the carbon dioxide jet appears to intersect with the unity line at an exit pressure ratio of PR = 2.15, which is the critical pressure ratio obtained from Eq. (1.3), while air and Argon at a pressure ratios 2.25 and 1.8, respectively. Thus, the suggested criterion appears to be utilizable in determining the transformation for underexpanded sonic jet.

To further comprehend the difference between regular reflection and Mach reflection, numerical schlieren images are shown in Fig. 3.5 for the three gases around the respective critical pressure ratios to analyse the corresponding RR and MR cases. Figure 3.5 shows that the regular reflection is clear at pressure ratios lower than the critical, and Mach reflection is clear at higher pressure ratios. It can be noted here that, by increasing γ, Mach reflection tends to occur at a lower pressure ratio as it happens first for Argon, air and then carbon dioxide, which agrees with the literature [115, 116]. This observation is consistent with the critical pressure ratio values obtained from correlation for different gases. The gas with higher specific heat ratio expands more and attains higher Mach number along the axis, just upstream of shock reflection point, at a given exit pressure ratio. Although maximum flow deflection angle, for a given Mach number, is lower for a gas of higher specific heat

ratio, higher axial Mach number at lower governing pressure ratio ultimately leads to early transition from RR to MR for this gas. This gas dynamic analysis justifies the transition of RR to MR in the order as Argon, air and carbon dioxide.

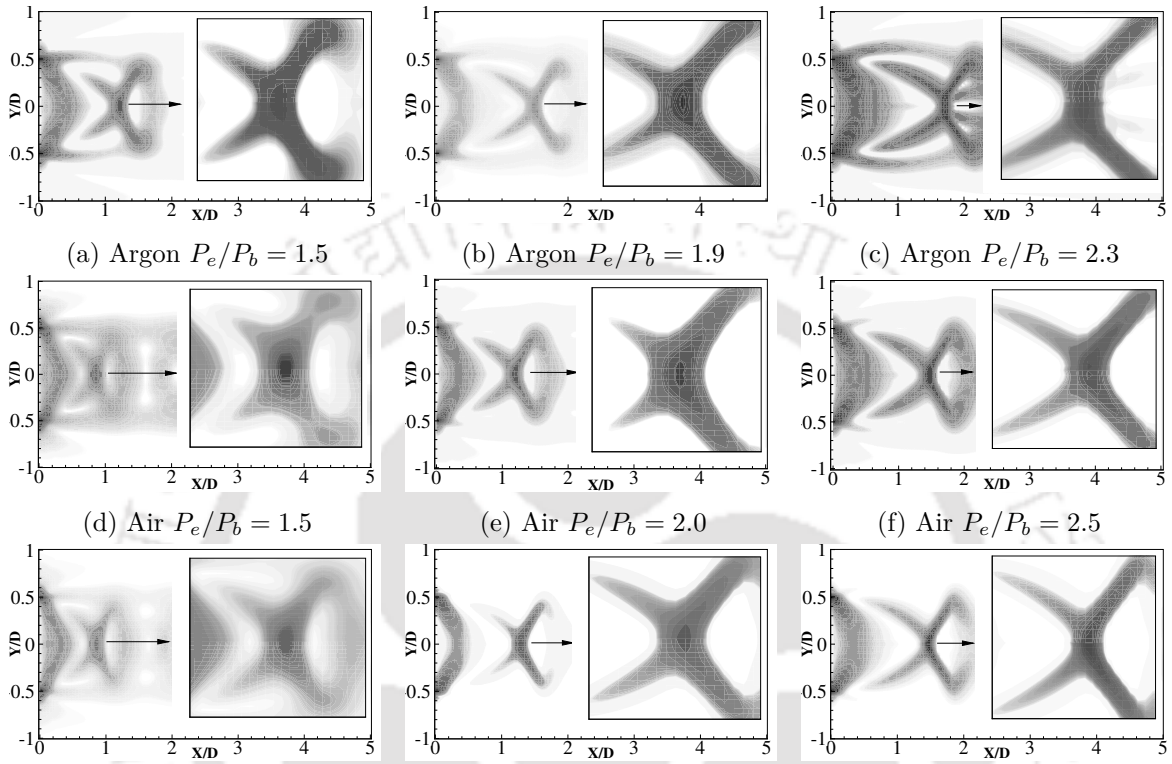

(a) Argon $P_e/P_b = 1.5$ (b) Argon $P_e/P_b = 1.9$ (c) Argon $P_e/P_b = 2.3$

(d) Air $P_e/P_b = 1.5$ (e) Air $P_e/P_b = 2.0$ (f) Air $P_e/P_b = 2.5$

(g) CO_2 $P_e/P_b = 1.5$ (h) CO_2 $P_e/P_b = 2.15$ (i) CO_2 $P_e/P_b = 2.5$

Figure 3.5: Numerical schlieren images for Argon, air and CO_2 at RR case, MR case and critical case.

3.5 Effect of turbulence

The results of the laminar flow model show a well alignment with the existing literature. However, the complexity of the flow requires further investigation towards the turbulence effects on the solution. Therefore, simulations are performed for three different exit pressure ratios using $k - \epsilon$ model of the commercial software ANSYS Fluent. The simulation is performed using AUSM scheme with second order accuracy, ideal gas assumption, and Sutherland's law for viscosity calculation. The simulations consider viscous Navier-Stokes equation, the equation of state, and the system is closed with $k - \epsilon$ turbulent model. It is to be mentioned that a turbulent flow acquires more diffusion and dissipation than the laminar flow. The results have come out to support this claim where the shear layer is more diffused. Figure 3.6 describes the radial distribution of axial velocity (u) at the location of highest Mach number. This location refers to the point exactly upstream of the reflection point on the axis, and it is plotted at three pressure ratios for both laminar and turbulent flows to

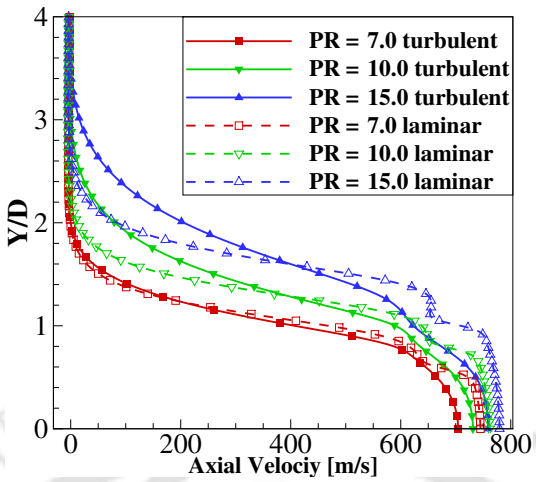

Figure 3.6: Radial distribution of axial velocity at the location of highest Mach number.

discriminate the differences. Looking at Fig. 3.6, one can notice an increase in the relative area covered by shear layer in the turbulent case with respect to the total area of the jet.

For another aspect of the effects, Mach number contours are plotted in Fig. 3.7. The comparison is taken at three different pressure ratios, 7.0, 10.0, and 15.0, for the turbulent and laminar models. In spite of the difference in shear layer growth and the weaker barrel shock, the flow seems to retain the location of the reflection point. It is obvious from Fig. 3.7 that, the laminar jet is allowed to expand more freely than the turbulent one, and it attains a higher Mach number immediately upstream the reflection point (Mach disk location). On the other hand, the turbulent flow seems to be pushed towards the axis by the shear layer as it grows downstream. This effect reduces the height of the inviscid core including the normal shock, and restricts the expansion of the flow. Hence, for Mach reflection to occur, it would require higher pressure ratios. Therefore, turbulent flow holds the regular reflection for a wider range of pressure ratios, i.e., turbulence delays the occurrence of Mach disk. Eventually, the inviscid core is terminated when the shear layer meets the axis, which happens at the same location for both of the models.

3.6 Mach disk location

Location of Mach disk decides the axial boundary of the inviscid core. Therefore, it has attracted the interest of many researchers to conduct experiments and perform simulations to come up with a clear correlation which could predict its location. It is the point at which the supersonic flow becomes subsonic after passing through a normal shock, and it determines the end of inviscid core area which is of high importance for laboratory experiments. Further, Mach disk location plays an important role in the thrust optimisation and thrust vector control in rockets. The normal shock location can be gauged from the axial distribution of Mach number, since the Mach number variation would become discontinuous in the presence of Mach disk. Tejeda et al. [117] have developed a correlation given in Eq. (3.1) to determine

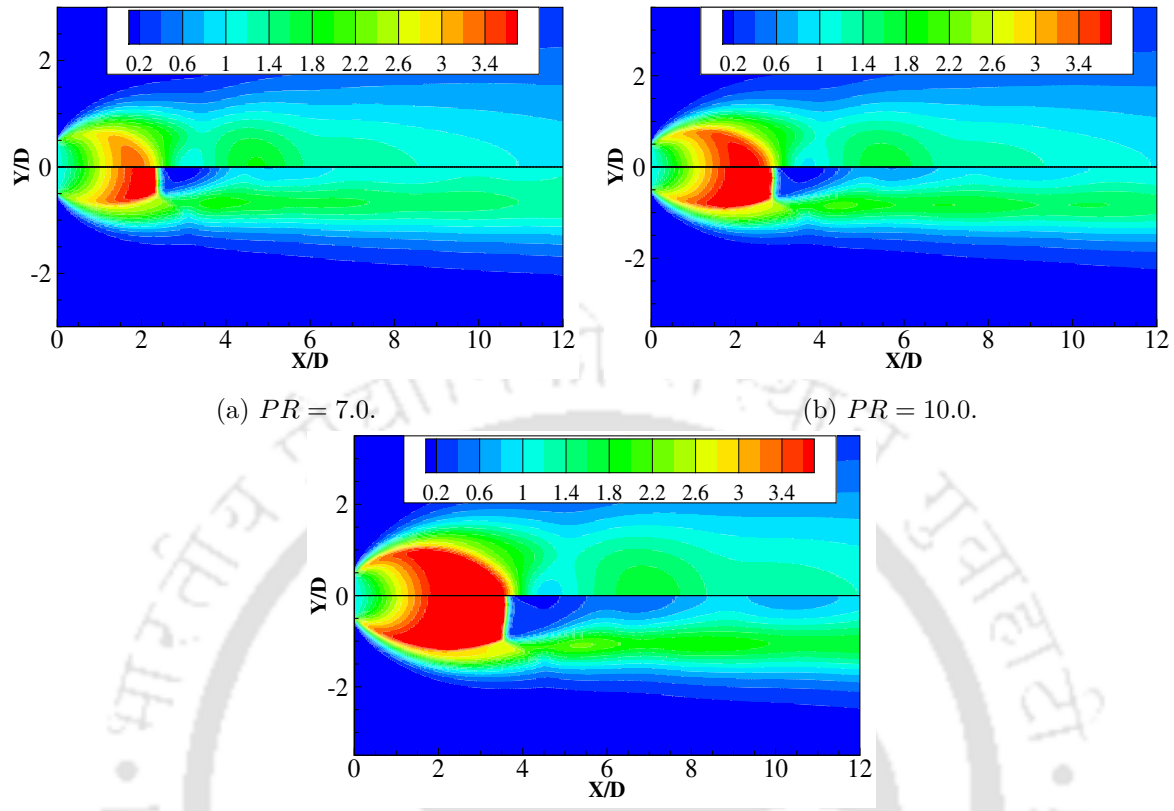

(a) $PR = 7.0$. (b) $PR = 10.0$.

(c) $PR = 15.0$.

Figure 3.7: The effects of turbulence (upper) and laminar (lower) regimes on Mach contours for three exit pressure ratios.

Mach number distribution along the jet axis:

$$M = (\frac{X}{D})^{(\gamma-1)}(b + \frac{c}{X/D} + \frac{d}{(X/D)^2} + \frac{e}{(X/D)^3}) \tag{3.1}$$

where b, c, d and e are coefficients related to γ as follows:

$$b = 16.5404 - 15.8215\gamma + 4.7018\gamma^2$$

$$c = -15.6286 + 15.1459\gamma - 3.7335\gamma^2$$

$$d = 13.1705 - 14.4312\gamma + 4.0591\gamma^2$$

$$e = -3.4116 + 3.7898\gamma - 1.0720\gamma^2$$

Although this expression describes the evolution of Mach number along the axis for each γ value, it does not predict the location of the normal shock. This distribution is plotted in Fig. 3.8 along with the current in-house solver results for air at different exit pressure ratios. The figure shows that Eq. (3.1) depicts Mach number distribution for an infinite pressure ratio, whereas the lines of the present simulations drastically drop at the location

of Mach disk. However, in the region of expansion upstream of the Mach disk, all the lines match consistently and conform with the line from Eq. (3.1). This figure provides accuracy of present computations in the inviscid core of the jet. Further, the location of Mach disk is also evident from this figure. Hence, this process is followed for each gas and for each condition of simulation.

It is essential to evaluate the effect of pressure ratio, temperature and specific heat ratio (γ),

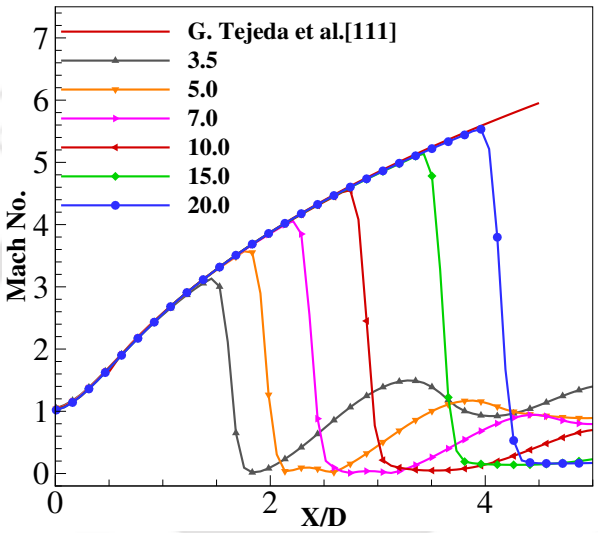

Figure 3.8: Mach number distribution along the jet axis for air.

to get a clear idea about their influence on the location of Mach disk. The present solver is employed to simulate the air free jet flow at chosen exit pressure ratios between 2.5 and 20.0 and the results are processed to estimate Mach disk location as the first abrupt jump in the pressure along the jet axis. These results are compared with Eq. (1.2) and the experimental results of Wilkes et al. [30] in Fig. 3.9 as the air and nitrogen are both considered as diatomic gases ($\gamma = 1.4$). This figure clearly portrays the accuracy of the present simulations.

For the aforementioned purpose, many simulations are carried out while fixing two parameters and altering the third, among the pressure ratio, total temperature and γ, to create a new case. These simulations are as many as 45, including the turbulent model simulations. The behavior of each gas with driving pressure ratio is examined by maintaining the sonic conditions at the inlet and gradually increasing the exit pressure ratio from 2.5 to 20 from one simulation to another. Figure 3.10 shows the variation of non-dimensional Mach disk location with the exit pressure ratio for the three gases with sonic state temperature of 300K at the inlet, which corresponds to stagnation temperature of 400K, 360K and 340K for Argon, air and carbon dioxide, respectively. Here, the distance of Mach disk from the nozzle exit is non-dimensionalised with the orifice exit diameter D, and compared with the correlation proposed by Driftmyer [31]. It is clear from the figure that the present estimates and the same obtained from Eq. (1.2) agree in the range of low pressure ratios and start diverging when it is increased. Figure 3.10 shows a deviation between the results obtained

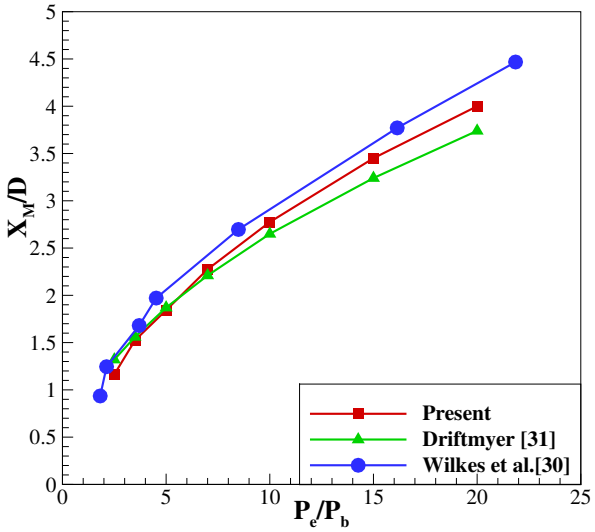

Figure 3.9: Mach disk location vs. exit pressure ratio for air (comparison).

from the present solver and the experimental correlations when adapted for Argon and CO_2, nevertheless, this deviation is minimum in the case of air. It may be noted that in the experiment of Driftmyer [31], air is used at total pressure ratio between 29.4 and 915.6. Then, the correlation reported in Eq. (1.2) is derived and concluded from the experimental results in this interval and generalised for other gases. Hence, the discrepancy between the computational results and results obtained from Eq. (1.2) might be attributed to the fact that the experiments were conducted for air at high pressure ratios, whereas the present work is concerned with moderate-to-high underexpanded sonic jet for three different gases with the assumption of perfect gas. Therefore, the computational results are useful in extending the limits of this correlation.

Thus, present results are found to be valid in predicting the Mach disk location beyond the

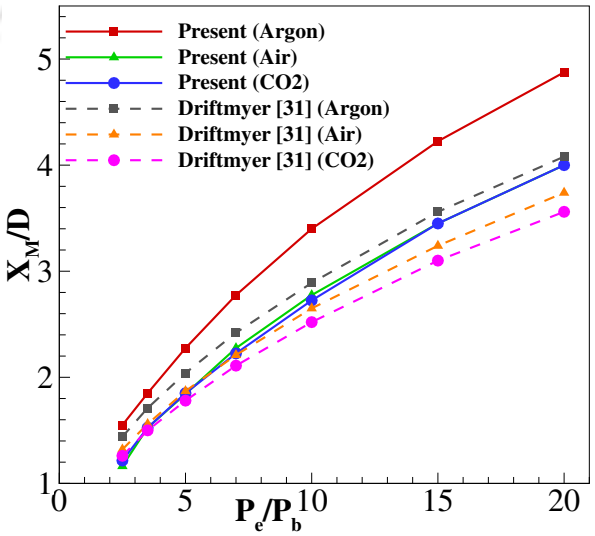

Figure 3.10: X_M/D vs. P_e/P_b for the present work and Driftmyer [31].

range of an established correlation. One can notice from Fig. 3.10 that a higher pressure ratio pushes Mach disk further downstream in the three cases of γ which agrees well with Eq. (1.2). It is also remarkable that for a certain exit pressure ratio, Mach disk is noticed to move downstream as γ increases, which is also explicitly shown in Eq. (1.2). Further, the rate of increase of Mach disk location in the range of higher pressure ratio (10.0 to 20.0) is noted to be slightly lower than the rate in the range of low pressure ratio (2.5 to 5.0) for the three gases. That is, a 100% increase in pressure ratio (2.5 to 5.0) moves Mach disk by 47%, 58%, and 52% for Argon, air, and CO_2, respectively. Whereas, a 100% increase in pressure ratio (10.0 to 20.0) moves Mach disk by 43%, 44%, and 47% for Argon, air, and CO_2, respectively . Hence, the slope of the lines in Fig. 3.10 is noted to decrease with the increase in pressure ratio for all the gases.

Then, the exit pressure ratio is fixed to the value of 20.0 and the sonic temperature is gradually increased from 300K to 1000K for each gas. The axial pressure distribution is plotted in Fig. 3.11 for all the three gases at different operating temperature. It is noticed from Fig. 3.11 that the stagnation temperature has no significant impact on the location of Mach disk at a certain pressure ratio for Argon, air or carbon dioxide up to 1000K sonic temperature. This finding agrees well with the theory that the shock cell structure mainly depends on the exit pressure ratio of the jet. It is an important conclusion of the present investigations which has been less attended. Thus, Mach disk location seems to be insensitive to reservoir temperature.

It is to be mentioned that, immediately downstream of Mach disk, the jet pressure attains

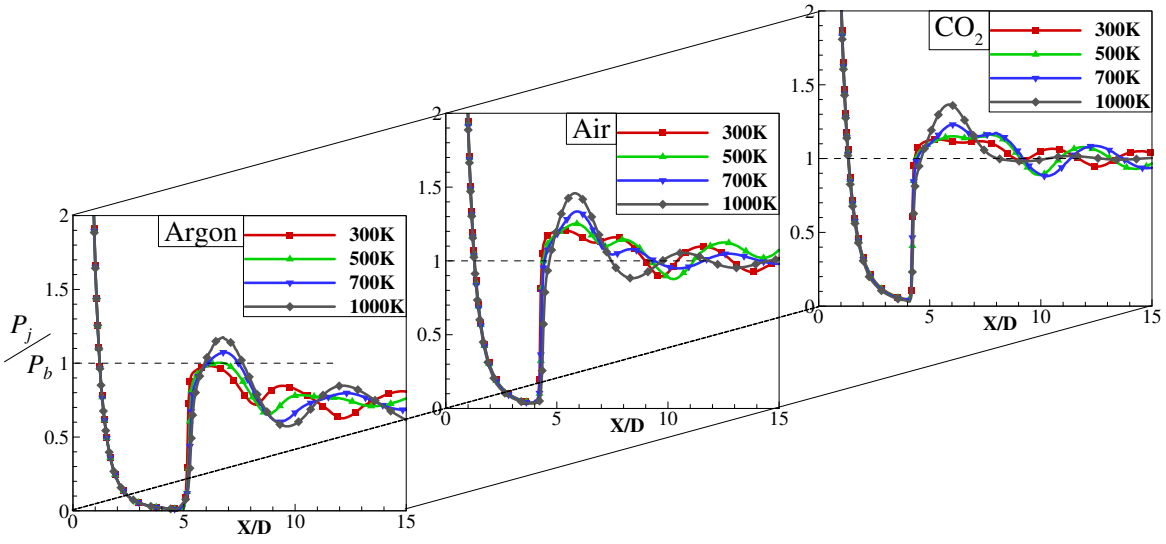

Figure 3.11: Near-field axial pressure distribution for the three gases at different temperatures.

the ambient pressure which is lower than the inlet (sonic) pressure, i.e., the jet-to-back pressure ratio becomes around 1.0 with a minor deviation. Presently obtained results (Fig. 3.11)

also agree well with the theoretical hypothesis [11]. However, the jet temperature is seen to exceed the inlet temperature after crossing the Mach disk, and the flow clearly becomes subsonic. Here, the loss in the kinetic energy, in comparison with the inlet, is compensated by a rise in the internal energy beyond the Mach disk. It is worth to note that, the pressure ratio almost attains unity beyond the Mach disk which suppresses convection but the local higher temperature enhances the diffusion in the flow which in turn broadens the shear layer.

3.7 Mach disk diameter

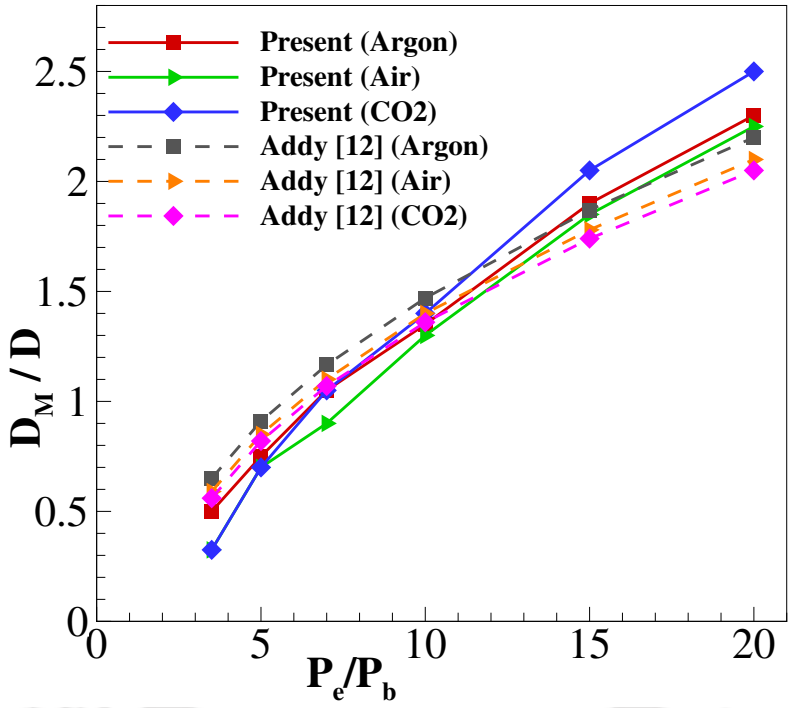

Figure 3.12: D_M/D vs. P_e/P_b for the present work and Addy [12]

Another important dimension in the structure is the height or diameter of the first normal shock, or the area of jet which passes through a normal shock from a supersonic/hypersonic state to a subsonic state. The height of the normal shock determines the fraction of the jet that becomes a subsonic region downstream, and also determines the radial dimension of the inviscid core. Further, Mach disk height affects the jet acoustic properties, noise dynamics and frequency. The in-house solver is employed to estimate the height in the present work. Researchers have identified the parameters which affect the diameter as pressure ratio [12, 13, 15], exit Mach number [13, 31, 34, 118], specific heat ratio [16, 18] and nozzle geometry [12, 13, 15, 27, 32]. However, it could be argued that it is not related to exit Mach number [44, 45], and hence the scope of this work is limited to only the sonic jets. The same approach followed to find the Mach disk location is employed here as well to understand the influence of the gas nature and flow properties on the Mach disk diameter. Figure 3.12

shows the influence of γ and exit pressure ratio on the diameter of Mach disk. It is noticed that varying γ does not significantly affect the diameter. However, it is worth mentioning that, at moderately underexpanded jets, argon with higher γ has the higher value of D_M/D, followed by air and carbon dioxide, respectively. Nevertheless, Mach disk diameter for carbon dioxide increases rapidly as the pressure ratio increases and holds the higher value of D_M/D for extremely underexpanded jets. The difference between the results of the present work and the experiment of Addy [12] varies from 4% to 42%. Those experiments [12] were conducted using air as a flowing gas at low total pressure ratios ($1 < P_0/P_b < 10$), which correspond to exit pressure ratios of $0.528 < P_e/P_b < 5.28$, and then used to construct the correlation reported in Eq. (1.3), which could be extended to include other gases. Hence, the contradiction between the simulation results and the results obtained from the correlation is attributed to the different pressure ratio ranges and different gases used. Here as well, it must be noted that, the computational simulations are useful to propose the amendment in the correlations to enlarge the envelop of their usefulness.

Further, the temperature impact on the diameter is studied by fixing the exit pressure ratio

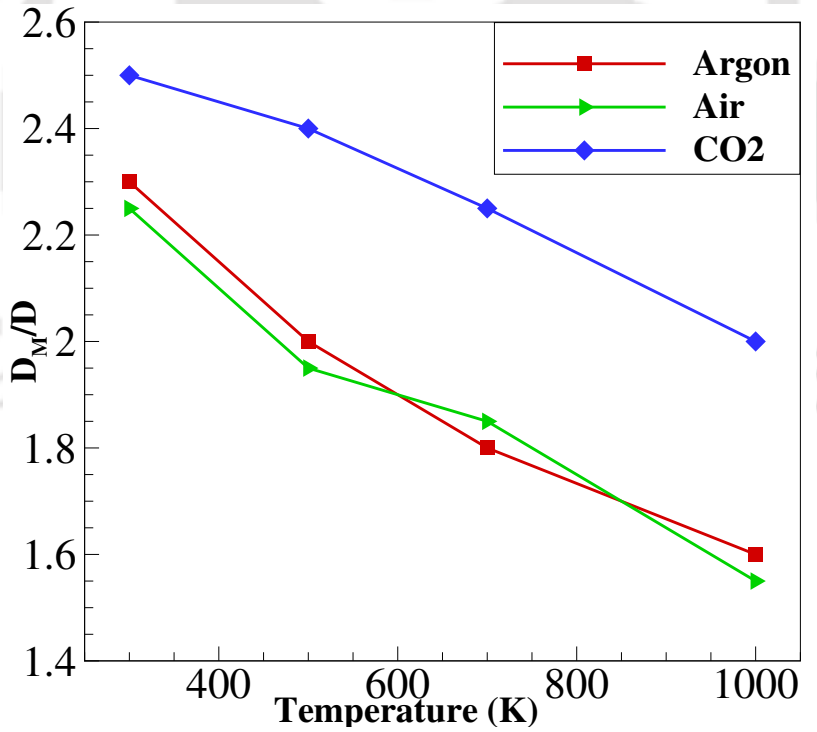

Figure 3.13: The impact of temperature on the diameter of Mach disk for the three gases.

for each gas at 20.0 and gradually increasing the total temperature from one simulation to another. The relation between the diameter of Mach disk and the inlet temperature is plotted in Fig. 3.13 which illustrates this relation for the three gases as it shows that increasing the temperature decreases the shock height for all the gases. This effect can be attributed to the fact that higher temperature causes more diffusion in the flow, which increases the thickness of shear layer, and hence, compresses the potential core further towards the jet

axis. This process causes a reduction in Mach disk diameter and overall jet height. This recommendation, which is also unexplored, is marked to be important to understand the gas dynamics of the free-jet.

3.8 Conclusion

This chapter deals with the underexpanded jet from sonic orifice. The laminar flow model is validated comparing with existing literature, and the turbulent simulations are done using ANSYS Fluent. The flow parameters, pressure ratio, stagnation temperature, and the nature of the gas, are varied throughout the simulations to understand their individual influence on the jet structure. Increasing the exit pressure ratio is mainly seen to transform the jet from slightly to moderately and then extremely underexpanded jet, subsequently, the formation of Mach disk and the transition from regular reflection to Mach reflection. Thus, the apparition of Mach disk is noted to be dependent on the pressure ratio and the specific heat ratio γ as it appears first for gases with high γ values. The distance between the nozzle exit plane and the first normal shock is seen to increase with the pressure ratio and γ. The increment in the location keeps a rate in the range $43\% - 58\%$ with an increase of 100% in the exit pressure ratio for the three gases. Such simulations are found to be useful to improve and incorporate necessary amendment in the existing correlations which would have been obtained from numerous experiments. The impact of the stagnation temperature on the location of Mach disk is almost unnoticeable in the considered range of temperature. Further, it is observed that the pressure immediately downstream of Mach disk almost matches the back pressure with an accepted deviation, whereas the temperature rises above the inlet temperature and the ambient temperature which not only compensates for the loss in kinetic energy but also enhances the diffusion. The diameter of Mach disk is studied with different pressure ratios, temperature, and gases. It is found to be proportional to the pressure ratio and inversely proportional to the total temperature, whereas the gas type does not affect the diameter remarkably. Current studies are found to be useful in exploring the dynamics of freejet and its dependence on various parameters.

CHAPTER 4

THE INFLUENCE OF UPSTREAM GEOMETRY

Abstract

The underexpanded sonic and supersonic jets have been widely studied due to their importance for many applications, such as rocketry, aerodynamics, physics, and chemistry. It has been mentioned that the pressure ratio is the main driving parameter in determining the dynamics of such jets. In this chapter, a numerical analysis is carried out to examine how the settling chamber dimensions and geometrical configurations can affect the structure of the underexpanded sonic jet. In this context, the location and diameter of Mach disk are examined for different nozzle geometries. The location and curvature of the sonic line are also highlighted.

4.1 Introduction

It is evident that nozzle wall shape influences the flow structure within and downstream the nozzle exit [43]. Having examined sonic freejets properties depending on the fluid parameters in Chapter 3, one should consider the effects of upstream geometry on the evolution of jet downstream the throat [27, 46]. For that purpose, this chapter is dedicated to investigate how the settling chamber shape, and sonic orifice shape would affect the flow in the near-field area. Nine sonic nozzle geometries are addressed, including straight nozzle, conical converging nozzle, round contoured nozzle, and sharp-edged orifice. Using Euler's equations exposes the geometrical effects without considering the viscous effects, and highlights the Mach disk location and diameter, in addition to the location and curvature of the sonic line. Therefore, Section 4.2 depicts the general shape of the domain employed in the simulations and the imposed boundary conditions, Section 4.3 elaborates the geometry of the different nozzles that are examined, Section 4.4 deals with the location of Mach disk resulting from these nozzles, Section 4.5 deals with the diameter of Mach disk, Section 4.6 sheds the light on the influence of geometry on the sonic line at the nozzle throat, and finally, Section 4.7

summarises the important findings of this chapter.

4.2 Computational domain and boundary conditions

The computational domain, to study the effects of upstream geometry on the freejet, comprises of the settling chamber, sonic nozzle, and 5 nozzle diameters downstream to capture the near-field region. The inlet is treated as zero-velocity boundary condition with the stagnation pressure and temperature. At the outlet, the pressure is strongly averaged, i.e., a fixed back pressure is set, the temperature is extrapolated from the domain, and the density is calculated as per equation of state. This treatment accommodates both subsonic and supersonic outlet conditions. Such computational domain is shown in Fig. 4.1. The solution is ensured to be independent of the mesh, where mesh is clustered within the nozzle and in the near-field area to capture the jet expansion, shock waves, and other flow features.

The boundary conditions considered for all the simulations are as follows: Nozzle Pressure

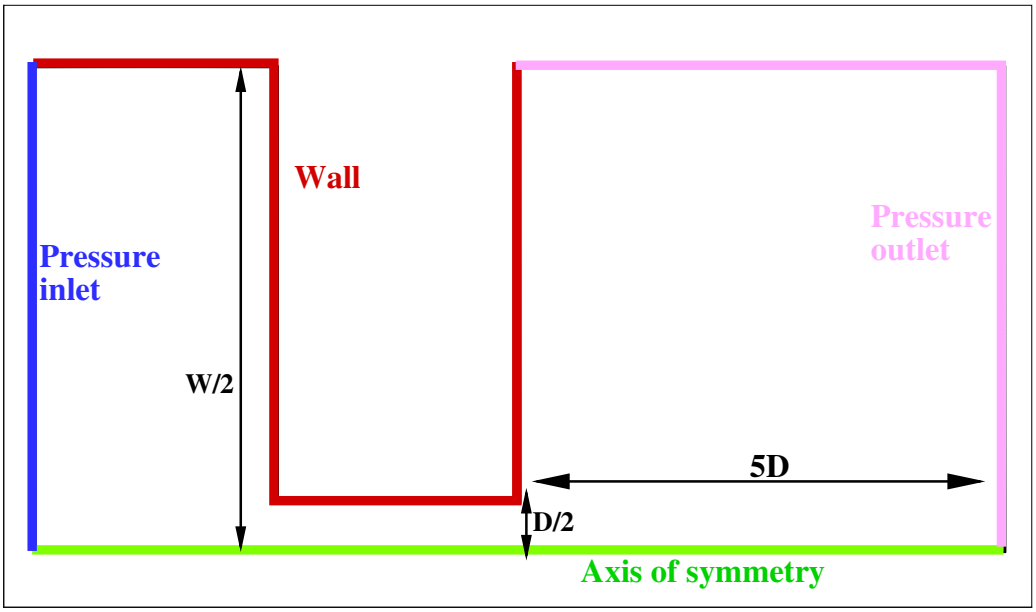

Figure 4.1: Computational domain and boundary conditions used for simulations.

Ratio (NPR) = 20.0;
Total temperature (T_0) = 300K;
The flowing gas is air ($R = 287J/kg.K$, $\gamma = 1.4$).
This pressure ratio corresponds to extremely underexpanded jet, a case in which the jet contains one normal shock (Mach disk) at the end of the single shock cell.

4.3 Nozzle geometries

The effect of upstream geometrical configurations is addressed numerically using the in-house CFD solver mentioned in Section 2.3. All of the simulations are inviscid to single out the influence of geometry regardless of the viscous effects. Different nozzle shapes are tested, viz., straight nozzle, conical converging nozzle, diverging orifice, and round nozzle with different radii. The nozzle geometries are tabulated in Table 4.1.

Table 4.1: Geometrical configurations of the used nozzles.

Nozzle	Geometry configurations
a	Settling chamber width = 4.0 D, conical converging nozzle of angle 30°.
b	Settling chamber width = 4.0 D, conical converging nozzle of angle 50°.
c	Settling chamber width = 5.0 D, straight nozzle of length 2.5 D.
d	Settling chamber width = 10.0 D, straight nozzle of length 2.5 D.
e	Settling chamber width = 5.0 D, straight nozzle of length 1.25 D.
f	Settling chamber width = 10.0 D, conical converging nozzle of angle 30°.
g	Round nozzle, $R = D$.
h	Round nozzle, $R = 2.5\ D$.
i	Diverging orifice of angle 15°.

4.4 Mach Disk Location

Initial interest is directed towards the location of Mach disk within the jet. The apparition of this shock wave corresponds to a condition of highly underexpanded jet, where an oblique shock cannot bring the flow up to the ambient pressure. Hence, the regular reflection turns into Mach reflection, and Mach disk forms at the end of shock cell as a normal shock. Figure. 4.2 shows Mach number contours for the chosen geometries. A vertical line is drawn at the location of Mach disk in case of conical nozzle with settling chamber width of 4D (Fig. 4.2 (a)), as a reference line.

One can notice from Fig. 4.2 that Mach disk location is merely sensitive to the nozzle geometry when the flow is expanding gradually. However, the expansion trend in the straight nozzle affects the Mach disk location significantly due to the shock train generated within the duct. This effect leads to shifting the Mach disk upstream, as shown in Fig. 4.2 (c), 4.2 (d), and 4.2 (e). It is also noticeable that the length of the straight nozzle does not remarkably affect the jet structure.

Nevertheless, the width of the settling chamber appears to shift Mach disk further upstream due to the intensity of shock waves experienced in the duct. Moreover, it is noted that Mach disk crosses the reference line slightly in the case of round nozzles, (g) and (h), and diverging orifice (i). That could be attributed to the smooth expansion of the gas in the case of the round nozzles, which can be considered isentropic, and the free expansion in the case of the diverging orifice.

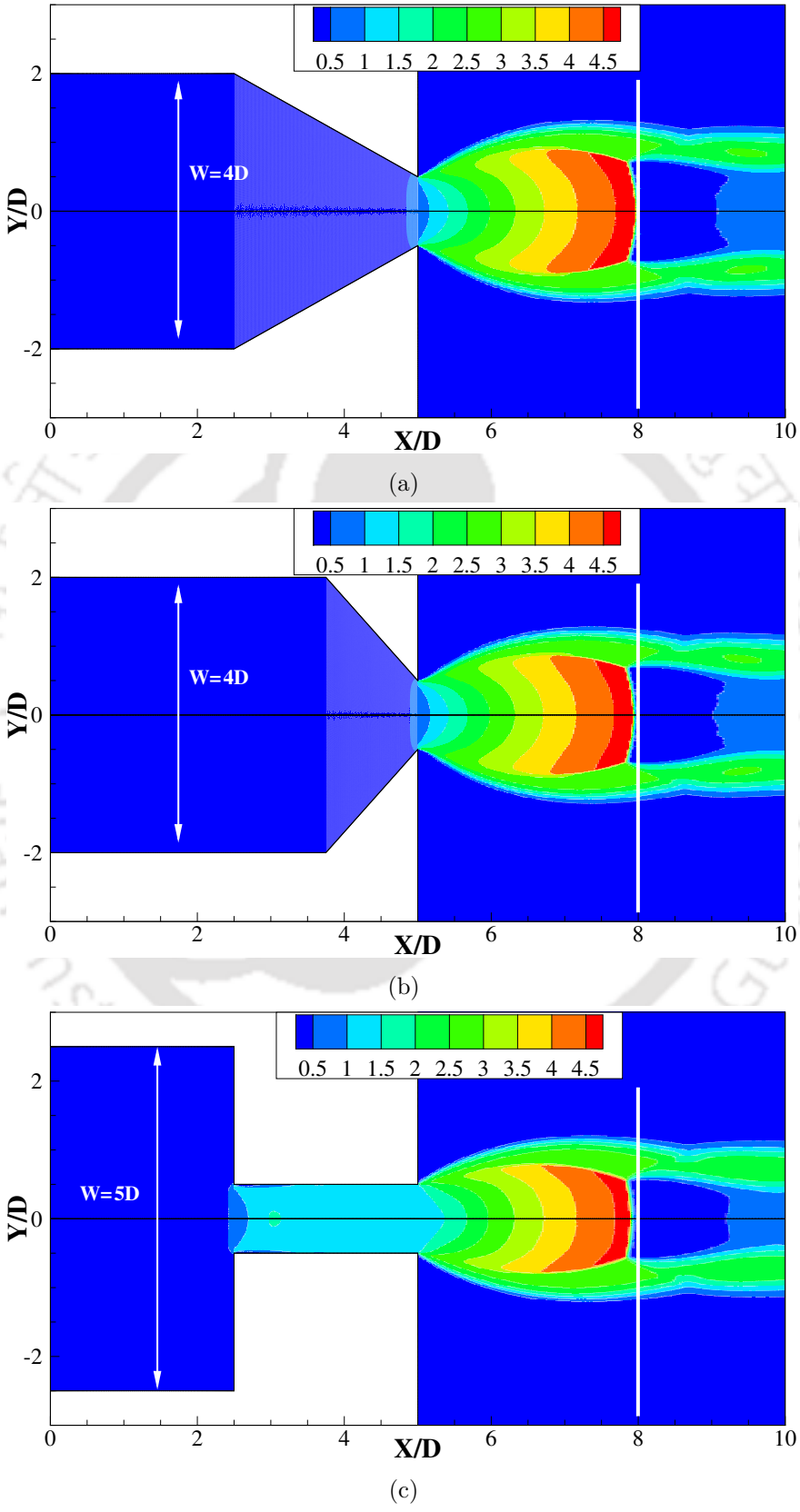

Figure 4.2: Mach number contours for the used nozzles.

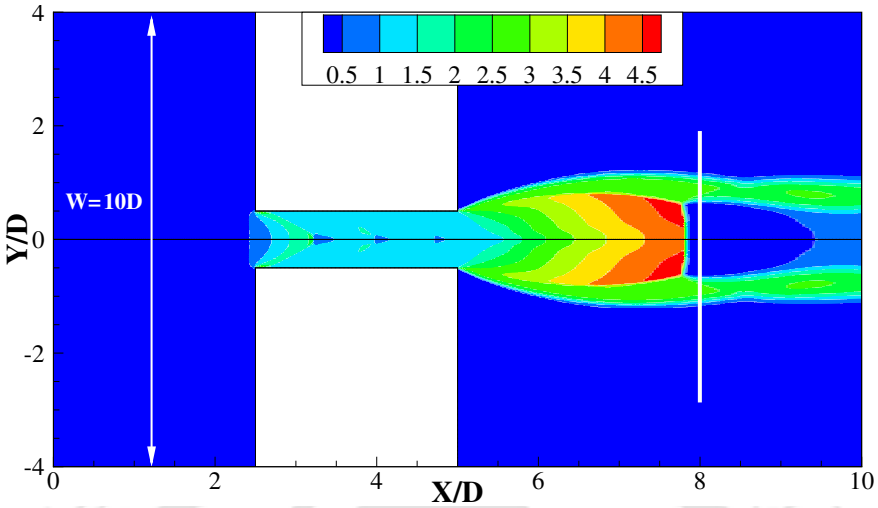

(d)

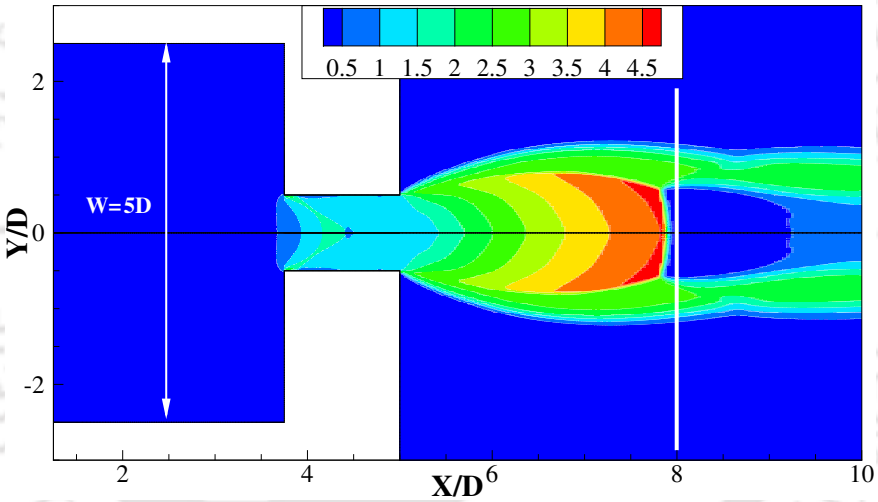

(e)

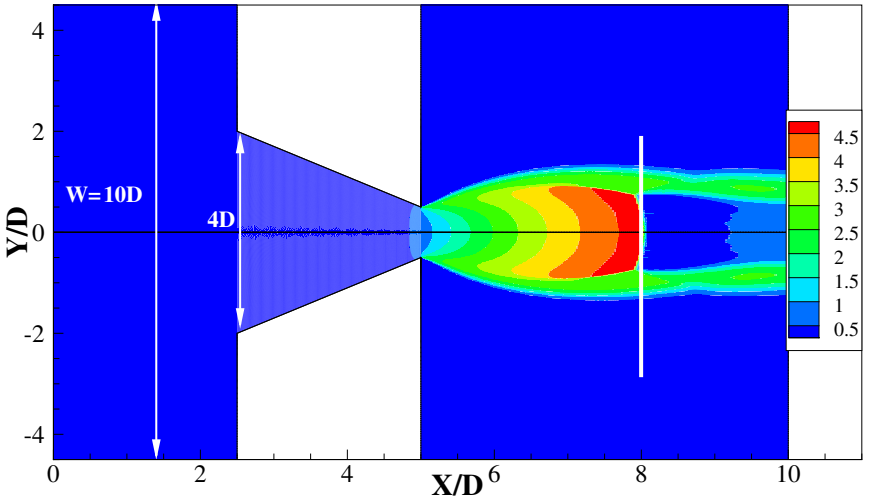

(f)

Figure 4.2: Mach number contours for the used nozzles.

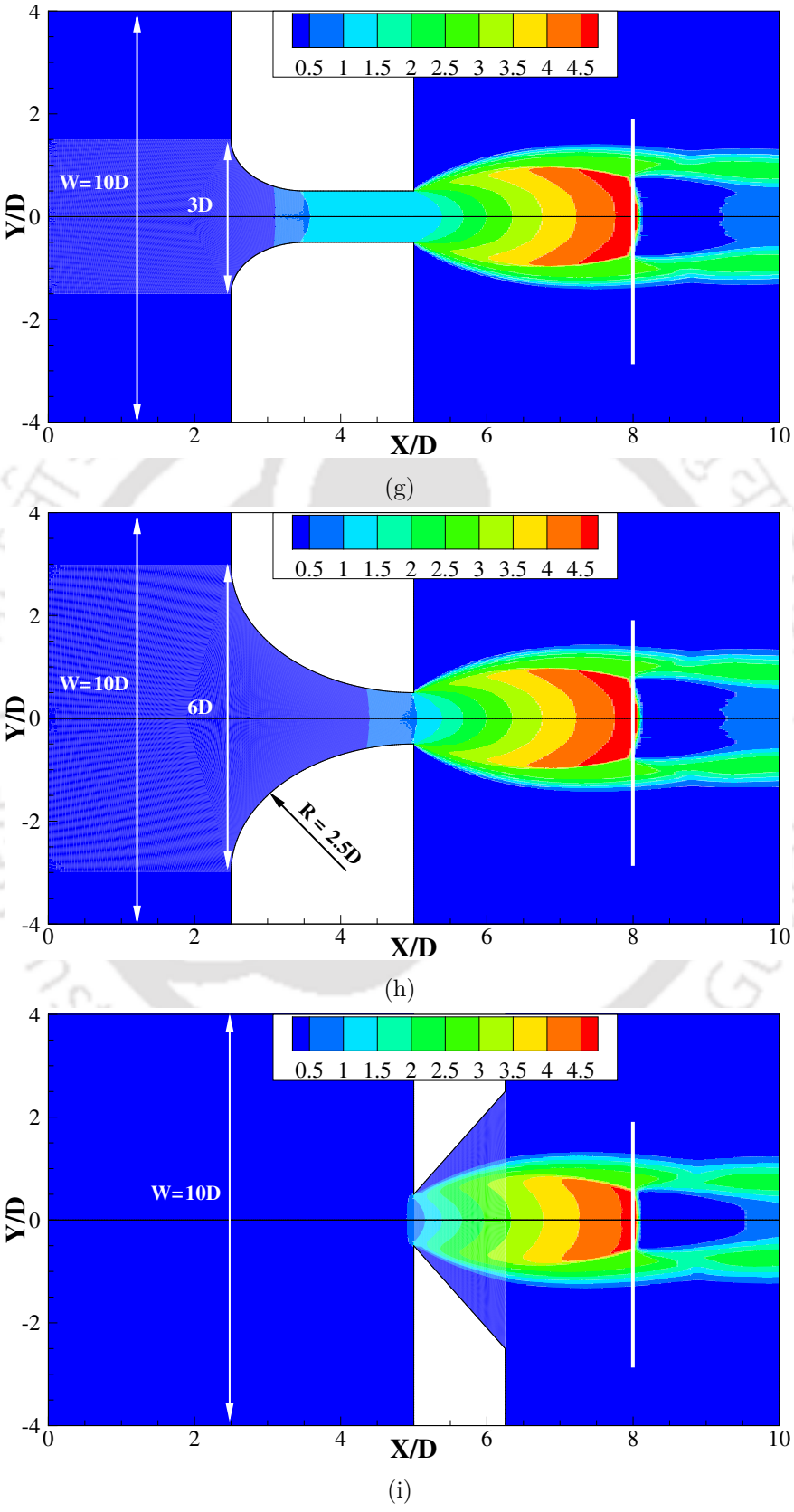

Figure 4.2: Mach number contours for the used nozzles.

To get a clear look at the location of Mach disk, axial pressure distribution for all the nozzles is plotted in Fig. 4.3 after normalising it with the back pressure. The location of Mach disk is the abrupt jump in the jet pressure ratio after leaving the nozzle exit plane.

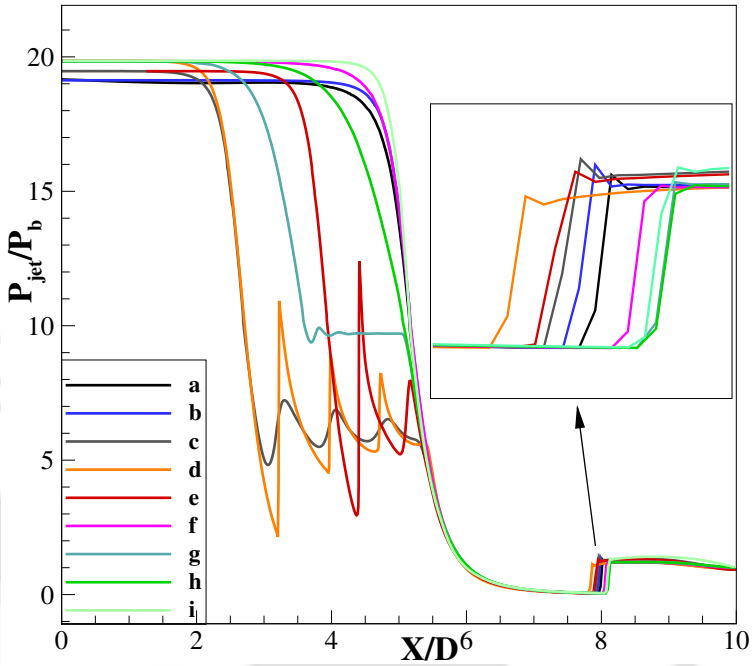

Figure 4.3: Axial distribution of the jet pressure ratio for the used nozzles.

Figure 4.3 depicts the axial pressure distribution from the settling chamber to a few diameters downstream of the nozzle exit. As stated earlier, nozzle (d) causes the normal shock to apprear at an upstream location compared to the other nozzles. Then nozzles (e) and (c) that have the same shock train configuration but with less intensity. The group of straight nozzles is followed by the group of conical nozzles (a), (b), and (f), and finally, the round nozzles and sharp-edged orifice. This result, along with jet height, can be used to compare the potential loss in each nozzle, and it conforms with the existence and intensity of shock waves within the nozzle.

To shed the light on the expansion trend within the straight nozzle, numerical schlieren images for the straight nozzle (d) and round nozzle (h) are plotted in Fig. 4.4. Here, nozzle (h) is considered as the contoured nozzle through which the flow expands isentropically, which makes it a proper frame of reference.

It is clear from Fig. 4.4 that the flow experiences a series of oblique shock waves within the straight nozzle, known as shock train, which causes the expansion process to deviate from isentropic and decreases the potential of the flow. This effect ultimately reduces the flow energy and pressure at the nozzle exit plane. Hence, the jet becomes less underexpanded, Mach disk moves upstream, and the total jet height decreases. On the other hand, in the round nozzle, the intensity of schlieren seems to be moderate within the nozzle, and it in-

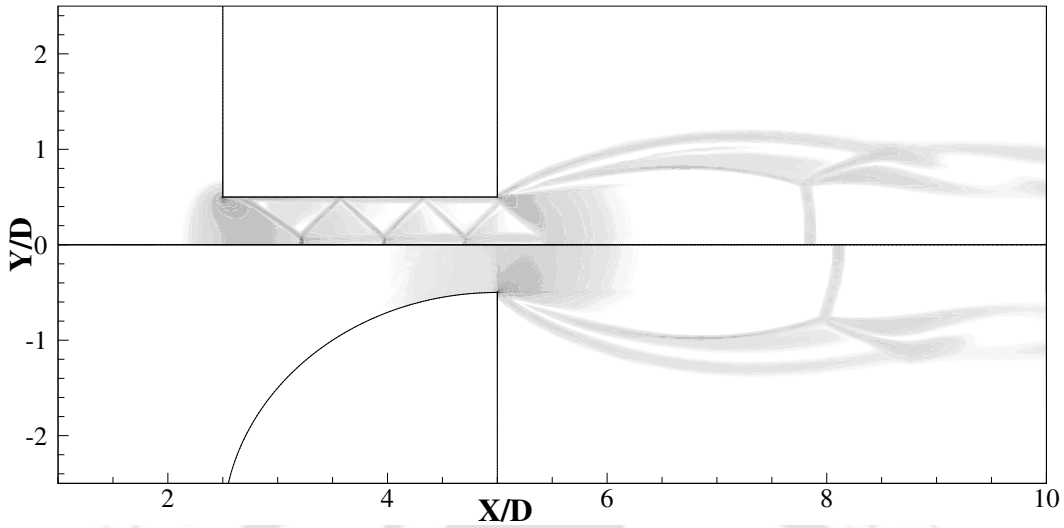

Figure 4.4: Numerical schlieren images for round nozzle (h, lower) and straight nozzle (d, upper).

creases near the nozzle exit plane, which indicates a smooth expansion throughout the nozzle.

4.5 Mach Disk Height

Equations 1.3 and 1.4 discriminate between sharp-edged nozzle and contoured nozzle. Therefore, it becomes crucial to address the changes that occur upon Mach disk diameter for different types of sonic nozzles. For this purpose, the height of Mach disk for each nozzle is measured and non-dimensionalised with the nozzle diameter. The results are plotted in Fig. 4.5.

One can arrive at clear conclusions from the data plotted in Fig. 4.5. It is evident that the highest Mach disk is obtained for contoured nozzles (g) and (h), as they maintain the minimum pressure loss during expansion. For the same reason, these two nozzles achieve the maximum Mack disk location as well.
The minimum height is noticed for orifice (i), which should come to no surprise because of the vena contracta observed at the sharp-edged nozzle. The fluid contraction (vena contracta) causes the flow to incline toward the jet axis for a small distance after leaving the nozzle to a point lower than nozzle edge, and hence decreasing the jet height in general. A close-up view is illustrated in Fig. 4.6 showing how the streamlines approach towards the axis even after leaving the nozzle exit. A horizontal reference line is drawn from the nozzle lip.

Comparing Mach disk diameter for conical nozzles (a), (b), and (f) shows no impact for the width of settling chamber, however, increasing the angle of convergence seems to decrease Mach disk diameter. It is worth mentioning that, although nozzle (i) has the most extended

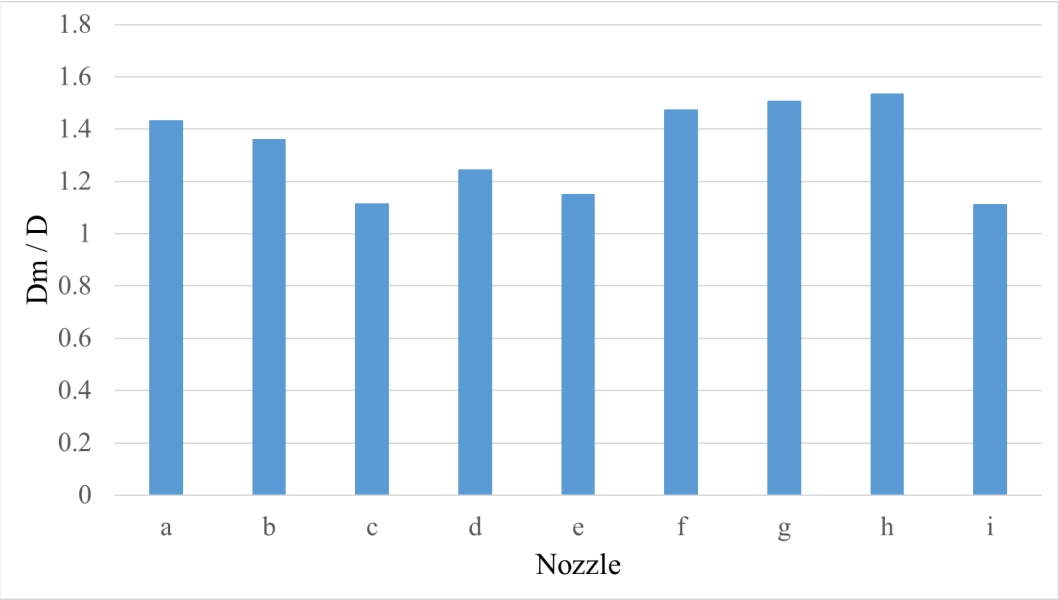

Figure 4.5: Mach disk diameter for the used nozzles.

expansion area in axial direction, it has the least Mach disk diameter, and henceforth it has the least expansion area in the direction normal to jet axis.

4.6 Sonic Line

The path of expansion process determines the location and curvature of the sonic line. Therefore, the sonic line in all of the nine cases is plotted in Fig. 4.7.

One can infer from Fig. 4.7 that sonic line exists at the end of converging part in all the nozzles, viz, at the minimum area or at the throat. For example, in round nozzle (g), the sonic line is located at the intersection between the converging part and the straight duct, where the flow achieves the sonic speed or Mach number is equal to 1.0. Whereas in nozzle (h), the converging part is extended up to the nozzle exit plane, and hence the sonic line is located at the nozzle exit. Nevertheless, in the case of straight nozzle (c, d, e), the air does not accelerate within the duct, and hence it obtains the sonic conditions at the beginning of the nozzle.

Moreover, it is seen that the curvature of the sonic line varies with the nozzle configurations. It is evident that it has less curvature when the convergence is smooth, and vice versa. Looking at nozzle (h), it has the smoothest expansion among the nozzles, thus its sonic line tends to look like a straight line. However, the sonic line has maximum curvature in case of straight nozzles, such as (c), (d), and (e), because of the sudden duct contraction. It is to be noted that sonic line in nozzle (i) has a stem near the nozzle lip, and this can be related to the vena contracta at the sharp-edged nozzle as the flow deflects away from the lip.

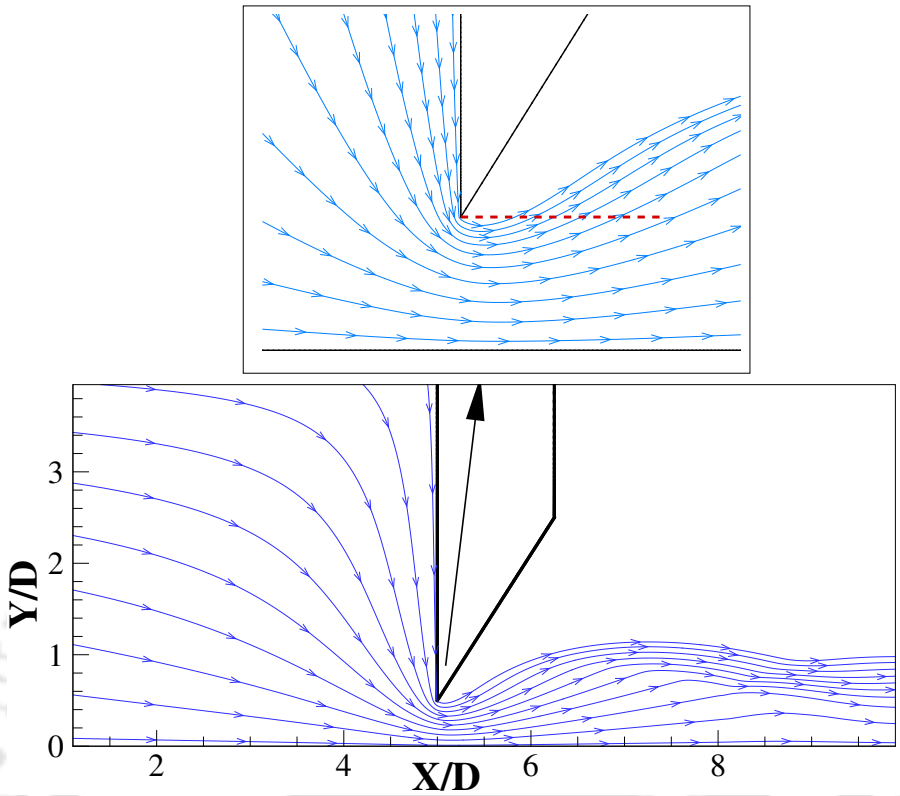

Figure 4.6: A close-up look on the phenomenon of vena contracta in the nozzle (i).

Even though the sonic line is sensitive to geometrical configuration of the nozzle, it is not affected by the nozzle pressure ratio. Figure 4.8 illustrates the sonic line in case of nozzle (i) for different pressure ratios, 12.0 and 20.0.

It can be seen in Fig. 4.8 that the curvature and location of sonic line are not affected by the pressure ratio, which assures that sonic line is fully dependent on the upstream geometry of the nozzle. However, it can be noted that the stem of sonic line is smaller in case of low pressure ratio, and that is attributed to the decrease of intensity in vena contracta phenomenon as the pressure ratio decreases.

4.7 Conclusions

This chapter has been dedicated to studying the element of sonic jet (Mach disk and sonic line) for different nozzle geometries in case of underexpanded jet with a nozzle pressure ration (NPR) of 20.0. The investigation is performed numerically using the in-house CFD solver for inviscid flow. The following findings are concluded:
1) Mach disk location is slightly sensitive to the nozzle geometry. It depends on the flow potential loss within the nozzle, the smoother the expansion, the further Mach disk moves

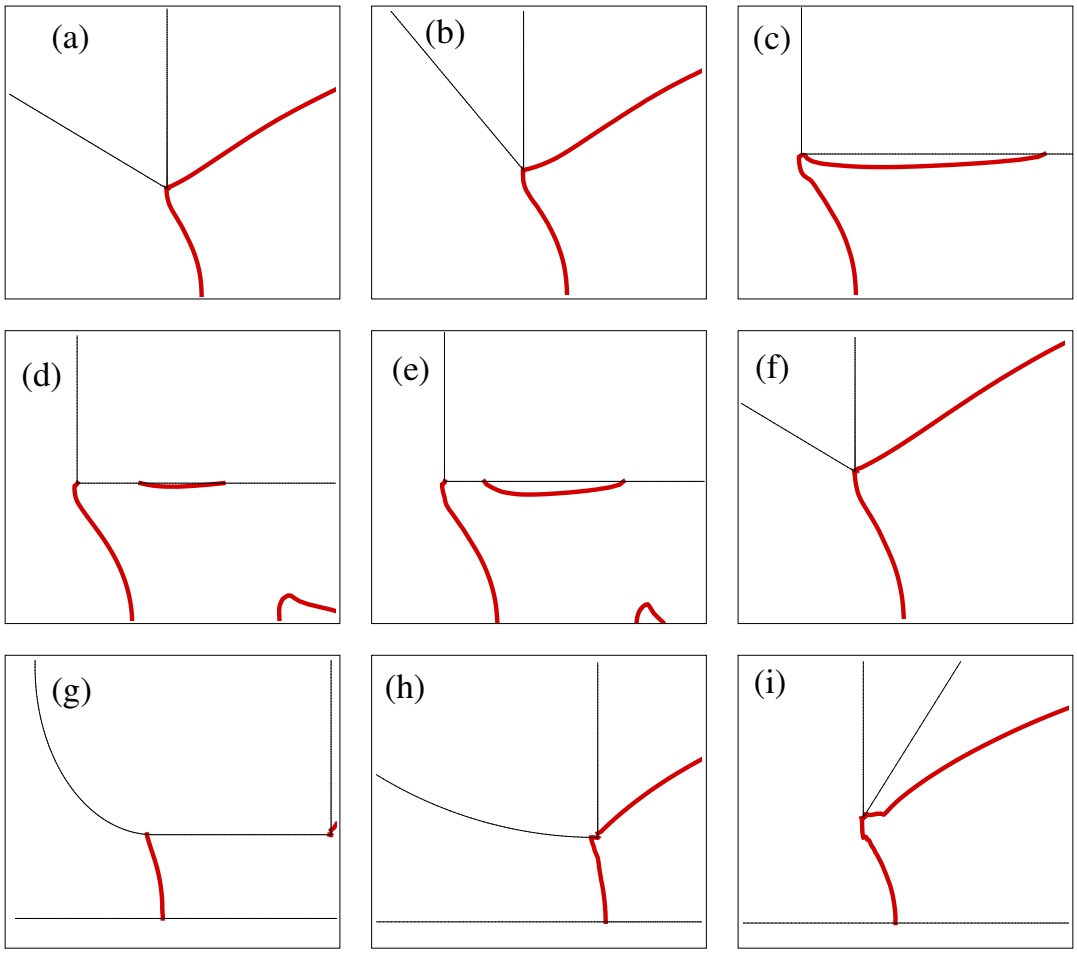

Figure 4.7: The sonic line in all the cases.

downstream. However, when the jet experiences shock waves within the nozzle, it loses a certain amount of potential which causes compressible flow region to decrease.

2) Mach disk height is affected by the nozzle shape. Contoured nozzles produce the highest Mach disk, whereas diverging orifice produces the minimum-height Mach disk.

3) The sonic line characteristics are influenced by the nozzle geometry. The sonic line is noted to take place at the end of converging area. Further, the smoothly converged nozzle causes the sonic line to be almost straight. Nevertheless, the straight nozzles with sudden contraction causes the curvature of sonic line to increase.

4) The location and curvature of the sonic line is not affected by the pressure ratio.

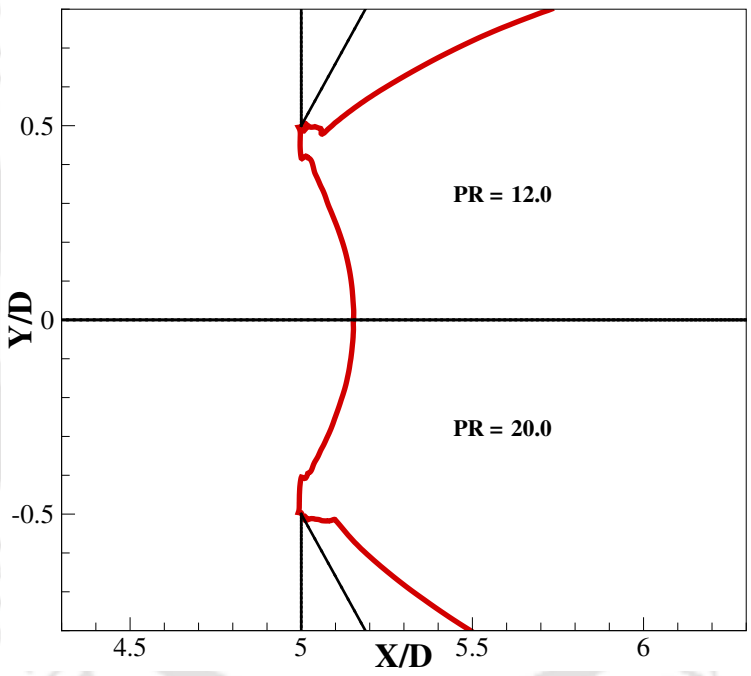

Figure 4.8: The sonic line in case of sharp-edged orifice (i) for $PR = 12.0$ (upper) and $PR = 20.0$ (lower).

CHAPTER 5

SUPERSONIC NOZZLE SHAPE OPTIMISATION

Abstract

Creating a supersonic jet in the laboratory is both challenging and expensive task. The supersonic flow is sensitive to the shape of the wall bounding it as a shock could be developed at the sharp edges and steep walls. Moreover, the growth of boundary layer, within and outside the nozzle, makes the design of a convergent-divergent nozzle a sophisticated work. The present work proposes an optimisation algorithm which is believed to be efficient in constructing a nozzle contour to deliver a shock-free radially-uniform flow at the exit plane. The resulting nozzle shapes are used to perform a number of simulations to understand the effect of each factor in the nozzle design. A comparison is carried out between the currently-obtained nozzle shape and an existing nozzle in the literature. The optimised nozzle shows a potential core of 7 throat diameters height at the nozzle exit and an axial extent of 28 throat diameters downstream the exit plane. Moreover, the shear layer growth is examined and linked to the boundary layer and nozzle wall shape. Further, the nozzle appears to operate efficiently even after increasing the nominal total temperature by 25% or decreasing it by 50%.

5.1 Introduction

Engineers have struggled to achieve successful instruments that produces high-speed flows with customisable flow properties. It is a fact that every application requires different flow structure to satisfy the purpose of that application. It is only fare to say that property of uniformity is the most desirable amongst many applications; a uniform flow corresponds to the maximum thrust in a rocket nozzle [119], and the radially-uniform profile for the maximum distance allows to conduct physical [56] and chemical [57] experiments. Hence, many works in the literature [43, 69, 72, 73] have been directed towards designing such nozzle. This chapter proposes three different optimisation processes to obtain a nozzle wall shape that

produces a radially-uniform flow. The steepest descent optimisation technique (explained in Section 2.2) is employed to obtain the shape with minimum radial velocity at the outlet, along with restriction on the inlet angle, i.e., the angle of divergence immediately downstream the throat. The optimisation technique is coupled with a flow solver based on one-dimensional flow relations, elaborated in Section 2.1 to eliminate the need for expensive computations. Three different ways of implementing the constraints are discussed and compared with the experimental results after fabricating the nozzle. Section 5.2 describes the processes that are used to construct the three nozzles, Section 5.3 highlights the role that initial angle of divergence in a supersonic nozzle plays in the process of gas expansion, Section 5.4 shows the influence of viscosity on the flow field within and downstream the nozzle, Section 5.5 points out the differences in performance for the three suggested nozzles, Section 5.6 highlights the development of shear layer in the proposed nozzle designs, Section 5.7 shows how the optimum nozzle performs under off-design conditions, Section 5.8 compares this nozzle's performance with a previously-designed nozzle [79], and finally, Section 5.9 summarises the results of current investigation.

5.2 Nozzle design process

Three different nozzles are suggested herein according to the method used in generating shape of the nozzle wall. The optimisation process starts from the right conical nozzle shape as the initial standard for all the cases. Each optimisation process follows different convergence path to minimise the objective function. These design specifications and restriction values are tabulated in Table 5.1. The convergence criteria of the said processes is plotted in Fig. 5.1.

Table 5.1: Specifications of the used nozzles.

Nozzle	α value	Initial angle	Bézier curve
1	0.0001	$=< 15°$	Third order
2	1D search	not restricted	Fourth order
3	1D search	$=< 10°$	Fourth order

The nozzle design is for the total temperature of 1300 K, total pressure ratio of $P_0/P_e = 2200$ and argon as the flowing medium. The geometric constraints are 2.0 mm as the throat diameter, exit diameter of 24 mm, and nozzle length of 30 mm. The process having a fixed value of α (as in $N1$) takes more iterations to arrive at the desired nozzle shape as compared to the other method which accounts 1-D search method to determine the optimal shape (as in $N2$ and $N3$).

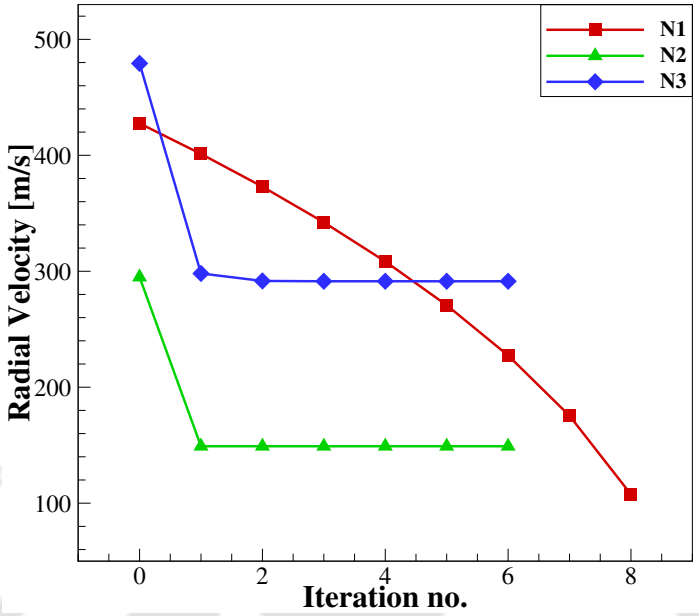

Figure 5.1: The convergence criteria for three different optimisation technique.

5.3 The significance of initial angle of divergence

The nozzle design is often governed by geometrical constraints (the length and diameter of the nozzle), gas dynamic restriction, like the minimum vacuum pressure that could be obtained by certain vacuum pump, or the reservoir temperature and pressure of the gas. Hence, it is important for the optimisation process to overcome these restrictions. A short nozzle, comparing to its diameters, would have a large divergence angle when constructed as a conical nozzle. Here comes the importance of imposing a limit for this angle.

Initially, inviscid simulations are performed on the three nozzle designs, $N1$, $N2$ and $N3$. Figure 5.2 shows the numerical schlieren images for $N2$ and $N3$ with identical boundary conditions, $T_0 = 1300\ K$ and $P_0/P_e = 2200$. It is evident that setting the initial angle constraint of 10 degrees limits the ability of gas to expand throughout the nozzle. On the other hand, the nozzle designed without restriction ($N2$) allows the gas to expand freely from the beginning of the divergent section. This is clear from Fig 5.2 where the expansion waves start coalescing immediately downstream of the throat area, creating high density gradient which is easily captured by schlieren image. Moreover, more the jet expands, the earlier it attains a low pressure value which would eventually require a normal shock to achieve equilibrium between the jet pressure and the ambient pressure [41]. This is illustrated in Fig 5.2 as the jet from the nozzle designed without initial angle constraint forms a Mach disk in an earlier location downstream of the nozzle exit. Nevertheless, when the initial divergence angle condition is imposed, the jet expands gradually within the nozzle, keeping relatively high pressure which can be further expanded after the jet leaves the nozzle.

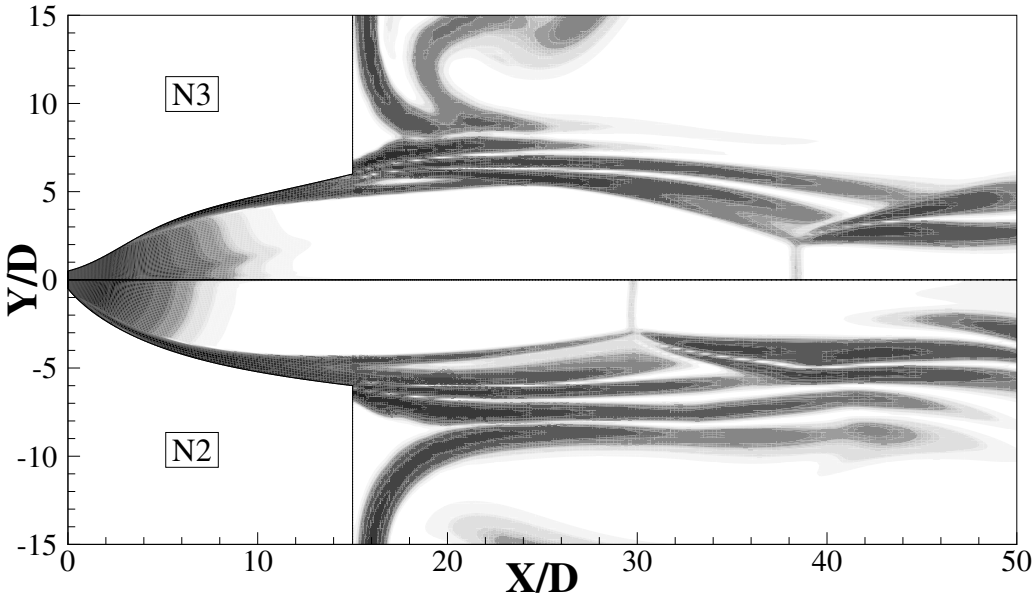

Figure 5.2: Numerical schlieren images for the nozzles $N2$ and $N3$.

5.4 The influence of viscosity

The optimisation procedure basically deals with the area-Mach number gas dynamic relation, which neglects the viscosity of the fluid. Therefore, to ensure the applicability of the current process for the viscous flows, the boundary layer thickness has to be accounted. Therefore, simulations are performed to arrive at an optimum configuration with the same constraints and conditions mentioned earlier. Nozzle ($N1$) is designed as per the low-fidelity solver for zero radial velocity at the exit. Two simulations are performed on this nozzle with inviscid and viscous wall boundary conditions. The influence of boundary layer on the flow field is significant for high-speed flows, this influence is shown as schlieren images in Fig. 5.3. The inviscid simulation aligns well with the desired flow field, whereas the viscous flow field develops a boundary layer at the wall which disturbs the flow and decreases the potential core area.

The flow field is significantly altered by imposing the viscous effects, especially the displacement thickness, δ^*, of the boundary layer, hence, there is necessity to compensate for this thickness. The low-fidelity inviscid solver is then set to converge when the objective function, $V_{rad,ex}$, attains a predefined value of radial velocity in comparison with the total jet velocity at the exit. The tolerance value depends on the gas and flow properties as well as geometric constraints. Hence, it needs to be evaluated for each case, such tolerance would eventually be balanced by the boundary layer thickness. For the present nozzle designs, this tolerance is considered 10% for exit radial velocity.

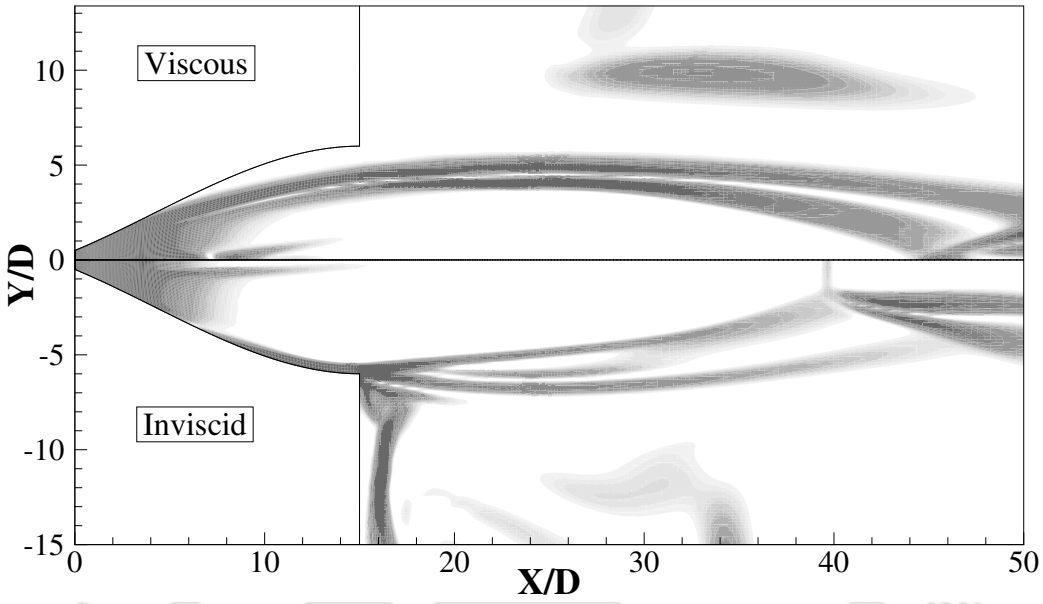

Figure 5.3: Numerical schlieren for the inviscid (lower) and viscous (upper) flow fields of the nozzle $N1$.

5.5 Performance analysis

The aforementioned three nozzles, $N1$, $N2$ and $N3$, designed with the aforementioned constraints and conditions, are compared with the conical nozzle by the means of Mach contours to reinforce the importance of nozzle wall shape on the near-field area, which is shown in Fig. 5.4. The shape depicts the length of potential core for each nozzle where the conical nozzle shows an extent up to 30 throat diameters downstream of the nozzle exit plane and the nozzles $N1$, $N2$ and $N3$ show a length of 28, 10, 25 throat diameters, respectively. It is clear that $N2$ produces the shortest potential core downstream of the nozzle exit plane, that is due to the free expansion immediately downstream of the nozzle throat, whereas it is initially restricted from expansion in $N1$ and $N3$. Hence, the other two nozzles keep relatively high pressure at the nozzle exit plane, and it continues to expand after exiting the nozzle. The properties of the jet, at the nozzle exit plane and a few diameters downstream, determine the dimensions of the potential core and the usability of the nozzle design for certain application, such as absorption spectroscopy. Hence, the radial and axial velocity throughout the cross-sectional nozzle exit area, are normalised with the total velocity at the axis and plotted in Fig. 5.5 to examine the flow field and the uniformity of the jet when it exits each of the nozzles. It can be observed from Fig. 5.5 that velocity profiles for all the nozzles follow the same behaviour, axially and radially. Here, nozzle $N2$ profile shows higher values of radial velocity than the conical nozzle and $N1$, and less diameter of uniform flow region than nozzles $N1$ and $N3$, which implies higher boundary layer thickness. That is evident from the previous discussion in section 5.3, as the uncontrolled initial angle allows the jet to expand freely and form a thicker boundary layer. The conical design of the nozzle shows the

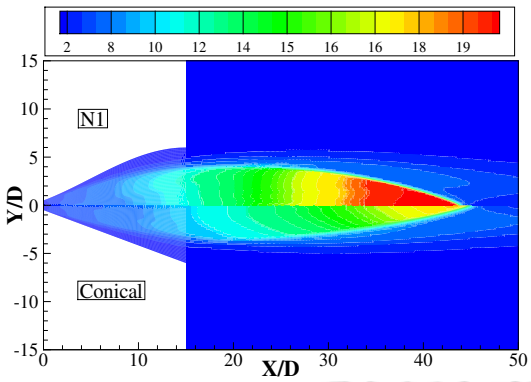

(a) Conical nozzle vs. N1.

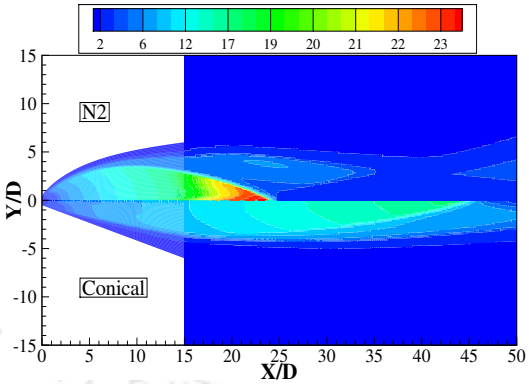

(b) Conical nozzle vs. N2.

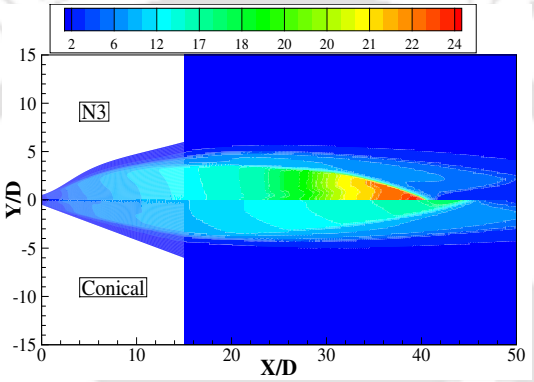

(c) Conical nozzle vs. N3.

Figure 5.4: Mach contour comparison for the proposed nozzle designs.

least radial velocity value, nevertheless, the nozzle $N1$ which is used in the experiment has the maximum uniformity height, at the nozzle exit plane. It may be observed from Fig. 5.5 and 5.6 that the radial velocity becomes negative for a short interval of the radial distance. This observation implies that the flow is moving towards the axis, and this is possible when the incident shock is strong enough to force the flow inwards. In this case, nozzle $N2$ has no restriction on the initial angle, so, the expansion is free and stronger than it in the other nozzles. Hence, the resulting incident shock is expected to be stronger as well. Further, the disturbance in axial velocity profile implies the end of potential core and the start of the shear layer. It can also be deduced from Fig. 5.5 and 5.6 that the conical nozzle produces a lower radial velocity value compared to other nozzles. However, in the sense of potential core height, the disturbance in radial velocity profile seems to take place at a lower location (almost 2 Y/D), whereas nozzle $N1$ extends the potential core up to (3.5 Y/D) which is a desired jet property.

Moreover, the jet forms its own boundaries after leaving the physical boundaries of the nozzle, and continues to expand throughout. The distance for which the jet maintains a uniform profile is called the length of potential core, and it is of high significance for some applications. Therefore, it becomes important to investigate the jet profile a few diameters downstream of the nozzle exit. Figure 5.6 illustrates the normalised radial (v^*) and axial (u^*) velocity

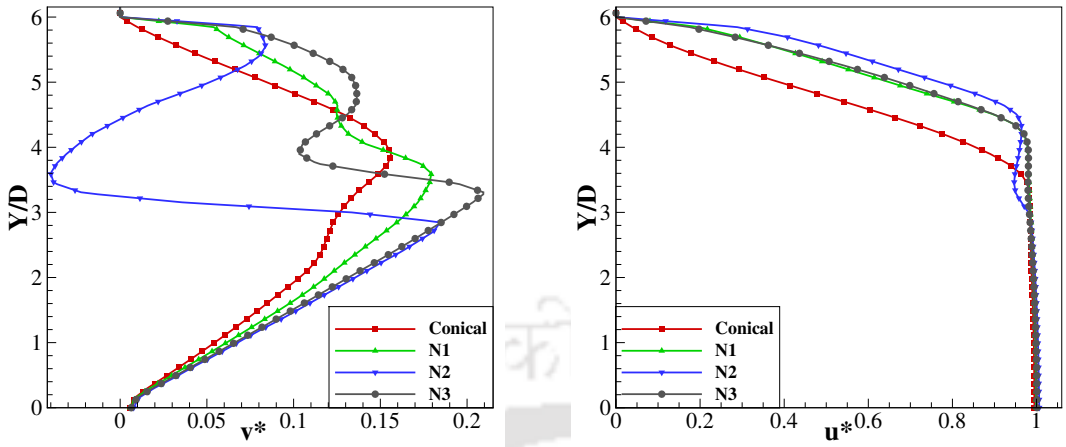

(a) Radial velocity. (b) Axial velocity.

Figure 5.5: Velocity profile at the nozzle exit plane for different nozzle designs.

profiles at 10 throat diameters downstream of the nozzle exit plane. It is evident from the

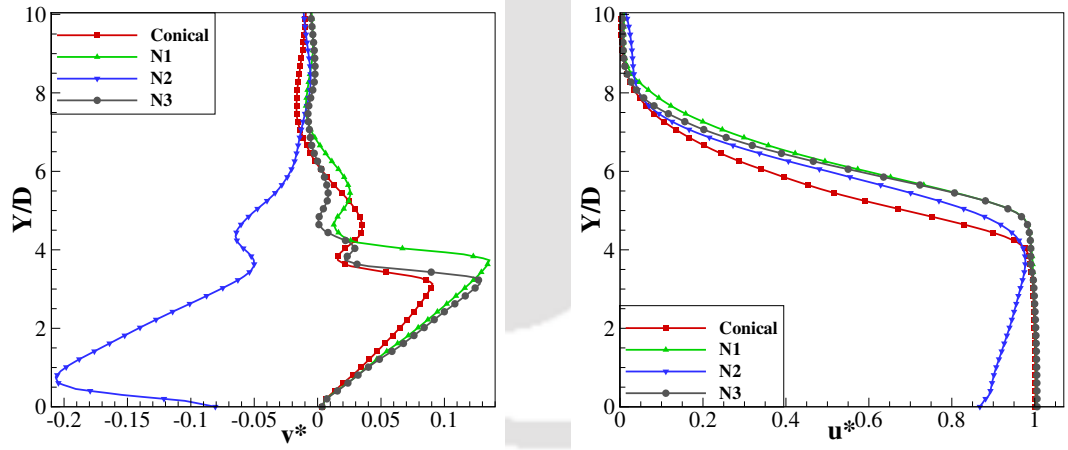

(a) Radial velocity. (b) Axial velocity.

Figure 5.6: Velocity profile 10 throat diameters downstream of the nozzle exit plane for different nozzle designs.

axial velocity profile in Fig. 5.6 that nozzles $N1$ and $N3$ follow the same trend. However, the radial velocity profile indicates an advantage of higher potential core for nozzle $N1$. The normalised radial velocity profile of nozzle $N2$ seems to be disturbed and in the negative side of the axis. That is because the axial location, 10 throat diameters downstream, falls after the axial reflection point, that appears in Fig. 5.4 (b). Thus, nozzle $N2$ has the shortest potential core compared to the other nozzle designs, for the current experimental boundary conditions.

5.6 Shear layer development

The transverse profiles of flow properties, for the above-discussed three optimised nozzles and the right conical nozzle, are extracted at the nozzle exit plane in addition to four different axial locations, viz., 5 mm, 10 mm, 15 mm, and 20 mm downstream of the nozzle exit plane. These locations correspond to 2.5D, 5D, 7.5D, and 10D downstream of the nozzle exit, respectively.

To visualise the thickness of the inviscid core and shear layer at these locations, density and axial velocity profiles for the conical nozzle, $N1$, $N2$ and $N3$ are plotted in Fig. 5.7 and 5.8, respectively. The radial coordinate (Y) is normalised to the nozzle throat diameter. For comparison, in Fig. 5.7, a dashed line of reference is drawn at a radial location where the inviscid core of conical nozzle ends at an axial location of 20 mm. One can notice that the inviscid core of nozzle $N1$ extends farther above the line, indicating more radial extent for the locations downstream of nozzle exit, whereas the flow seems less uniform at the nozzle exit.

Moreover, the flow emitting from nozzle $N2$ attains a uniform profile at the nozzle exit and then shear layer starts to take over the inviscid area. At a location of 20 mm downstream the nozzle exit, the flow loses its uniformity, and it appears that inviscid core has been terminated at a location between 15 mm and 20 mm downstream the nozzle exit. Looking at the radial profile of nozzle $N3$ jet, the flow behaves uniformly across the axial and radial directions and the uniform area extends farther above the reference line. However, it is noticed that nozzle $N1$ produces higher inviscid core than the other nozzles.

Further, the plots show that shear layer of nozzle $N1$ is comparable in thickness with that of conical nozzle, whereas nozzles $N2$ and $N3$ show higher thickness in shear layer. The density in all the nozzles decreases in the downstream direction and it obtains the minimum at a location of 20 mm downstream. However, the same axial location in nozzle $N2$ shows higher density, which implies a compression wave upstream of this location, i.e., between 15 mm and 20 mm downstream.

To investigate the flow field further, Fig. 5.9 illustrates isodensity lines for the four nozzles. In this figure, one can discriminate the incident shock (barrel shock) and shear layer (resulting from boundary layer within the nozzle). It is found that there is a weak disturbance within the conical nozzle and nozzle $N1$, which propagates up to the nozzle exit and then diffuses downstream. This disturbance justifies the distorted radial profile at the exit of these two nozzles (Fig. 5.7 (a) and 5.7 (b)). Moreover, Nozzles $N1$ and the conical nozzle show similar axial extent of the inviscid core, but $N1$ shows more radial extent. On the other hand, nozzles $N2$ and $N3$ do not show similar trend, and hence the uniform profile at the exit.

Furthermore, the unrestricted divergence downstream the throat of nozzle $N2$ allows the jet to expand freely and rapidly within the nozzle, which causes the jet pressure to drop drastically and decreases the degree of underexpansion, and therefore terminates the inviscid

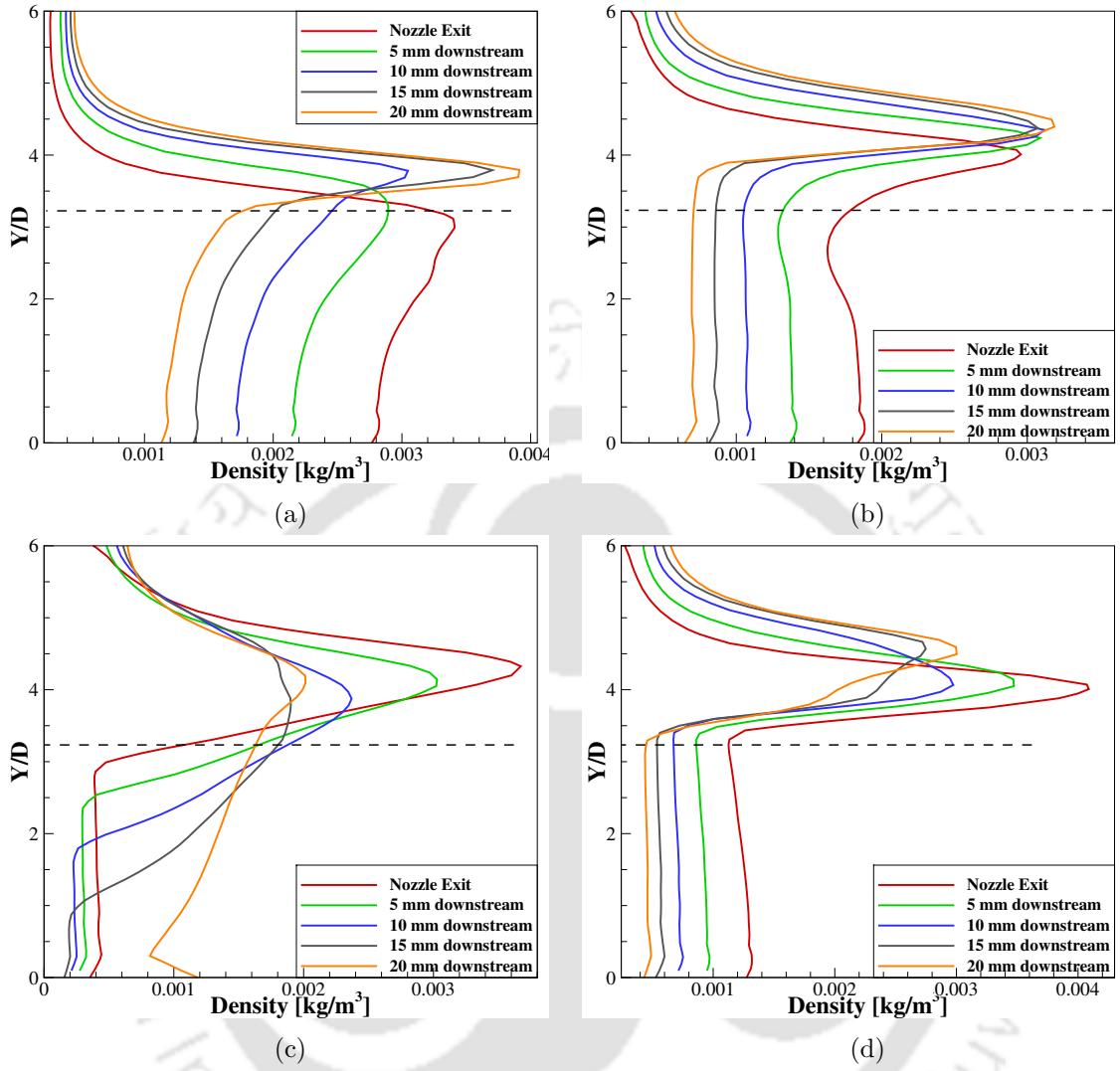

Figure 5.7: Radial density profiles at the exit and four axial locations downstream the exit of a) conical nozzle, b) $N1$, c) $N2$, and d) $N3$.

core at an earlier axial location. Also, from the isodensity lines of nozzles $N2$ and $N3$, there seems to be larger gap between the barrel shock and shear layer than the cases of the conical nozzle and nozzle $N1$. This effect explains the observed thickness of shear layer in Fig. 5.7 (c) and 5.7 (d).

To take a closer look at how the flow is propagating, the axial pressure distribution within the four nozzles and in the near-field area is plotted in Fig. 6.6. In this figure, the axial distance is normalised to the throat diameter, and the jet pressure is normalised to the back pressure.

It is clear from Fig. 5.10 that jet expansion is terminated at an earlier location (22 X/D) in the case of nozzle $N2$ due to the free expansion. The inviscid core is extended up to 40 X/D, 44 X/D, and 46 X/D for nozzles $N3$, $N1$, and the conical nozzle. It is further seen that the conical nozzle forms stronger internal shock immediately downstream the throat, whereas

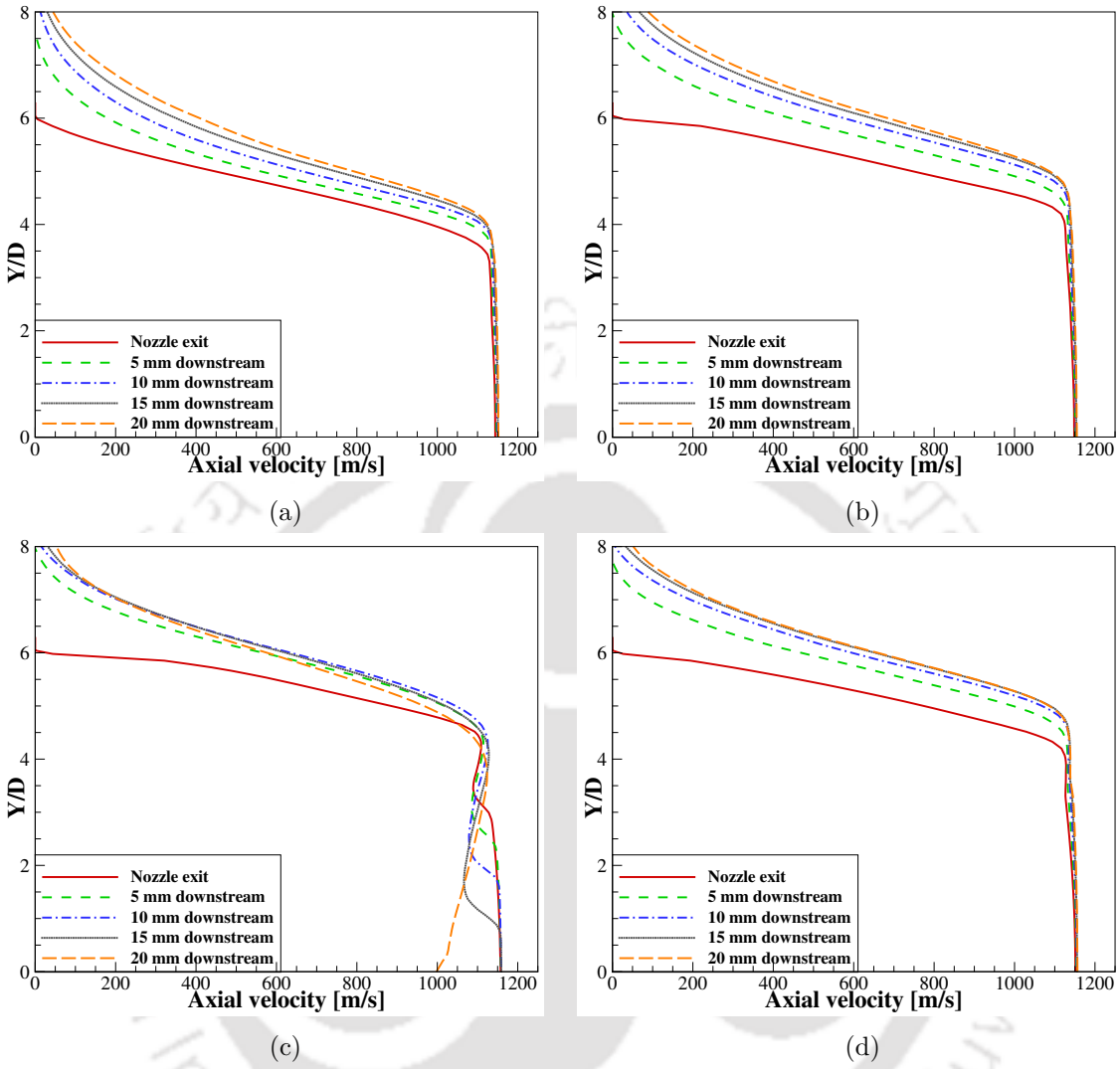

Figure 5.8: Radial profile of axial velocity at the exit and four axial locations downstream the exit of a) conical nozzle, b) $N1$, c) $N2$, and d) $N3$.

this disturbance is weaker for nozzle $N1$ and it is not present in nozzles $N2$ and $N3$.

5.7 Off-design conditions performance

Beyond the exit pressure ratio, it is seen that total temperature governs the nozzle design. As the nozzle shape is designed to meet a specific value of total temperature, the nozzle is expected to operate with this value as long as the nozzle pressure ratio is sufficient to create a choking condition. Nonetheless, it would be impractical for a nozzle to operate with such constraint alone, and the usability should be extended further. Hence, off-design conditions are imposed on the selected nozzle, i.e., with higher and lower total temperature than the design conditions. Thus, off-design simulations are performed on the nozzle $N1$ for lower, 500 K, and higher, 1200 K, sonic temperature, keeping the same geometrical

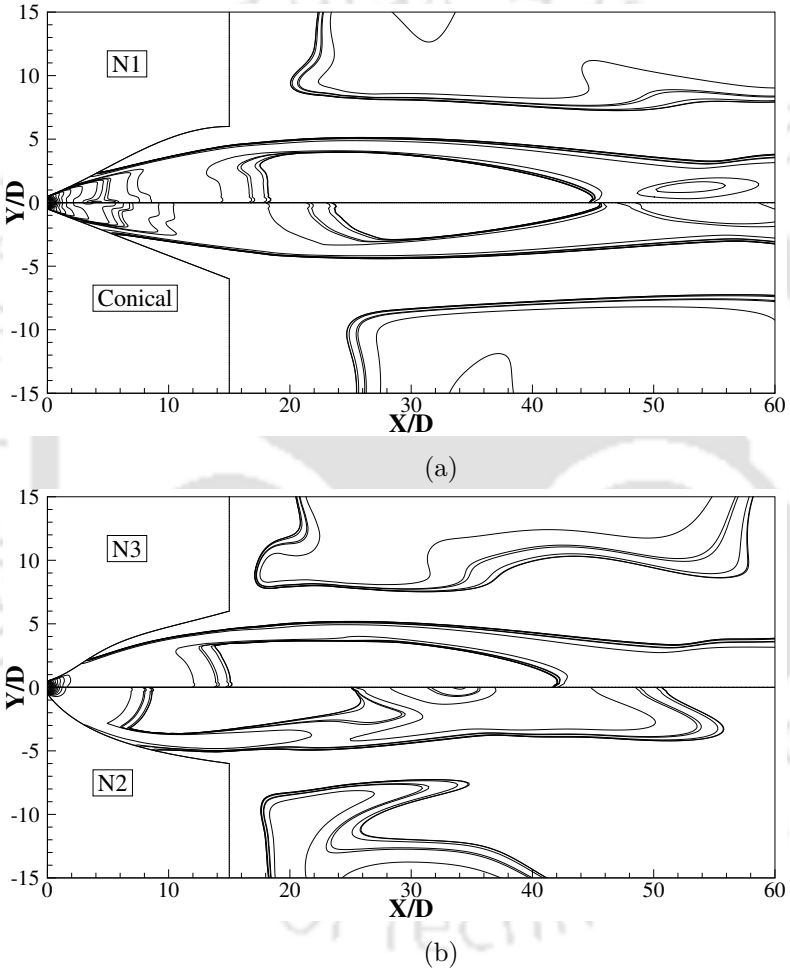

Figure 5.9: Isodensity lines for the a) conical nozzle vs. $N1$ and b) $N2$ vs. $N3$.

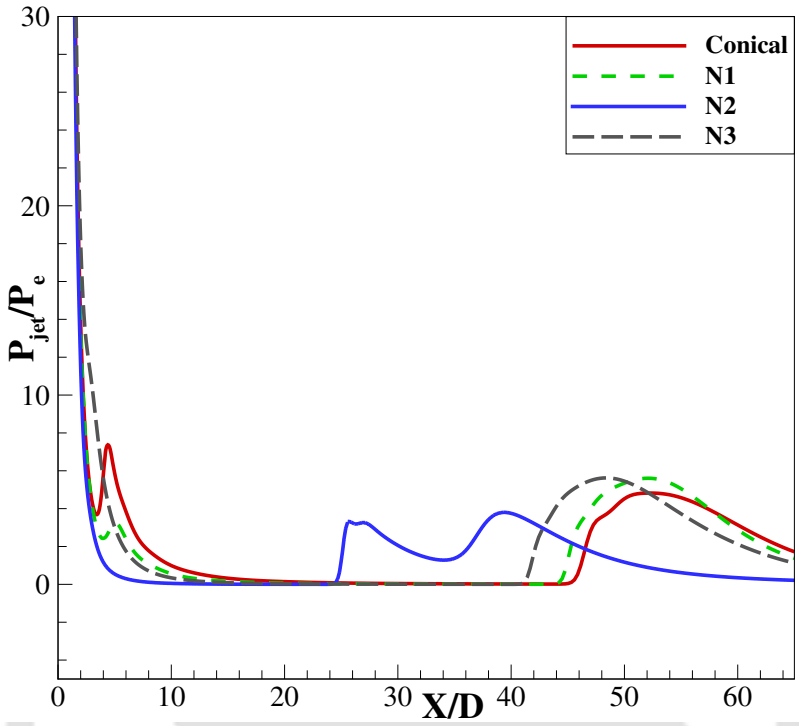

Figure 5.10: Axial pressure distribution in the near-field area for the four nozzles.

constraints and pressure ratio. The results are compared with the design condition, 975 K sonic temperature, in the sense of velocity distribution along the normal direction. Figure 5.11 depicts the normalised radial (v^*) and axial (u^*) velocity distributions at the nozzle exit plane for design and off-design conditions. Figure 5.12 illustrates the radial distribution of radial (v^*) and axial (u^*) velocities at an axial location of 10 throat diameters downstream the nozzle exit for design and off-design conditions. Looking at Fig. 5.11 and 5.12, the nozzle is proved to operate at lower and higher temperature with no disturbance in the velocity profile. However, and as expected, as the temperature increases, the shear layer grows thicker at the nozzle exit and downstream of the exit.

5.8 Comparison with the nozzle of Rao [79]

In order to compare the present procedure with an already established method to construct a nozzle wall, the nozzle obtained by the proposed optimisation algorithm ($N1$) is compared with the nozzle of Rao [79] which is mainly constructed for the maximum thrust rocket nozzle with zero back pressure. Maximum thrust requires a radially-uniform flow at the nozzle exit, and therefore an ideal rocket nozzle is designed to produce a uniform flow [119].
The dimensions of Rao's nozzle are taken as input to the optimisation code for air as a gas and total temperature of 1300 K. Simulations for both of the nozzles are then performed for a total pressure ratio of 2200. The dimension of the nozzle are kept as mentioned in the reference [79], the nozzle length is 8.19 throat radius and exit radius is 4.4 throat radius.

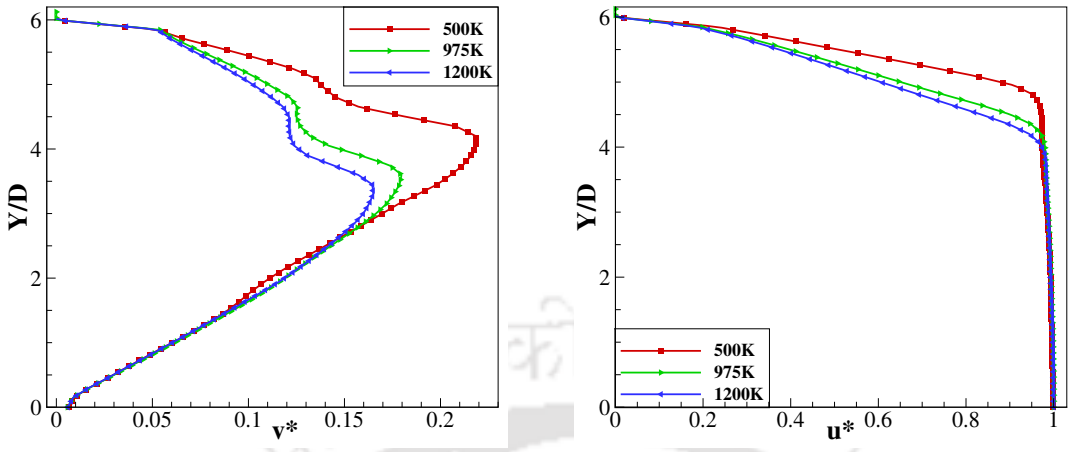

(a) Radial velocity. (b) Axial velocity.

Figure 5.11: Velocity profile at the nozzle exit plane for different operating temperatures.

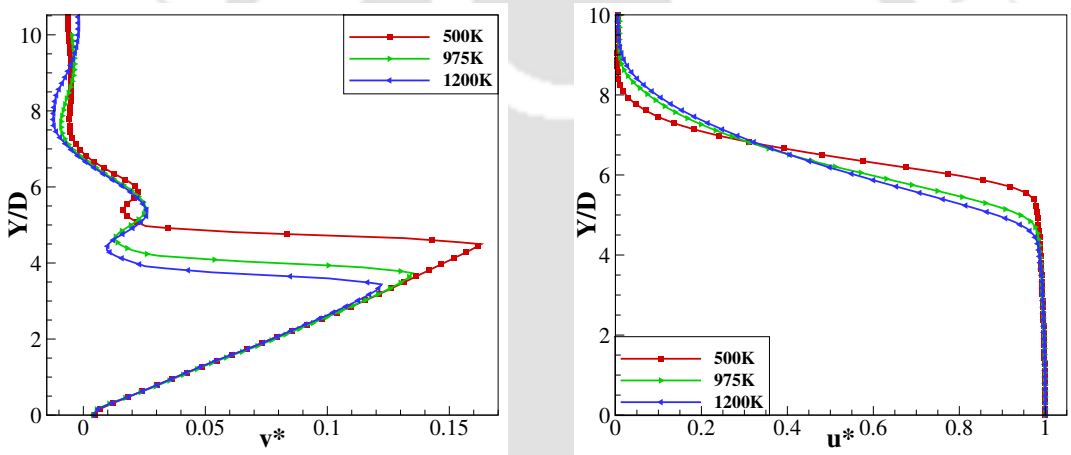

(a) Radial velocity. (b) Axial velocity.

Figure 5.12: Velocity profile at 10 throat diameters downstream of the nozzle exit plane, for different operating temperatures.

The comparison results are plotted in Fig. 5.13 in terms of numerical schlieren images for the flow fields. Rao's nozzle shows an internal shock at the nozzle due to the high divergence angle. Although the design of the nozzle has a small slope immediately downstream of the throat, the nozzle wall tends to have a steep slope for the rest of the design. Both nozzles show identical axial length of potential core as they have the same axial location for the shock reflection point. In the sense of radial length, the internal shock in Rao's nozzle appears to decrease the height of the potential core, causing it to be limited in the radial direction.
To probe the flow at the nozzle exit plane, the radial distribution of density at the nozzle exit is depicted in Fig. 5.14 for the nozzle of Rao and $N1$ which is constructed using the present optimisation algorithm and the dimensions from Rao [79]. The radial distance in this figure is non-dimensionalised with the exit radius of the nozzle, R_e. The nozzle $N1$ shows more uniformity at the nozzle exit, whereas the nozzle of Rao shows a disturbance in the density

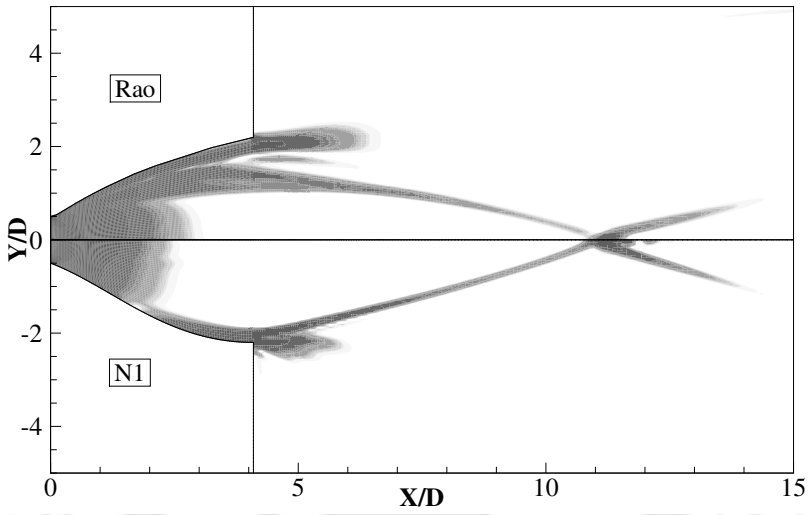

Figure 5.13: Numerical schlieren images for Rao's nozzle [79] and nozzle $N1$.

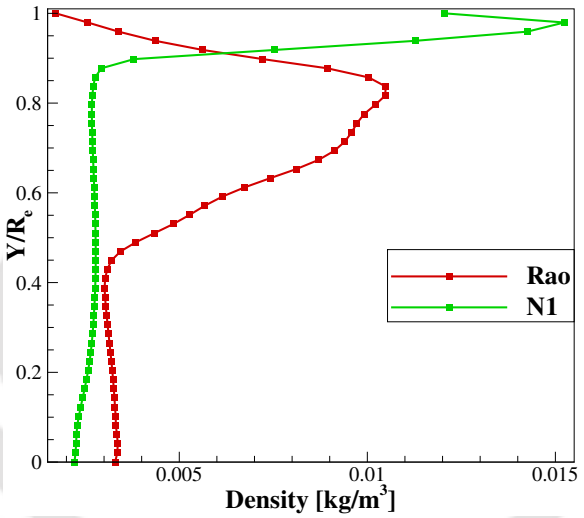

Figure 5.14: Radial density distribution at the nozzle exit for Rao's nozzle [79] and nozzle $N1$.

distribution that can be attributed to the internal shock which is extended downstream the nozzle exit plane. Furthermore, nozzle $N1$ appears to have a higher potential core as the uniform density distribution extends for almost 90% of the exit radius.

The flow emitting from nozzle $N1$ is of particular interest for spectroscopic applications, and therefore, the nozzle has been fabricated and used for experimental purposes. The details of the experiment are available in Appendix A.

5.9 Conclusions

This chapter focuses on the supersonic nozzle shape optimisation, utilizing gas dynamic relations and the method of steepest descent to design the diverging section of a super-

sonic nozzle. The low-fidelity flow solver is found to be useful to construct a nozzle with a radially-uniform flow at the outlet, while incorporating different mathematical techniques to implement the optimisation method. The resulting nozzle is then imported into an in-house CFD solver which is treated as a high-fidelity framework to validate the low-fidelity solver results. The influence of restricting the initial angle of divergence on the expansion trend of the gas is highlighted, and it shows that restricting the angle allows the gas to expand gradually within and outside the nozzle, which extends the potential core further downstream. The impact of viscosity is shown in developing the boundary layer at the nozzle wall and the resulting shear layer downstream. The shear layer is examined up to $10D$ downstream the nozzle exit, and its growth is explained based on the flow development inside the nozzle. flow properties for the nozzles are shown and deliberately discussed for the feasibility of design. Moreover, the nozzle chosen for experiment is tested for off-design conditions and it is proved to operate properly under different boundary conditions. The resulting nozzle from the current optimisation algorithm is compared with an existing nozzle from the literature to examine the uniformity of the flow at the nozzle exit plane.

CHAPTER 6

ALTITUDE COMPENSATING RINGED NOZZLE

Abstract

The increased demand for supersonic and hypersonic flows has motivated the researchers to find effective, efficient, and affordable methods to produce such flows in the laboratories. It is desirable for the rocket nozzle to operate efficiently at different altitudes, which made the Altitude Compensating Nozzles (ACNs) emerge as a feasible solution. In this chapter, a new method to produce a supersonic jet is proposed, namely, a ringed nozzle. The nozzle consists of a stack of parallel rings that serves as a nozzle with bleeding slots. This design can be utilised to obtain different exit Mach numbers and to attain the desired performance according to the jet requirements and perform under different pressure ratios, serving as an ACN. The stack of rings might be altered to tailor nozzle shape and area ratio corresponding to the nozzle requirement. The numerical simulations show promising results and prove that the bleeding can also help in reducing the thickness of boundary layer, and control flow separation at the nozzle wall.

6.1 Introduction

Whereas Chapter 5 deals with the challenge of constructing a supersonic nozzle, more engineering challenges arise, one of which is the nozzle ability to operate in different conditions. It is well-established that supersonic flights encounter varying ambient pressure while ascending and descending, and therefore, the efficiency of the nozzle (or the entire engine) is affected by the ambient (back) pressure. Hence, altitude compensating nozzles in many types were invented to overcome the varying pressure problem. A widely used ACN is the dual-bell nozzle [98] which is explained in Section 1.6. This nozzle operates ideally at two different altitudes and it is believed to improve the engine performance compared with the conventional nozzle. In this chapter, we propose another arrangement that would possibly help tackling this challenge; the ringed nozzle, a set of rings stacked parallelly to operate as a

conventional nozzle, with the ability to change the area ratio according to the back pressure. The concept is illustrated in Fig. 1.7. Here, Section 6.2 shows the computational domain that is employed to model the concept, Section 6.3 depicts the flow field of a supersonic nozzle flow, Section 6.4 explains the nozzle arrangement and design, Section 6.5 deals with the changes occurring in the flow due to the use of ringed nozzle, Section 6.8 provides an insight on how this nozzle operates under off-design conditions, and Section 6.9 highlights the salient results of this chapter.

6.2 Computational domain and boundary conditions

As the supersonic/hypersonic nozzle flow is highly sensitive to the domain, it requires to extend the dimensions of the domain so that the boundary conditions do not affect the internal flow field, and there will be no interaction between boundaries [32]. Thus, the length of the domain is kept as 300 throat diameters, and its height as 150 throat diameters. This domain includes the supersonic part of the nozzle, gaps between the rings and nozzle outlet. For the current simulations, domain inlet is set for sonic conditions, i.e., $M = 1.0$, $P_0/P_b = 2200$, and $T_0 = 1300\ K$. The nozzle wall and rings are treated as adiabatic walls. The computational domain is initialised with the outlet conditions, corresponding to the desired pressure ratio, and is illustrated in Fig. 6.1 along with the boundary conditions. The mesh lines are clustered towards the nozzle interior and the near-field to capture the flow accurately. The initial mesh has $59,400$ nodes which are then enhanced up to $81,000$. A further enhancement in the mesh, up to $141,300$ nodes shows a similar solution as that of the previous mesh. Hence, the solution is found to be independent of the mesh at $81,000$ nodes. The axial pressure distribution supporting it is shown in Fig. 6.2.

6.3 Flow field properties

Supersonic nozzle flow has a complicated jet structure, having boundary layer, expansion waves downstream the throat, extended shear layer downstream the nozzle exit, and the point of jet reflection. These flow features get altered with the boundary condition and the nozzle geometry. Nevertheless, typical features of the ideally-expanded and underexpanded jet are illustrated in the numerical schlieren image (Fig. 6.3) obtained from the current CFD simulation for a typical governing nozzle pressure ratio of 2055 and a conventional conical nozzle. The flow features depicted in this figure would be referred in the analysis. The usability of the proposed ringed nozzle is initially addressed numerically, considering Argon ($\gamma = 1.67$ and $R = 208\ J/kgK$) to be the working fluid for its significance in spectroscopic applications. The nozzle is designed accordingly with a throat diameter of 2.0 mm, exit diameter of 24.0 mm and a length of 30.0 mm, along with 1300 K total temperature. The nozzle pressure ratio, NPR, is set as 2055, which corresponds to exit pressure ratio of 1000, considering Argon properties.

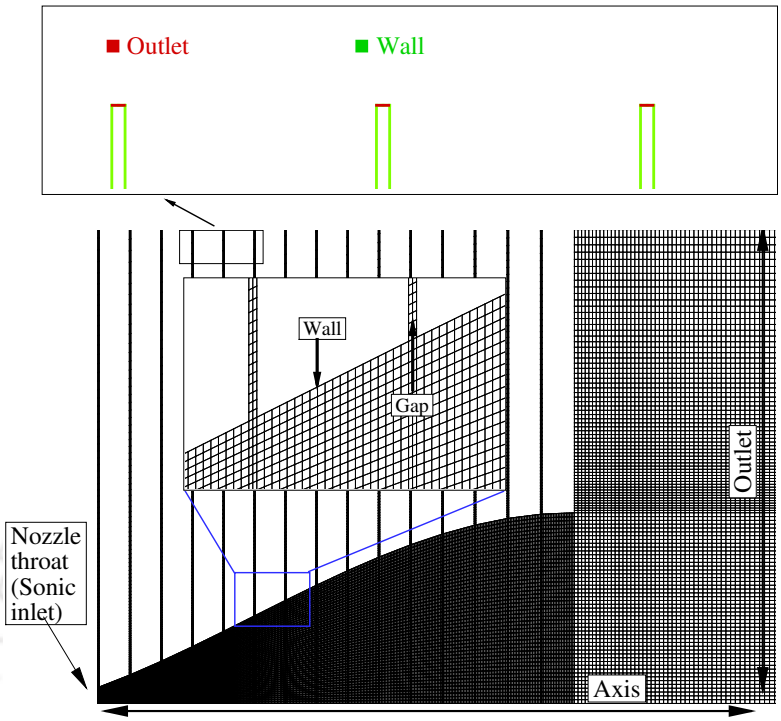

Figure 6.1: Domain and mesh used for the simulations.

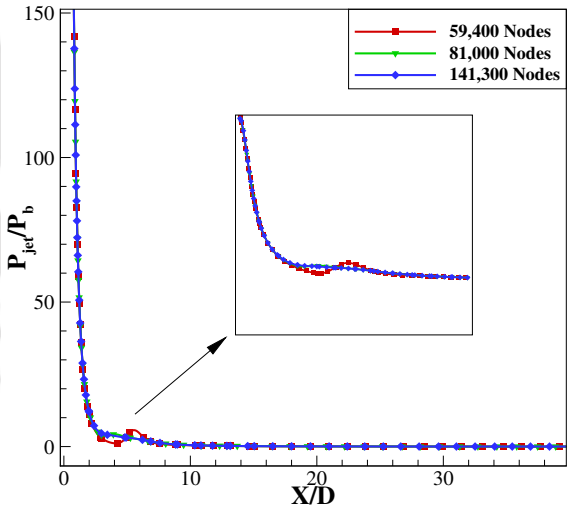

Figure 6.2: Axial distribution of the jet pressure ratio for three different meshes.

The conical nozzle is capable of producing a supersonic jet with almost the desired Mach number. However, the jet at the nozzle exit and downstream might have a certain non-uniform radial distribution for Mach number and other jet properties, like density and temperature. This discrepancy is caused by the spherical expansion of the jet, and the growth of boundary layer. Therefore, the optimised nozzle $N1$ which is developed in Chapter 5 is chosen to tackle these challenges. Moreover, the gaps between the rings allow a gas loss from the flow, and that has an influence on the flow properties within and downstream the nozzle. Hence,

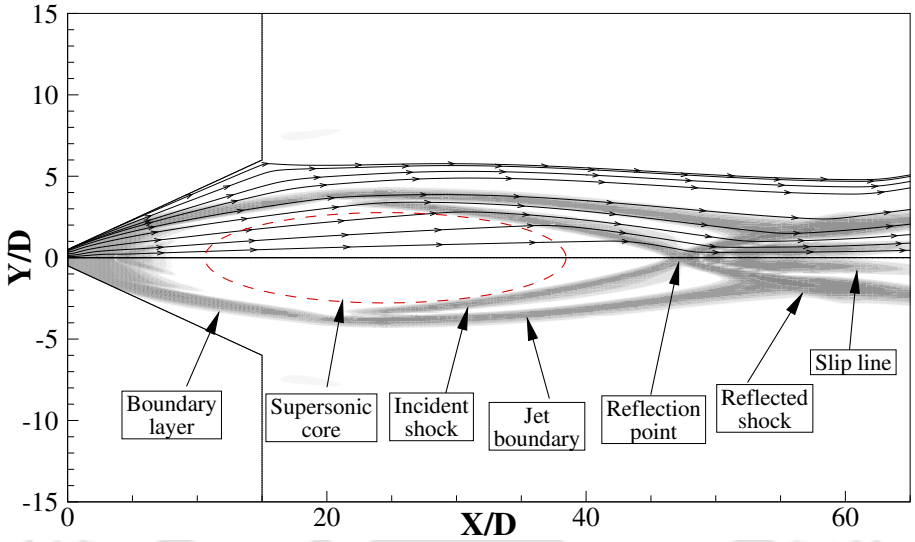

Figure 6.3: Supersonic jet components.

numerical schlieren images are used to illustrate the flow field.

6.4 Flow through conical and contoured ringed nozzle

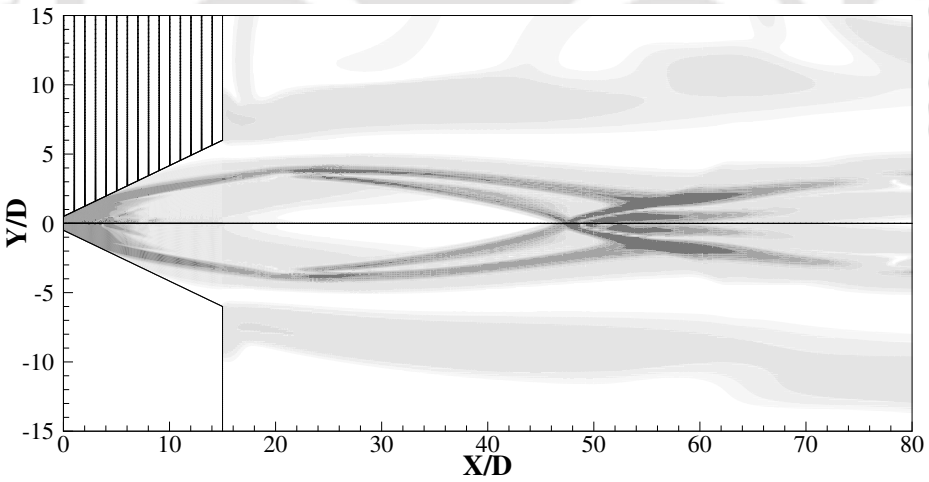

Figure 6.4: Numerical schlieren image for conical nozzle (bottom) and conical ringed-nozzle (top).

Initial simulation is performed to compare the flow through ringed conical nozzle and the classical conical nozzle. Here, the gap between the rings is considered to be 0.1 mm, which corresponds to 0.05 throat diameter. Figure 6.4 shows a comparison between the numerical schlieren contours for the regular conical nozzle and the ringed conical nozzle with the same above-mentioned dimensions. One can notice from the figure that the jet is not remarkably altered by replacing the regular nozzle with rings. This can be attributed to the small amount of mass that bleeds through the gaps between the rings, that is, using a conical nozzle causes

the flow to separate from the wall and hence does not allow the mass to escape through the gaps. The total pressure probed on the axis at the exit plane is found to drop by 0.64% when using the above-mentioned rings.
Efforts are then extended to design a contoured nozzle using the method discussed earlier for the same constraints and conditions. Further, the contoured nozzle is also replaced with stacked rings, and a few simulations are performed on the resulting domain with different gap widths. Figure 6.5 shows the effect of altering the bleeding gaps between the stacked rings. Relatively large gap leads to more mass loss which decreases the jet mass flow rate. Therefore, as the gap decreases, the jet attains higher mass flow rate, and higher local pressure as a result. Thus the supersonic core length is approximately 27 throat diameter downstream for a gap width of $0.3D$, and it extends to $29D$ and $31D$ for a gap width of $0.15D$ and $0.05D$, respectively. This is also reflected in the axial pressure distribution in Fig. 6.6.

Moreover, it is evident from Fig. 6.5 (c) that, the supersonic core of the jet, for a small gap width, almost attains the location of the reflection point for the conventional contoured nozzle. This shows that minimizing the gap width decreases the lost mass flow through the bleeding slots and makes it approach the performance of a conventional nozzle. Thus, the expansion trend, represented by axial pressure distribution, has to be thoroughly studied to discriminate the influence of each set of rings on the resulting jet. Figure 6.6 illustrates the axial pressure distribution, from the nozzle throat up to $50D$ downstream, for the conventional contoured nozzle compared to the ringed nozzles with different gap width.

It is also seen in Fig. 6.6 that the conventional nozzle and the ringed nozzle with the smallest gap width have matching axial reflecting points, around $31D$ downstream the nozzle exit plane, compared to nozzles with wider gaps, that have reflection points at $29D$ and $27D$ downstream for a gap width of $0.15D$ and $0.3D$, respectively. This is imputed to the higher mass flow rate in case of conventional nozzle, and the almost negligible mass loss in the narrow gap, $0.05D$. In Fig. 6.6, the pressure distribution is seen to be disturbed within the nozzle in the initial phase of expansion while using the stack of rings. Nonetheless, it is seen to be smooth for the conventional nozzle. This is due to the sharp-edged ring that impacts the flow and causes what appears to be a slight pressure increment for wider gaps. However, this effect is not noticed in the flow within the conventional nozzle, and it is nearly not visible for ringed nozzle with gap width $0.05D$. This effect is seen to be more impactful as the gap width increases, because the flow gets more distance to expand and increases its Mach number before hitting the sharp edge of the first ring. Hence, the gap width is recommended to be as narrow as possible to imitate the performance of a conventional nozzle and avoid the formation of a weak shock within the nozzle. Nevertheless, this weak shock gets weaker and vanishes as it propagates within the nozzle, as observed in the schlieren images in Fig. 6.5.

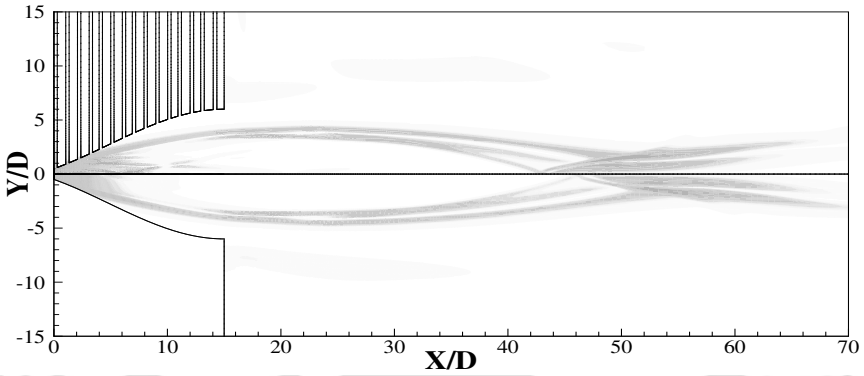

(a)

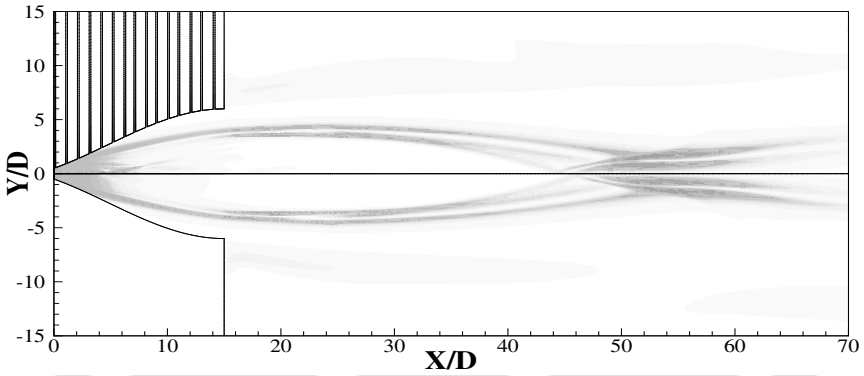

(b)

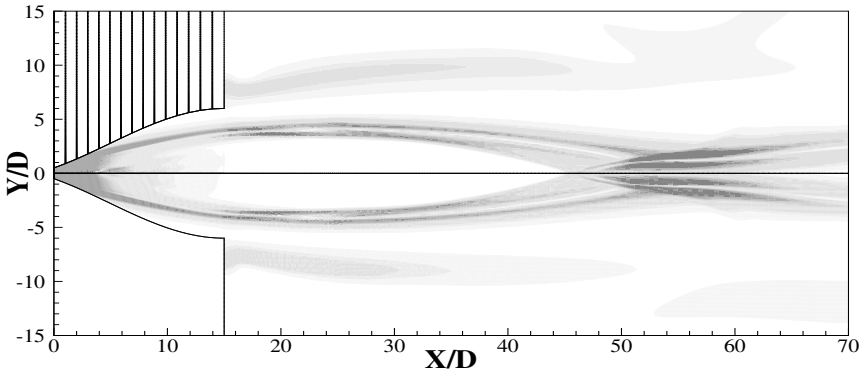

(c)

Figure 6.5: Numerical schlieren images of a conventional nozzle versus ringed nozzles with different gap widths: (a) Gap width =0.3D, (b) Gap width =0.15D and (c) Gap width =0.05D

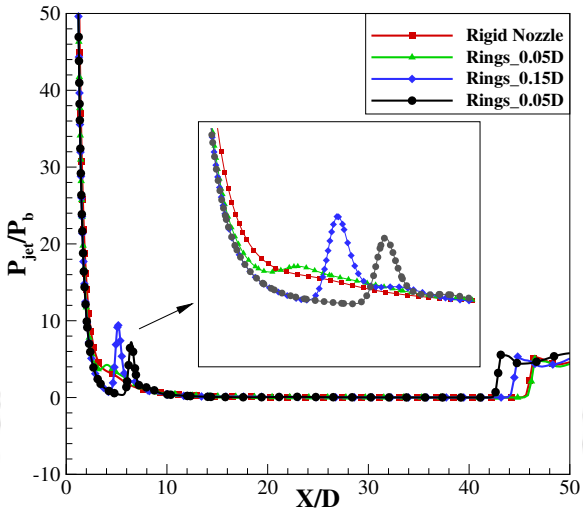

Figure 6.6: Axial pressure distribution for rigid and ringed nozzles.

6.5 Flow behaviour for ringed nozzle

The flow properties are measured at a point of the axis in the exit plane, as a reference, to determine the effect of using a ringed nozzle. Figure 6.7 depicts the density and Mach number at the reference point for a conventional nozzle (represented by a gap width of zero) and ringed nozzles with different gap widths. It shows that, the jet density increases as the gap width decreases, that is, the smaller gap allows less mass loss from the nozzle. Furthermore, Mach number seems to follow a different trend, it attains a maximum value for the wider gap and then drops as the gap width decreases. The plot illustrates that these two parameters, density and Mach number, are inversely proportional to each other. This is attributed to the compression effect by the regular nozzle wall on the jet, making it more difficult for the gas to expand, whereas the ringed nozzle eliminates the low-momentum boundary layer and allows more expansion within the nozzle, which in turn increases Mach number and decreases the density as the gap width increases. It is also noticed from Fig. 6.7 that the point corresponding to $0.05D$ follows a non-monotonic trend. To understand the turning of jet properties at this point, one has to consider that the density and Mach number at the nozzle exit plane are subjects of two parameters, the mass flow rate and the rate of expansion. A small gap width allows a minimal mass loss that corresponds to potential loss, and hence a slight decrease in Mach number without remarkable effect of expanding. However, when the gap width increases, the gas is allowed to expand more freely, and hence there is increase in Mach number and decrease in density. Although the bleeding slots take away the low-momentum part of the flow, they deprive the flow from certain energy content along with the lost mass flow. Therefore, as an indicator for potential, the ratio of total pressure (PR_0) at the exit of the nozzle ($P_{0,e}$) to the stagnation pressure (P_0) is calculated

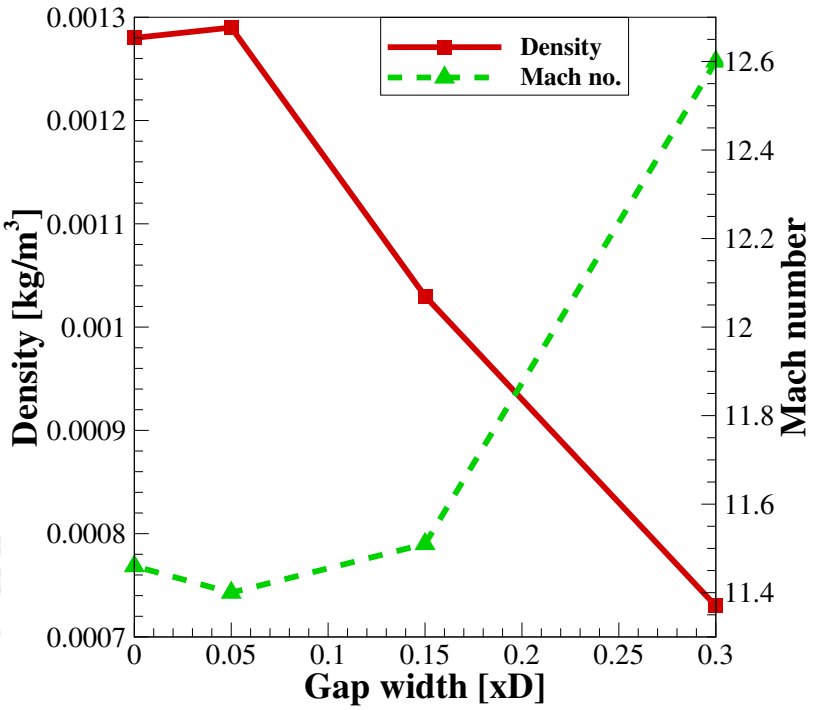

Figure 6.7: Jet density and Mach number at the nozzle exit for different gap widths.

as given by Eq. 6.1 and plotted in Fig. 6.8.

$$PR_0 = \frac{P_{0,e}}{P_0} \tag{6.1}$$

where, $P_{0,e}$ is the total pressure at the intersection point of nozzle axis and nozzle exit plane for the conventional contoured nozzle and the ringed nozzles with a certain gap width, $0.05D$, $0.15D$ and $0.3D$.

It can be clearly seen from Fig. 6.8 that total pressure decreases when the rings are introduced, and decreases further as the gap width increases. The total pressure ratio attains values of 0.75, 0.80 and 0.98 for gap width of $0.3D$, $0.15D$ and $0.05D$, respectively. Further, the flow seems to keep more than 0.99 of its total pressure as it expands through the conventional nozzle, and thus indicates an isentropic expansion throughout the chosen nozzle. Therefore, the presence of bleeding slots at the nozzle wall removes a certain amount of the flow potential, and this effect can be mitigated by narrowing the gap width between the stacked rings. To analyse the nozzle performance, the thrust coefficient and specific impulse, for the contoured nozzle and subsequent ringed nozzle, are calculated as follows:
The thrust is calculated as,

$$T = m^*.V_{exit} + (P_e - P_b)A_e \tag{6.2}$$

where m^* is the mass flow rate at the exit plane, A_e is the nozzle exit area, and V_{exit} is the exit velocity at the nozzle axis.

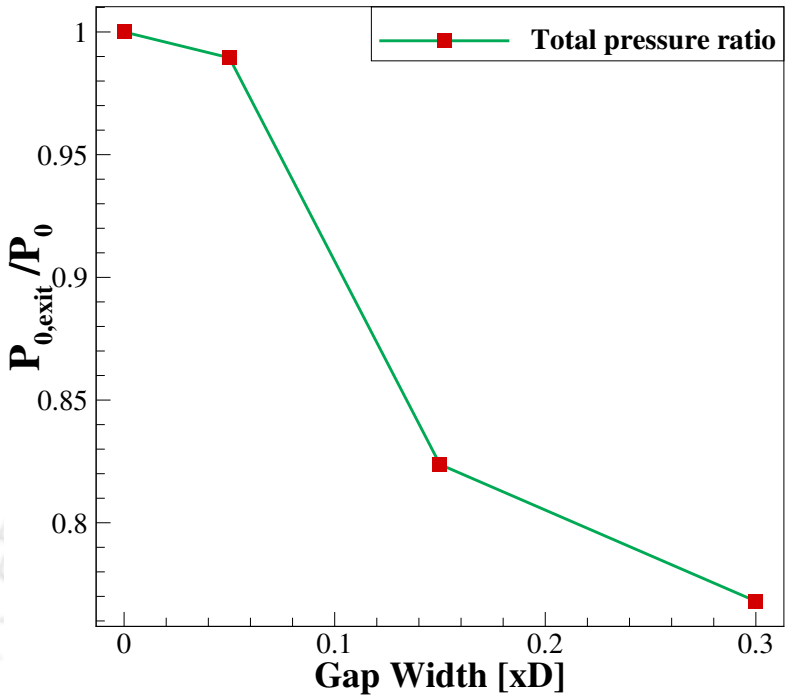

Figure 6.8: Ratio of total pressure at the nozzle exit plane vs. the gap width

The specific impulse, I_s, is defined as the thrust per unit weight flow at sea level:

$$I_s = \frac{T}{m^* g_0} \tag{6.3}$$

Moreover, the thrust coefficient is given by Eq. 6.4:

$$C_t = \frac{T}{P_0.A_t} \tag{6.4}$$

where A_t is the throat area and P_0 is the total pressure.

The thrust coefficient and specific impulse are then plotted in Fig. 6.9. It is clear that thrust is proportional to the mass flow rate from Eq. 6.2. Hence, the mass loss through the gaps reduces the thrust and consequently the thrust coefficient. It is also noticed that the slope of C_t line is relatively lower between the conventional nozzle and the nozzle with gap width $0.05D$, whereas it decreases faster when the gap width increases. On the other hand, the specific impulse is, if anything, inversely proportional to the mass flow rate. Therefore, it is seen to increase slightly in the initial stage (gap width of $0.05D$). However, with further increment in gap width, other factors (such as exit pressure and exit velocity) interfere significantly, and the specific impulse decreases.

Figure 6.9: The thrust coefficient and specific impulse for contoured ringed nozzle with different gap width.

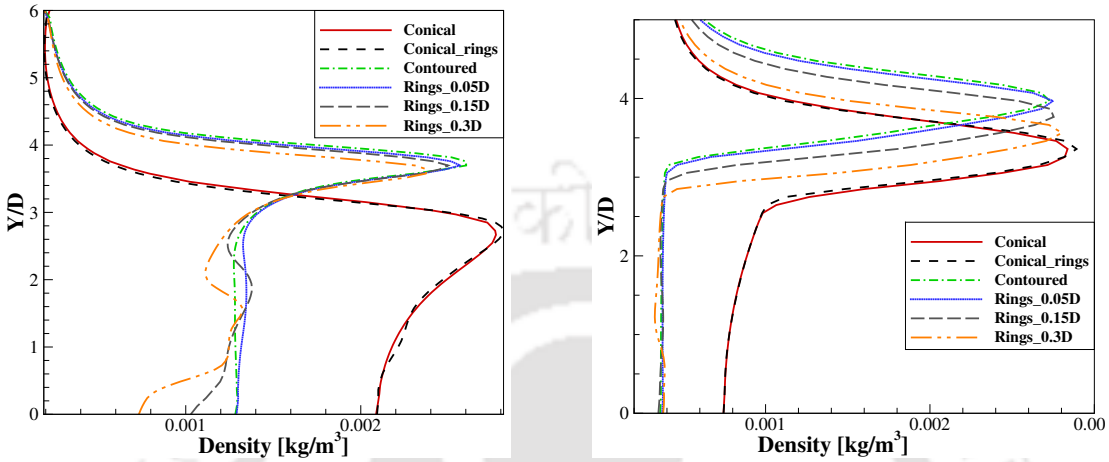

(a) (b)

Figure 6.10: Radial distribution of density at two different locations for several nozzles: (a) At the nozzle exit plane and (b) At axial location $15D$ downstream the exit plane.

6.6 Flow Uniformity Analysis

As the radially-uniform flow jet is preferable at the outlet of the nozzle for many applications, it becomes of great interest to plot the radial distribution of jet properties at the nozzle exit plane to investigate the role of using the contoured nozzle and subsequently the ringed contoured nozzle. Thus, the radial distribution of jet density is plotted in Fig. 6.10 (a) for conical, contoured and ringed nozzles.

It is noticeable from Fig. 6.10 (a) that the jet resulting from contoured nozzle and the subsequent ringed nozzle is expanded more than the jet resulting from conical and ringed conical nozzles. It is also seen that the presence of rings creates a disturbance in the radial distribution at the nozzle exit, resulting from the impact of sharp-edged rings, and propagates downstream. However, the variation in distribution is decreased as the gap width is decreased, and the contoured ringed nozzle with a minimum gap width shows a similar trend to the conventional contoured nozzle. Furthermore, in Fig. 6.10 (b), the radial distribution of density is plotted at an axial location of $15D$ downstream of the nozzle exit plane to examine the uniformity and height of the inviscid core after it leaves the nozzle. It can be deduced that the jet maintains its height for the said axial distance and further enhances its radial uniformity as it propagates downstream. Moreover, the conventional nozzle and the ringed nozzle with minimum gap width seem to attain the maximum core height, manifesting the improvement in the flow resulting from nozzle shape optimisation. Furthermore, one can notice from Fig. 6.10 (a) and 6.10 (b) that the radial distribution in the shear layer area is not regular, i.e., the density starts with a low value outside the jet boundaries, and grows to a

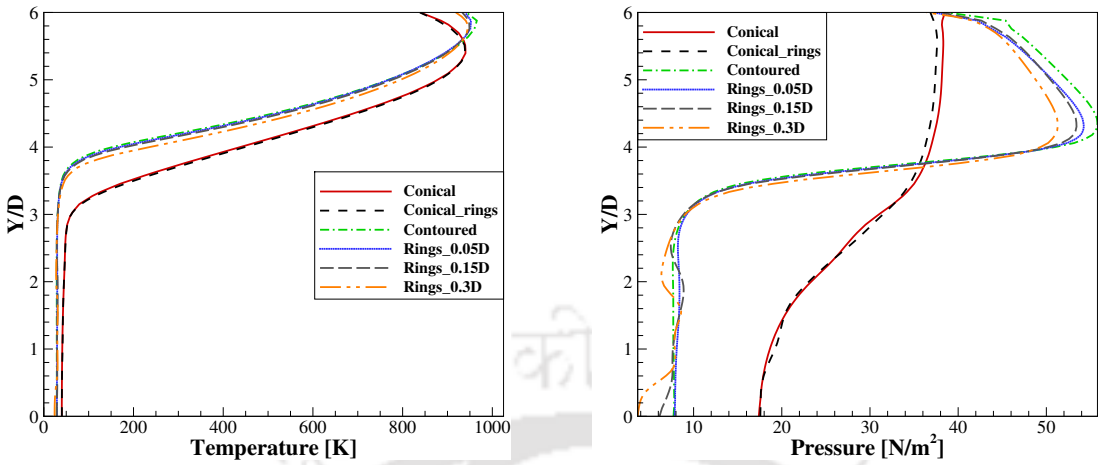

(a) (b)

Figure 6.11: Radial distribution of temperature and pressure at the nozzle exit plane: (a) Temperature and (b) Pressure.

large value within the shear layer, then decreases rapidly towards the inviscid core. To probe this phenomenon, other jet parameters such as pressure and temperature have to be studied. Hence, the temperature and pressure distribution are plotted at the same two locations, viz, at the nozzle exit plane and at an axial location of $15D$ downstream the exit. Figure 6.11 shows the radial distribution of temperature and pressure at the nozzle exit plane.

Moreover, Fig. 6.12 shows the radial distribution of temperature and pressure at $15D$ downstream the nozzle exit. Figures 6.11 and 6.12 reveal a regular distribution for the temperature throughout the shear layer. However, the pressure is seen to increase and then decrease across the shear layer, adopting the same trend of density, which justifies the density distribution. In the case of free supersonic jet, the shear layer is formed from the viscous effects, thus, the shear layer has a rapid variation in density and pressure. That is why the pressure and density are noticed to rapidly increase, and then decrease to match the flow parameters of the supersonic inviscid core. This process causes the irregular radial distribution of density and pressure noticed in Fig. 6.10, 6.11 and 6.12.

Although the ringed nozzles show non-uniformity in the flow field at the nozzle exit and downstream, the ringed nozzle with small gap width, namely $0.05D$ shows a matching profile of the conventional contoured nozzle throughout the jet core. Thus, using a ringed nozzle with narrow gaps imitates the performance of a conventional nozzle with minimal mass flow loss and has the ability to compensate the change in back pressure.

Since the supersonic jet is desired for different applications that have different preferences regarding the jet, it is of great interest to further examine the jet velocity at the exit. Therefore, the radial distribution of normalised axial and radial velocity at the nozzle exit plane is plotted in Fig. 6.13 for the conventional nozzle ($0.00D$) and the ringed nozzles with three gap widths. It is evident here that the nozzle with $0.05D$ gap width would be the most feasible for the maximum length of inviscid supersonic core. If minor compromise is accepted for

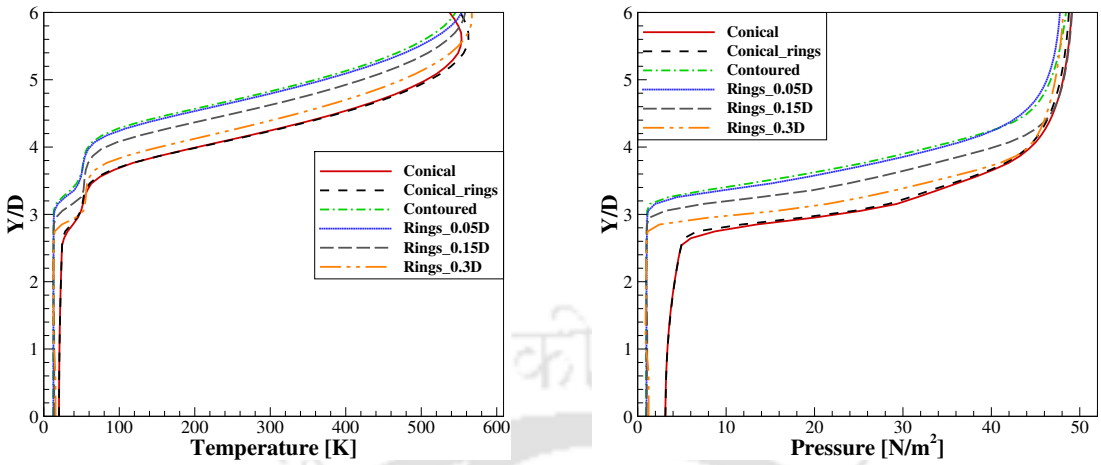

(a) (b)

Figure 6.12: Radial distribution of temperature and pressure at $15D$ downstream of nozzle exit plane: (a) Temperature and (b) Pressure.

the inviscid core length, then higher uniformity at the nozzle exit can be seen for the nozzle with $0.3D$ gap width since it produces the minimum value of radial velocity at exit. Hence, the nozzle gap can be adjusted as per the requirement of the jet.

6.7 Altitude Compensation Effect

The ringed nozzle offers a significant advantage in achieving optimal performance across a range of pressure ratios compared to conventional contoured nozzles. To demonstrate this advantage, a comparison is made between the two nozzle types at a pressure ratio corresponding to the dimensions of the conventional nozzle. The nozzle geometry corresponds to an area ratio of $A/A^* = 144$, resulting in a total pressure ratio of 25800. Schlieren images presented in Fig. 6.14 (a) reveal that both the conventional contoured nozzle and the ringed nozzle perform similarly under these conditions. The pressure ratio is then reduced to 11500, which corresponds to an area ratio of 88.83. To adjust for the change in operating conditions, six rings are removed from the end of ringed nozzle to achieve the required area ratio, while the conventional nozzle remains unaltered. The number of rings selected for the nozzle design is intended to demonstrate the altitude-compensating effect. As such, removing 2-3 rings is deemed inconsequential to the area ratio since the nozzle's exit is shaped to uniformly direct the flow. Conversely, excising numerous rings would eliminate a substantial portion of the nozzle's contoured segment and transform it into a semi-conical shape. This is due to the fact that the initial part of the diverging section is designed to accommodate most of the expansion process. The performance of both nozzles is evaluated under the new conditions, and the difference in performance is illustrated in the schlieren image shown in Fig. 6.14 (b).

The comparison of the ringed nozzle with the conventional nozzle in ideal operating

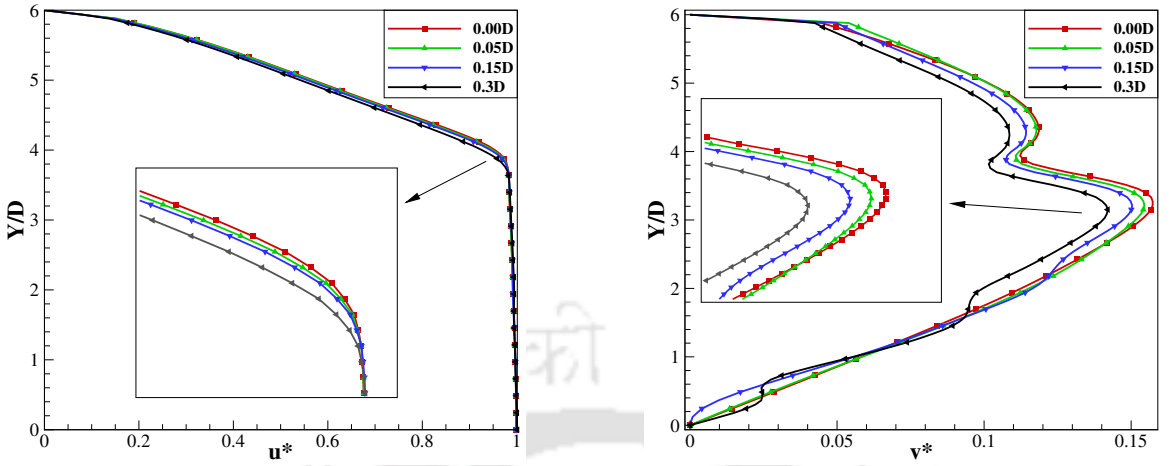

(a) (b)

Figure 6.13: Radial distribution at the nozzle exit for the normalised (a) Axial velocity and (b) Radial velocity.

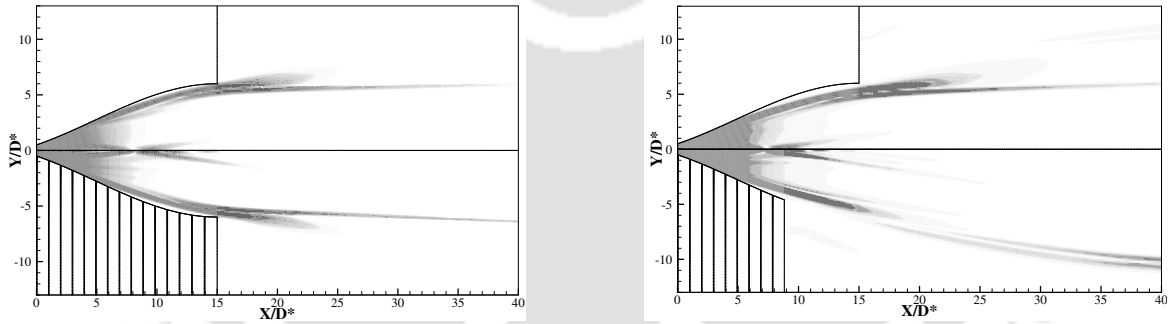

(a) (b)

Figure 6.14: Schlieren images comparing the conventional nozzle and ringed nozzle performance at NPR (a) 25800 and (b) 11500.

conditions, as presented in Fig. 6.14 (a), indicates negligible differences in performance. However, the ringed nozzle exhibits an advantage in adapting to changes in operating conditions. As demonstrated in Fig. 6.14 (b), when the pressure ratio decreases, the ringed nozzle is seen to qualitatively adapt for the change in operating condition, and produce a semi-ideally expanded jet. It should be noted that the remaining rings are a portion of the optimised nozzle shape for the initial dimensions, which may require re-optimisation for the new dimensions (the new length is 17.65 mm).

To provide more details, the thrust coefficient and specific impulse of the conventional and ringed nozzle are calculated and compared at the two different operating pressure ratios in Fig. 6.15. This figure shows that the ringed nozzle does not deviate from the performance of conventional nozzle in terms of specific impulse. However, it is seen to perform better in terms of thrust coefficient as it has higher value at low pressure ratio due to the adaptation

capability.

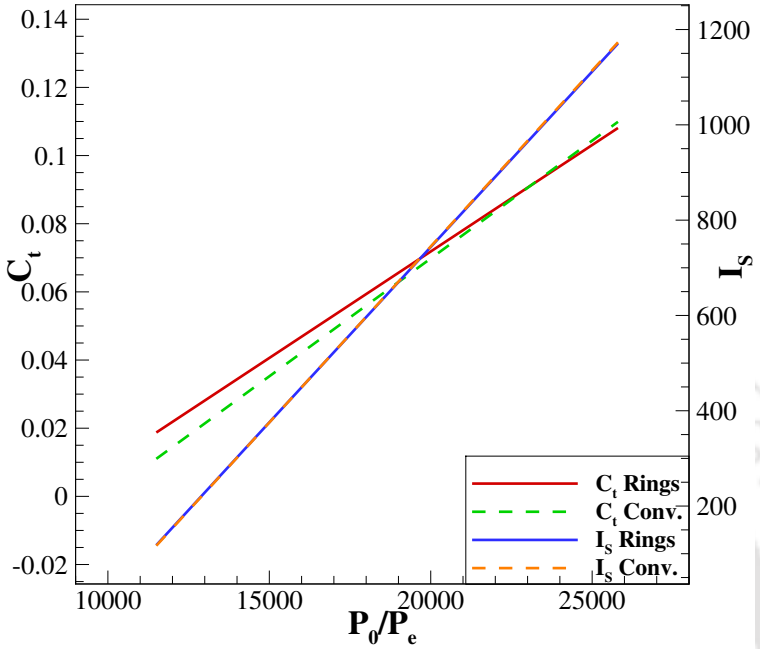

Figure 6.15: Variation of thrust coefficient and specific impulse for the ringed nozzle and conventional nozzle under two different operating conditions.

6.8 Operating under Off-design conditions

Whereas it is impractical to use a certain nozzle, or a set of stacked rings, for a specific pressure ratio, two more simulations are performed with different pressure ratios to examine the jet behavior throughout a range of pressure ratio for a ringed nozzle with a $0.05D$ gap width. Figure 6.16 depicts Mach contours for three exit pressure ratios, 1500, 1000 and 500.

Figure 6.16 shows that higher pressure ratios extend the axial dimension of potential core further downstream, that is, the reflecting point shifts downstream, and this observation agrees with the literature[31]. It is also noticeable that, the ringed nozzle operates efficiently at different pressure ratios as long as the choking condition is satisfied. However, as the pressure ratio increases, the expansion at the nozzle exit becomes stronger, which enlarges the thickness of shear layer and disturbs the uniformity of the jet. This effect can be easily seen in Fig. 6.16 as the axial extent of the inviscid core is less than $25D$ downstream the nozzle exit plane for a pressure ratio of 500, whereas it attains an axial distance of $30D$ and $40D$ for pressure ratios of 1000 and 1500, respectively.

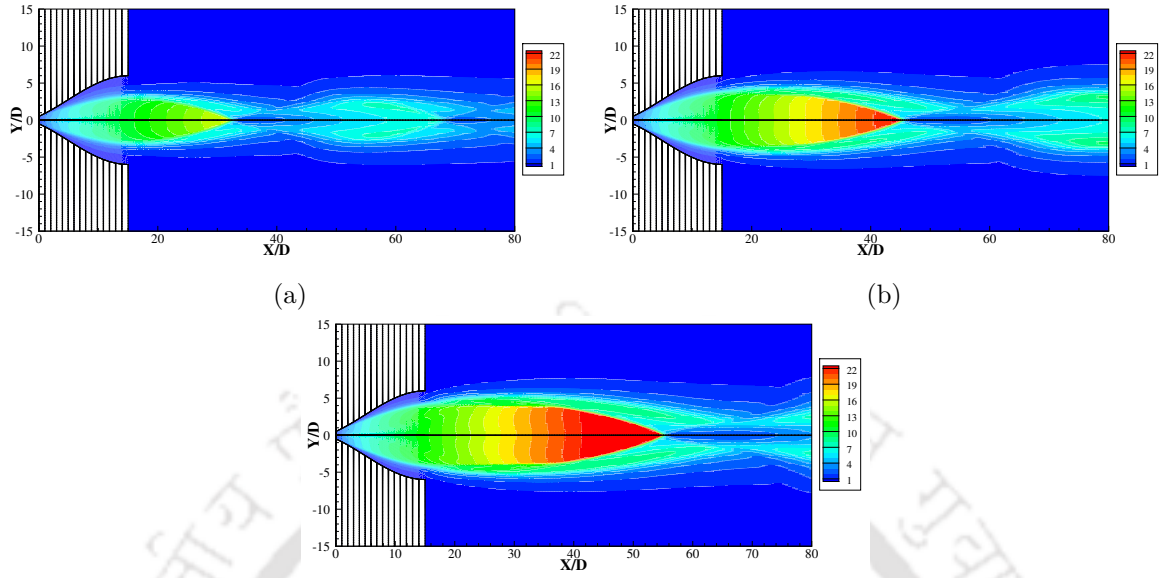

Figure 6.16: Mach contours for ringed nozzle at different pressure ratios: (a) PR =500, (b) PR =1000 and (c) PR =1500

6.9 Conclusions

This chapter aims to analyse a newly proposed Altitude Compensating Nozzle, the ringed nozzle. It suggests replacing the rigid nozzle wall with a stack of rings, which would benefit the quality of the flow at the nozzle exit and downstream, and account for the changes in the pressure ratio across the nozzle. The conclusion comprises the following findings:

- The ringed nozzle is a viable option for varying operating conditions, as its design maintains the jet properties if the gap width is minimised.
- The gaps between the rings are bleeding slots that remove the low-momentum part of boundary layer, which allows the jet to expand freely and decrease the thickness of shear layer downstream of the nozzle exit plane.
- The ringed nozzle with small gap width imitates the performance and expansion trend of a conventional contoured nozzle and keeps the mass loss, and therefore the energy loss, to the minimum.
- The ringed nozzle is seen to maintain the thrust coefficient and specific impulse when the gap width is kept as minimum.
- When the pressure ratio changes, the ringed nozzle is found to adapt for the change by removing or adding rings from the end to match the exit pressure with the back pressure.

- The specific impulse of the ringed nozzle does not deviate from the performance of a conventional nozzle when the pressure ratio drops. However, the adaptive capability of the ringed nozzle enhances the thrust coefficient under varying conditions. While the ringed nozzle is proven to be a potential solution for altitude-compensating performance, this design needs further experimental validation for actual in-flight performance.

CHAPTER 7

CONCLUSIONS AND FUTURE SCOPE

The previous chapters describe the results of thoroughly studying the free sonic and supersonic flows. The in-house CFD computer solver is found to be reliable in capturing different types of complexity in the flow field, i.e., the shock waves patterns and shock wave-shear layer interaction. Even though many assumptions (laminar flow and ideal gas) are made throughout the thesis, the results obtained are validated with experimental correlations and previous works in the literature.

7.1 Conclusions

The conclusions of this thesis can be summarized as follows:

7.1.1 Computational methodology

- An in-house flow solver based on Navier-Stokes equations is developed to solve the flow field of supersonic jets. The results prove the validity of the solver for such cases.
- A flow solver based on one-dimensional gas dynamic relations is also developed for the purpose of constructing supersonic nozzle wall shape. The solver seeks to minimise the radial velocity at the nozzle exit in collaboration with steepest gradient descent optimisation algorithm.
- The one-dimensional solver and the optimisation algorithm are found useful in obtaining nozzle wall shapes customised for different applications.

7.1.2 Underexpanded sonic freejet

- Increasing the exit pressure ratio is mainly seen to transform the jet from slightly to moderately and then extremely underexpanded jet, subsequently, the formation of

Mach disk and the transition from regular reflection to Mach reflection. Thus, the apparition of Mach disk is noted to be dependent on the pressure ratio and the specific heat ratio γ as it appears first for gases with $\gamma = 1.67$ at $P_e/P_b = 1.9$ and gases with $\gamma = 1.4$ and $\gamma = 1.27$ at $P_e/P_b = 2.0$ and $P_e/P_b = 2.15$, respectively.

- The turbulent simulations results show a high rate of diffusion and dissipation in the jet, causing high rate of energy loss, which restricts the free expansion of the gas and delays the apparition of Mach disk.

- The distance between the nozzle exit plane and the first normal shock (Mach disk) is deliberately studied and it is noticed to increase with the pressure ratio and γ. The increment in the location keeps a rate in the range $43\% - 58\%$ with an increase of 100% in the exit pressure ratio for the three gases. Such simulations are found to be useful to improve and incorporate necessary amendment in the existing correlations which would have been obtained from numerous experiments.

- The impact of the stagnation temperature on the location of Mach disk is almost unnoticeable in the considered range of temperature.

- It is observed that the pressure immediately downstream of Mach disk almost matches the back pressure with an accepted deviation, whereas the temperature rises above the inlet temperature and the ambient temperature which not only compensates for the loss in kinetic energy but also enhances the diffusion.

- The diameter of Mach disk is studied with different pressure ratios, temperature, and gases. It is seen to be proportional to the pressure ratio and inversely proportional to the total temperature, whereas the gas type does not affect the diameter remarkably.

7.1.3 Supersonic nozzle shape optimisation

- The low-fidelity flow solver is found to be useful in constructing a shock-free nozzle with a radially-uniform flow at the outlet, while incorporating different mathematical techniques to implement the optimisation method.

- Restricting the initial angle of divergence allows the gas to expand gradually within and outside to nozzle which extends the potential core further downstream. Further, the impact of viscosity is shown in developing the boundary layer at the nozzle wall and the subsequent shear layer downstream.

- Different nozzle designs are studied from the perspective of flow uniformity, the extent of potential core, and the growth of shear layer for each nozzle.

- The nozzle is tested for off-design conditions and it is proved to operate properly under different boundary conditions. The resulting nozzle from the current optimisation algo-

rithm is compared with an existing nozzle from the literature to examine the uniformity of the flow at the nozzle exit plane.

- One of the proposed nozzles is fabricated and tested, the experimental results appear to align well with the CFD predictions which indicates the validity of the current solver in predicting such flows.

7.1.4 The effects of upstream geometry

- Mach disk location is found to be slightly sensitive to the nozzle geometry. It depends on the flow potential loss within the nozzle, the smoother the expansion, the further Mach disk moves downstream. However, when the jet experiences shock waves within the nozzle, it loses a certain amount of potential which causes compressible flow region to decrease.

- Mach disk height is affected by the nozzle shape. Contoured nozzles produce the highest Mach disk, whereas diverging orifice produces the minimum-height Mach disk.

- The sonic line characteristics are influenced by the nozzle geometry. The sonic line is noted to take place at the end of converging area. Further, the smoothly converged nozzle causes the sonic line to be almost straight. Nevertheless, the straight nozzles with sudden contraction causes the curvature of sonic line to increase. The location and curvature of the sonic line is not seen to be affected by the pressure ratio.

7.1.5 Ringed nozzle

- A novel supersonic nozzle design, the ringed nozzle, is examined numerically to study the impact of rings on the jet properties. It is noticed that, the use of a ringed nozzle keeps the advantages of a conventional contoured nozzle as long as the gaps between these rings is kept to minimum. Further, the dimensions of inviscid core within the jet are preserved when the ringed nozzle is used.

- The gap size between the rings has been altered as to study its effect on the flow properties. It is proven that the gaps act as bleeding slots for the low-momentum part of boundary layer, that allow the jet to expand freely and decrease the thickness of shear layer downstream of the nozzle exit plane.

- The results show that ringed nozzle with small gap width imitates the performance and expansion trend of a conventional contoured nozzle and keeps the mass loss, and therefore the energy loss, to the minimum.

7.2 Scope of Future Work

In the light of current work, one should point out the limitations and drawbacks that could be considered in future works.

- Expanding the study to include two parallel supersonic, or one supersonic and one subsonic, streams. A turbulent model is in progress to address the instabilities in such flows.
- The hysteresis phenomenon of underexpanded jets has to be studied to examine the evolution of flow from low-pressure ratio up to high-pressure ratio. A transient simulation is to be carried out.
- Conduct further simulations to examine the effects of other gas properties, such as viscosity and thermal conductivity, on the formation and location of Mach disk. This could help to refine existing correlations and provide a more complete understanding of the factors that influence Mach disk formation.
- Studying the downstream flow field beyond the Mach disk to better understand the processes of shock reflection and the development of complex flow structures. This could involve detailed numerical simulations of the entire flow field or experimental measurements using techniques such as particle image velocimetry (PIV) or laser Doppler velocimetry (LDV).
- Different mathematical presentations of the nozzle wall shape can further enhance the usability of the low-fidelity solver, using bi-objective or multi-objective optimisation techniques.
- Extending the optimisation method to incorporate additional design constraints, such as maximum pressure or temperature limits, in order to create nozzles suitable for specific applications.
- Investigating the potential for using the low-fidelity flow solver and optimisation method for other types of flow control devices or nozzle configurations in order to expand the scope and applicability of the approach.
- Using turbulence models such as Large Eddie Simulations (LES) to resolve the boundary layer near the nozzle wall and downstream flow.
- Studying the influence of upstream geometry with viscous simulation to understand the complexity of the flow field.
- Extend the current work to consider multi-dimensional nozzle designs, where the shape of the nozzle varies in both the radial and axial directions. This could provide a more flexible approach to nozzle design that allows for a greater degree of control over the flow characteristics.

- Investigate the effect of nozzle geometry on the transition from regular reflection to Mach reflection and the formation of Mach disk. This could involve studying a wider range of nozzle geometries and varying the shape of the nozzle and the pressure ratio to see how it affects the formation and location of Mach disk.
- Using Immersed Boundary Method (IBM) in performing the simulations of the ringed nozzle is suggested instead of constructing a complex mesh for each simulation.
- Design and optimisation of the ringed nozzle for specific applications, such as high-speed propulsion or scramjet engines, by considering various design parameters such as the number of rings, ring spacing, and ring height.
- Investigation of the effect of ring shape (e.g., circular, elliptical, or triangular) on the flow properties of the ringed nozzle and comparison with conventional contoured nozzles.
- Analysis of the acoustic properties of the ringed nozzle, including the generation of shock waves and noise reduction techniques, which could have important implications for applications such as supersonic aircraft or rocket propulsion.

APPENDIX A

Experimental Results

The jet produced by a nozzle constructed in graphite according to the optimisation procedure ($N1$) is investigated experimentally by Pitot probe measurements. Figure 7.1 shows the computational Mach number contour for the domain downstream of the nozzle exit, whereas Fig. 7.2.a shows a two-dimensional mapping of the Mach number extracted from total pressure measurements performed in an argon flow produced with 1720 hPa of stagnation pressure and 0.67 hPa back pressure in the expansion chamber, which creates an extremely underexpanded jet at the nozzle exit, and a stagnation temperature of 1300K. The forming shock waves coalesce downstream the nozzle exit leading to an incident shock and a total potential core with longitudinal extension of about 80 mm. It can be seen from Fig. 7.2.c that Mach number increases monotonically along the flow axis through the expansion from 10 to 16 upon exiting the nozzle till 33 mm downstream. Mach number then starts to decrease downstream under the action of the interfering oblique shock waves.
During our studies by cavity ring-down spectroscopy (CRDS)[42], the hypersonic jet was probed transversally at 20 mm (10 throat diameter) from the exit plane of nozzle $N1$, at a location where the extension of the isentropic core "IC" is maximum and the one of the unwanted shear layers is minimum, Fig. 7.3.a. These shear layers are formed by an inner part (shear layer 1 "SL1") induced by an incident shock located at 0.75 cm from the axis of the jet (Fig. 7.3.b), and an outer part beyond about 1 cm (shear layer 2 "SL2") and developing under the action of the static gas in the chamber. About 10% of methane is mixed to the initial flow of argon [42] and its rotation-vibration absorption lines are recorded in the infrared, as illustrated in panel c of Fig. 7.3. CRDS integrates the absorption signal along the line of sight through the cold isentropic core and the hotter shear layers (Fig. 7.3, panels a and b). These three spatial regions ("IC", "SL1", "SL2") contribute to the absorption spectrum additively, albeit differently, so that their respective associated temperatures, even rotational and translational (i.e. kinetic), can be tentatively determined [120]. The rotational temperature is extracted from the relative line intensities (line area), while the kinetic

temperature is extracted from the Full-Width at Half-Maximum (FWHM), (in cm^{-1}), of well isolated absorption lines, according to Eq. 7.1.

$$\Delta v(FWHM) = 7.162 \times 10^{-7} v_0 \sqrt{\frac{T}{M}} \tag{7.1}$$

Where v_0 is the line center (in cm^{-1}), T is the kinetic temperature, and M is the molar mass (in grams).

Panel c in Fig. 7.3 aims to explain the contribution of each flow region to the recorded spectral line shape. The isentropic core is characterized by a very cold rotational temperature which can be retrieved from the relative intensities of the methane absorption lines starting from the lowest rotation-vibration energy levels characterized by low J-values, where J is the quantum number related to the total angular momentum of the molecule. On the other hand, the hot gas in the shear layers is associated with transitions starting from higher J rotational levels that are more populated at high temperature. By way of illustration, an $R0$ line and clusters of $R3$ and $P9$ lines of methane are shown in Fig. 7.3.c. The intensity of the $R0$ line is dominated by the low temperature gas in the "IC" (blue curve), while the contribution of the isentropic gas to the higher J lines is found to be relatively small ($R3$ lines, blue curve) or even negligible ($R9$ lines, blue curve). As a result, rotational temperatures of 39 ± 5K and 375 ± 25K were extracted from the relative line intensities associated with low and high J-values, respectively. The former temperature characterizes the isentropic core, while the latter is associated with the shear layers. The small temperature uncertainty of $\pm$5K related to the isentropic core reflects its good radial uniformity (Fig. 7.3.b), while the larger uncertainty of $\pm$25K related to the peripheral layers can be explained by the large gradients relative to these specific zones (Fig. 7.3.b). Moreover, this rotational temperature of 375K must be considered as an average value of "SL1" and "SL2".

Regarding the kinetic temperatures, CFD calculations lead to a value as low as 16K for the

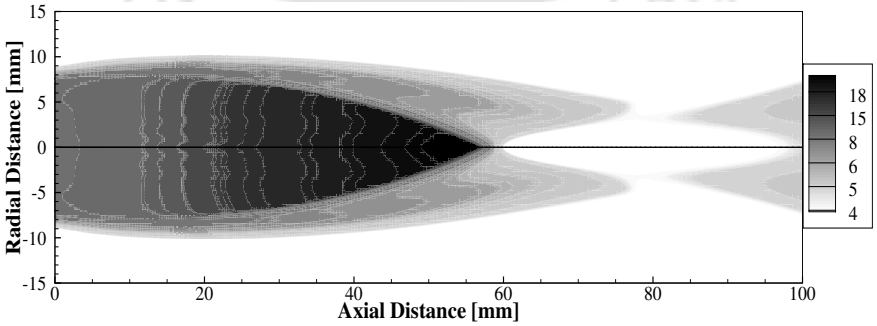

Figure 7.1: Computational Mach number contour for nozzle $N1$.

isentropic core of nozzle $N1$, which remains constant along the line of sight over a distance of approximatively 1.5 cm (Fig. 7.3.b). It should be noted that the non-negligible amount of methane added to argon during our experiments is probably responsible for a higher kinetic

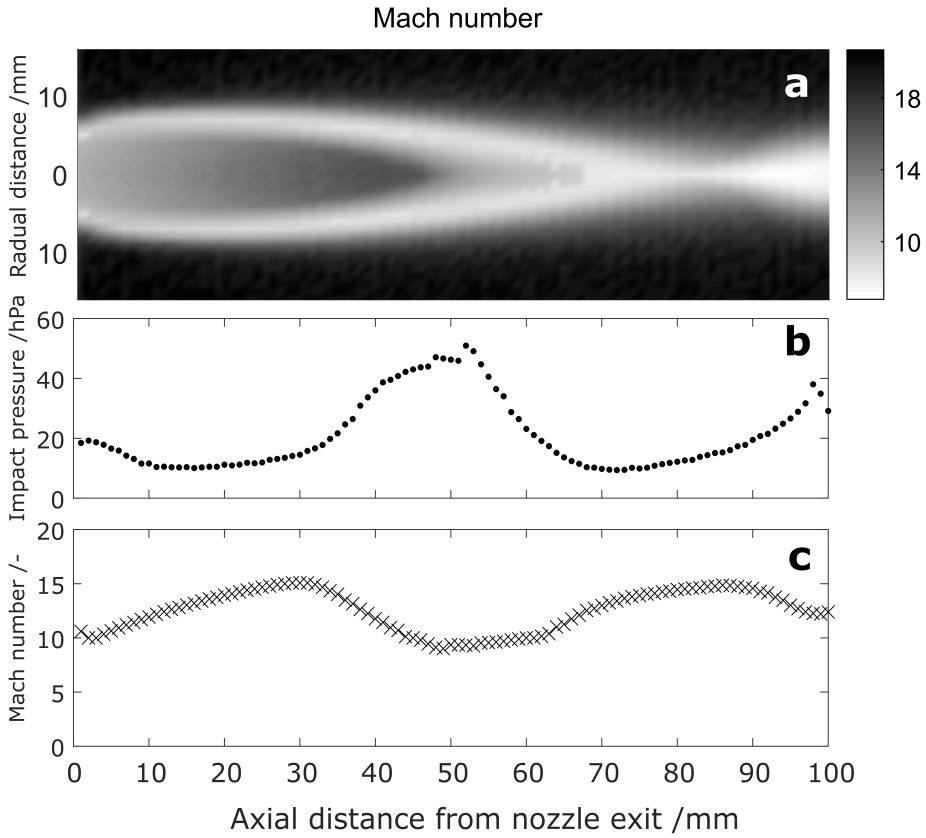

Figure 7.2: Axial evolution of flow properties through the domain downstream the nozzle exit.

temperature. Moreover, it is likely that the kinetic and rotational temperatures are not equilibrated (non-LTE conditions). Therefore, the actual kinetic temperature is probably between this value of 16K and the estimated rotational temperature of 39K. According to Eq. 7.1, such a low temperature of 16K should lead to a very narrow $R0$ line of 0.0043 cm^{-1} FWHM (orange line in Fig. 7.3.c), whereas the observed line is about twice broader with FWHM of 0.009 cm^{-1} (black line in Fig. 7.3.c). This cannot be explained solely by the Doppler effect related to the thermal agitation of the molecules, but must involve a convective Doppler effect related to the divergence of the flow streamlines [62]. Indeed, the Doppler line broadening of 0.009 cm^{-1} would correspond to an unrealistic kinetic temperature of 70K, thus much higher than the measured rotational temperature of 39K. In fact, the origin of this broadening is twofold; One must consider both a gas volume at a given kinetic temperature (16K according to the CFD calculations) and a radial expansion of the flow. The thermal and convective Doppler effects are cumulative and lead to the experimental FWHM line-width of 0.009 cm^{-1}. This is confirmed by our numerical simulation that considers the gas temperature, density and radial velocity along the line of sight, as displayed on panel c (red lines). As already mentioned, the $R0$ line is mainly sensitive to the contribution of "IC" flow and its FWHM can be almost reproduced by simply taking into account the simulation data

corresponding to the isentropic core flow region (blue line). However, in the case of the $R3$ three-line cluster, the "SL1" contributes the most to the absorption, while "IC" and "SL2" contribute to a lesser extent. Note that the central line is not perfectly reproduced, this is due to an additional absorption line of methane not present in the HITRAN database [121], from which all the spectroscopic data of the methane transitions are extracted. Finally, absorption lines with higher J quantum numbers (e.g. $P9$ lines shown in Fig. 7.3) are representative of the outermost "SL2" shear layer. They are much broader with a FWHM of 0.015 cm^{-1}. As shown in Fig. 7.3.b, the radial velocity in "SL2" is, on average, much lower than in the outer part of the isentropic core. Therefore, the line-width of the high J-value absorption lines is certainly less affected by the convective Doppler effect and should yield to a more reliable kinetic temperature by applying Eq. 7.1.

In short, each flow region can be investigated using transitions starting from different J

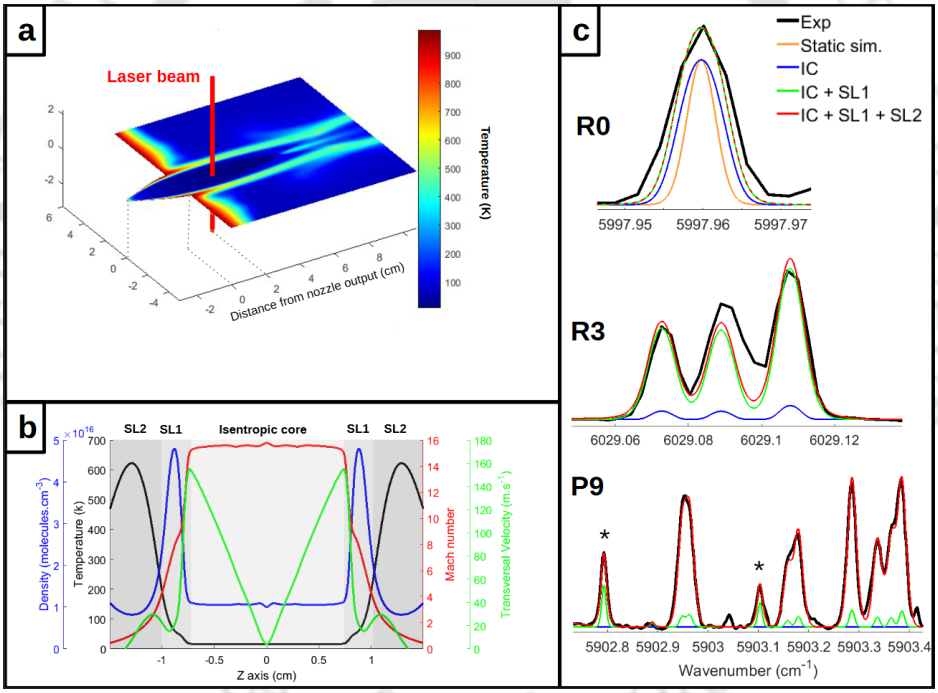

Figure 7.3: (a) CFD Temperature contour plot of nozzle $N1$ with laser beam located at 20 mm downstream from the nozzle exit plane. (b) Density, temperature, Mach number and radial velocity along the laser line of sight. (c) Observed (black) $R0$, $R3$ and $P9$ absorption lines of methane (lines topped by a star are not $P9$ lines), and their numerical simulation through the isentropic core (blue), through the isentropic core and the shear layer (green), and through all the different layers of the flow (red). The orange curve is a simulation of a static gas at 16K

.

rotational levels. A low J-value line is well suited to characterize the cold isentropic core which is associated with a progressively increasing transverse velocity producing a much broader line (Fig. 7.3.c, black curve) compared to its static counterpart (Fig. 7.3.c, orange curve). The shear layer can be investigated on the one hand by the line-shape of a medium

J-value transition like $R3$, in addition to the isentropic core, the narrower but denser inner shear layer "SL1" must be considered to reproduce the experimentally recorded line-shape (Fig. 7.3.c, green curve). On the other hand, CFD calculations reveal that the shape of high J-rotational lines, such as $P9$ lines, is mainly affected by the hotter outer shear layer "SL2". so that the entire absorption length (Fig. 7.3.c, red curve) is needed to reproduce the $P9$ transitions.

REFERENCES

[1] Donald H Levy. The spectroscopy of very cold gases. *Science*, 214(4518):263–269, 1981.

[2] Sonia Melandri, Gianni Maccaferri, Assimo Maris, Aldo Millemaggi, Walther Caminati, and Paolo G Favero. Observation of the rotational spectra of van der waals complexes by free jet absorption millimeter wave spectroscopy: pyridine-argon. *Chemical physics letters*, 261(3):267–271, 1996.

[3] Michael S Francis. Air vehicle management with integrated thrust-vector control. *AIAA Journal*, 56(12):4741–4751, 2018.

[4] Vladislav Emelyanov, Mikhail Yakovchuk, and Konstantin Volkov. Multiparameter optimization of thrust vector control with transverse injection of a supersonic underexpanded gas jet into a convergent divergent nozzle. *Energies*, 14(14):4359, 2021.

[5] R Balu, AG Marathe, PJ Paul, and HS Mukunda. Analysis of performance of a hot gas injection thrust vector controlsystem. *Journal of Propulsion and Power*, 7(4):580–585, 1991.

[6] Ashley M Korzun, Kelly J Murphy, and Karl T Edquist. Supersonic aerodynamic characteristics of blunt body trim tab configurations. In *31st AIAA Applied Aerodynamics Conference*, page 2809, 2013.

[7] Dong-Hyun Kim and In Lee. Transonic and low-supersonic aerodynamic analysis of a wing with underpylon/store. *Journal of Aircraft*, 37(1):189–192, 2000.

[8] Kelly J Murphy, Thomas J Horvath, Gary E Erickson, and Joseph M Green. Supersonic aerodynamic characteristics of proposed mars' 07 smart lander configurations. *Journal of spacecraft and rockets*, 43(2):282–292, 2006.

[9] GB Kistiakowsky and William P Slichter. A high intensity source for the molecular beam. part ii. experimental. *Review of Scientific Instruments*, 22(5):333–337, 1951.

[10] Terry A Miller. Chemistry and chemical intermediates in supersonic free jet expansions. *Science*, 223(4636):545–553, 1984.

[11] T C Jr Adamson and J A Nicholls. On the structure of jets from highly underexpanded nozzles into still air. *Journal of the Aerospace sciences*, 26(1):16–24, 1959.

[12] AL Addy. Effects of axisymmetric sonic nozzle geometry on mach disk characteristics. *AIAA Journal*, 19(1):121–122, 1981.

[13] AV Antsupov. Properties of underexpanded and overexpanded supersonic gas jets. *Soviet Physics Technical Physics*, 19:234, 1974.

[14] FS BILLIG, RC Orth, and M Lasky. A unified analysis of gaseous jet penetration. *AIAA journal*, 9(6):1048–1058, 1971. doi: 10.2514/3.49916.

[15] Harry Ashkenas and Frederick S Sherman. Structure and utilization of supersonic free jets in low density wind tunnels. *No. NASA-CR-60423*, 1965.

[16] S Crist, DR Glass, and PM Sherman. Study of the highly underexpanded sonic jet. *AIAA journal*, 4(1):68–71, 1966.

[17] D d'Ambrosio, LM De Socio, and G Gaffuri. Physical and numerical experiments on an under-expanded jet. *Meccanica*, 34(4):267–280, 1999.

[18] W Davidor and SS Penner. Shock standoff distances and mach-disk diameters in underexpanded sonic jets. *AIAA Journal*, 9(8):1651–1653, 1971.

[19] L D'attorre and F Harshbarger. Further experimental and theoretical studies of underexpanded jets near the mach disc. Technical report, General dynamics/Astronautics San Diego CA, 1964.

[20] L D'attorre and FC Harshbarger. Parameters affecting the normal shock location in underexpanded gas jets. *AIAA Journal*, 3(3):530–531, 1965. doi: 10.2514/3.2899.

[21] Richard Courant and Kurt Otto Friedrichs. *Supersonic flow and shock waves*, volume 21. Springer Science & Business Media, 1948.

[22] Benoit Andre, Thomas Castelain, and Christophe Bailly. Experimental exploration of underexpanded supersonic jets. *Shock Waves*, 24(1):21–32, 2014.

[23] Frank I Buckley Jr. Mach disk location in jets in co-flowing airstreams. *AIAA Journal*, 13(1):105–106, 1975.

[24] Irina A Graur, Tatiana G Elizarova, A Ramos, Guzman Tejeda, JM Fernandez, and Salvador Montero. A study of shock waves in expanding flows on the basis of spectroscopic experiments and quasi-gasdynamic equations. *Journal of Fluid Mechanics*, 504: 239–270, 2004.

[25] Andrea G Hsu, Ravi Srinivasan, Rodney DW Bowersox, and Simon W North. Molecular tagging using vibrationally excited nitric oxide in an underexpanded jet flowfield. *AIAA journal*, 47(11):2597–2604, 2009.

[26] Er-yun Chen, Gui-gao LE, Gai-ping ZHAO, et al. Numerical simulation of highly underexpanded axisymmetric jet with runge-kutta discontinuous galerkin finite element method. *Journal of Hydrodynamics, Ser. B*, 20(5):617–623, 2008.

[27] K Hatanaka and T Saito. Influence of nozzle geometry on underexpanded axisymmetric free jet characteristics. *Shock Waves*, 22(5):427–434, 2012.

[28] Guillaume Lehnasch and Pascal Bruel. A robust methodology for rans simulations of highly underexpanded jets. *International journal for numerical methods in fluids*, 56 (12):2179–2205, 2008.

[29] Alexey Velikorodny and Sergey Kudriakov. Numerical study of the near-field of highly underexpanded turbulent gas jets. *international journal of hydrogen energy*, 37(22): 17390–17399, 2012.

[30] Jennifer Wilkes, Christopher Glass, Paul Danehy, and Robert Nowak. Fluorescence imaging of underexpanded jets and comparison with cfd. In *44th AIAA Aerospace Sciences Meeting and Exhibit*, page 910, 2006.

[31] Richard T Driftmyer. A correlation of freejet data. *AIAA journal*, 10(8):1093–1095, 1972.

[32] Y Otobe, H Kashimura, S Matsuo, T Setoguchi, and H-D Kim. Influence of nozzle geometry on the near-field structure of a highly underexpanded sonic jet. *Journal of Fluids and Structures*, 24(2):281–293, 2008.

[33] DJ Carlson and CH Lewis. Normal shock location in underexpanded gas and gas-particle jets. *AIAA Journal*, 2(4):776–777, 1964.

[34] Eugene S Love, Carl E Grigsby, Louise P Lee, and Mildred J Woodling. *Experimental and theoretical studies of axisymmetric free jets*. US Government Printing Office, 1959.

[35] Vladimir Aniskin, Sergey Mironov, and Anatoliy Maslov. Investigation of the structure of supersonic nitrogen microjets. *Microfluidics and nanofluidics*, 14(3-4):605–614, 2013.

[36] VM Aniskin, AA Maslov, and SG Mironov. Effect of nozzle size on supersonic microjet length. *Technical Physics Letters*, 37(11):1046–1048, 2011.

[37] Erwin Franquet, Vincent Perrier, Stephane Gibout, and Pascal Bruel. Free underexpanded jets in a quiescent medium: A review. *Progress in Aerospace Sciences*, 77: 25–53, 2015.

[38] V So Avduevskii, AV Ivanov, I Mr Karpman, Vo D Traskovskii, and M Ya Yudelovich. Flow in supersonic viscous under expanded jet. *Fluid Dynamics*, 5(3):409–414, 1970.

[39] Yu P Finatev, LA Shcherbakov, and NM Gorskaya. Mach number distribution over the axis of supersonic underexpanded jets. *Journal of engineering physics*, 15(6):1153–1157, 1968.

[40] MJ Werle, DG Shaffer, and RT Driftmyer. Freejet terminal shocks. *AIAA Journal*, 8 (12):2295–2297, 1970.

[41] Ali Jraisheh, Jubajyoti Chutia, and Vinayak Kulkarni. Alteration in structure of underexpanded freejet through gas-dynamic perspective. *AIAA Journal*, pages 1–9, 2021.

[42] Eszter Dudas, Nicolas Suas-David, Shuvayan Brahmachary, Vinayak Kulkarni, Abdessamad Benidar, Samir Kassi, Christine Charles, and Robert Georges. High-temperature hypersonic laval nozzle for non-lte cavity ringdown spectroscopy. *The Journal of chemical physics*, 152(13):134201, 2020.

[43] Dean B Atkinson and Mark A Smith. Design and characterization of pulsed uniform supersonic expansions for chemical applications. *Review of scientific instruments*, 66 (9):4434–4446, 1995.

[44] J Seiner and T Norum. Experiments of shock associated noise of supersonic jets. In *12th Fluid and Plasma Dynamics Conference*, page 1526, 1979.

[45] J Seiner and T Norum. Aerodynamic aspects of shock containing jet plumes. In *6th Aeroacoustics Conference*, page 965, 1980.

[46] Michael Abbett. Mach disk in underexpanded exhaust plumes. *AIAA Journal*, 9(3): 512–514, 1971.

[47] AP Aleshin, IN Denisov, NM Rogachev, and VF Sivirkin. Effect of the cone angle and the degree of contraction of a sonic nozzle on the geometrical structure of the first roll of an underexpanded jet. *Journal of engineering physics*, 28(2):207–210, 1975.

[48] MMA Alam, T Setoguchi, S Matsuo, and HD Kim. Nozzle geometry variations on the discharge coefficient. *Propulsion and Power Research*, 5(1):22–33, 2016.

[49] V Chauhan, SM Aravindh Kumar, and E Rathakrishnan. Aspect ratio effect on elliptical sonic jet mixing. *The Aeronautical Journal*, 120(1230):1197–1214, 2016.

[50] N Menon and BW Skews. Effect of nozzle inlet geometry on underexpanded supersonic jet characteristics. In *Shock Waves*, pages 955–960. Springer, 2009.

[51] Fang Chen, Alexandre Allou, Quentin Douasbin, Laurent Selle, and Jean Denis Parisse. Influence of straight nozzle geometry on the supersonic under-expanded gas jets. *Nuclear Engineering and Design*, 339:92–104, 2018.

[52] Hadi Samsam-Khayani, Binqi Chen, Mirae Kim, and Kyung Chun Kim. Visualization of supersonic free jet flow structures subjected to various temperature and pressure ratio conditions. *Optics and Lasers in Engineering*, 158:107144, 2022.

[53] Kayane K Dingilian, Martina Lippe, Jakub Kubecka, Jan Krohn, Chenxi Li, Roope Halonen, Fatemeh Keshavarz, Bernhard Reischl, Theo Kurten, Hanna Vehkamaki, et al. New particle formation from the vapor phase: From barrier-controlled nucleation to the collisional limit. *The journal of physical chemistry letters*, 12:4593–4599, 2021.

[54] Shinobu Tanimura, Yensil Park, Andrew Amaya, Viraj Modak, and Barbara E Wyslouzil. Following heterogeneous nucleation of co 2 on h 2 o ice nanoparticles with microsecond resolution. *RSC advances*, 5(128):105537–105550, 2015.

[55] A Bonnamy, R Georges, A Benidar, J Boissoles, A Canosa, and BR Rowe. Infrared spectroscopy of (co 2) n nanoparticles (30< n< 14500) flowing in a uniform supersonic expansion. *The Journal of chemical physics*, 118(8):3612–3621, 2003.

[56] Yu Kudryavtsev, R Ferrer, Mark Huyse, Paul Van den Bergh, and Piet Van Duppen. The in-gas-jet laser ion source: Resonance ionization spectroscopy of radioactive atoms in supersonic gas jets. *Nuclear Instruments and Methods in Physics Research Section B: Beam Interactions with Materials and Atoms*, 297:7–22, 2013.

[57] Meryem Tizniti, Sebastien D Le Picard, Franccois Lique, Coralie Berteloite, Andre Canosa, Millard H Alexander, and Ian R Sims. The rate of the f + h 2 reaction at very low temperatures. *Nature chemistry*, 6(2):141–145, 2014.

[58] Ludovic Biennier, Sophie Carles, Daniel Cordier, Jean-Claude Guillemin, Sebastien D Le Picard, and Alexandre Faure. Low temperature reaction kinetics of cn-+ hc3n and implications for the growth of anions in titan's atmosphere. *Icarus*, 227:123–131, 2014.

[59] Alexey Potapov, Andre Canosa, Elena Jimenez, and Bertrand Rowe. Uniform supersonic chemical reactors: 30 years of astrochemical history and future challenges. *Angewandte Chemie International Edition*, 56(30):8618–8640, 2017.

[60] Niclas A West, Tom J Millar, Marie Van de Sande, Edward Rutter, Mark A Blitz, Leen Decin, and Dwayne E Heard. Measurements of low temperature rate coefficients for the reaction of ch with ch2o and application to dark cloud and agb stellar wind models. *The Astrophysical Journal*, 885(2):134, 2019.

[61] N Suas-David, S Thawoos, and AG Suits. A uniform flow–cavity ring-down spectrometer (uf-crds): A new setup for spectroscopy and kinetics at low temperature. *The Journal of chemical physics*, 151(24):244202, 2019.

[62] Andre Canosa, AJ Ocana, Maria Antinolo, Bernabe Ballesteros, Elena Jimenez, and J Albaladejo. Design and testing of temperature tunable de laval nozzles for applications in gas-phase reaction kinetics. *Experiments in Fluids*, 57(9):1–14, 2016.

[63] Srisha MV Rao and G Jagadeesh. Novel supersonic nozzles for mixing enhancement in supersonic ejectors. *Applied Thermal Engineering*, 71(1):62–71, 2014.

[64] Kennith L Goin and Alan Pope. High-speed wind tunnel testing(textbook on design, calibration and operation of near-sonic, transonic, supersonic and hypersonic wind tunnels). *NEW YORK, JOHN WILEY AND SONS, INC., 1965. 474 P*, 1965.

[65] H DANESHYAR. One-dimensional compressible flow(book). *Oxford, Pergamon Press, Ltd., 1976. 190 p*, 1976.

[66] John David Anderson and Mary L Bowden. *Introduction to flight*, volume 582. McGraw-Hill Higher Education New York, 2005.

[67] John David Anderson. *Modern compressible flow: with historical perspective*, volume 12. McGraw-Hill New York, 1990.

[68] Jie Wu and Tze How New. An investigation on supersonic bevelled nozzle jets. *Aerospace Science and Technology*, 63:278–293, 2017.

[69] N Lemos, N Lopes, JM Dias, and F Viola. Design and characterization of supersonic nozzles for wide focus laser-plasma interactions. *Review of Scientific Instruments*, 80 (10):103301, 2009.

[70] Karl Schmid and Laszlo Veisz. Supersonic gas jets for laser-plasma experiments. *Review of Scientific Instruments*, 83(5):053304, 2012.

[71] D Munday, E Gutmark, J Liu, and K Kailasanath. Flow structure and acoustics of supersonic jets from conical convergent-divergent nozzles. *Physics of Fluids*, 23(11): 116102, 2011.

[72] Jeffrey G Allman and Joe D Hoffman. Design of maximum thrust nozzle contours by direct optimization methods. *AIAA journal*, 19(6):750–751, 1981.

[73] Nan Yu, Yanni Yang, Renaud Jourdain, Mustapha Gourma, Adam Bennett, and Fengzhou Fang. Design and optimization of plasma jet nozzles based on computational fluid dynamics. *The International Journal of Advanced Manufacturing Technology*, pages 1–10, 2020.

[74] Hiroumi Tani and Tetsufumi Ohmaru. Hybrid continuum/rarefied flow simulations of plume interaction with full-sized spacecraft. *Journal of Spacecraft and Rockets*, pages 1–14, 2022.

[75] Kaikai Yu, Chong Chen, and Yile Chen. Inverse design of nozzle using convolutional neural network. *Journal of Spacecraft and Rockets*, pages 1–10, 2022.

[76] John Paul P, Prasanth P Nair, Abhilash Suryan, Joe Paul Martin M, and Heuy Dong Kim. Numerical simulation on optimization of pintle base shape in planar expansion-deflection nozzles. *Journal of Spacecraft and Rockets*, 57(3):539–548, 2020.

[77] Simon Bagy, Bijan Mohammadi, Michael Meheut, Mathieu Lallia, and Pascal Coat. Aerodynamic shape optimization of aircraft engine nozzles based on computer-aided design. In *AIAA Scitech 2020 Forum*, page 2247, 2020.

[78] Christopher Heath, Eric J Nielsen, Michael A Park, and Justin S Gray. Aerodynamic shape optimization of a two-stream supersonic plug nozzle. In *53rd AIAA Aerospace Sciences Meeting*, page 1047, 2015.

[79] GVR Rao. Exhaust nozzle contour for optimum thrust. *Journal of Jet Propulsion*, 28 (6):377–382, 1958.

[80] Dimitri Papamoschou and Anatol Roshko. Observations of supersonic free shear layers. *Sadhana*, 12(1):1–14, 1988.

[81] Anthony Demetriades and Timothy L Brower. Experimental study of transition in a compressible free shear layer. Technical report, Montana State University Bozeman Supersonic Wind Tunnedl Lab, 1982.

[82] Garry L Brown and Anatol Roshko. On density effects and large structure in turbulent mixing layers. *Journal of Fluid Mechanics*, 64(4):775–816, 1974.

[83] Paul E Dimotakis. Two-dimensional shear-layer entrainment. *AIAA journal*, 24(11): 1791–1796, 1986.

[84] Richard G Batt. Some measurements on the effect of tripping the two-dimensional shear layer. *AIAA Journal*, 13(2):245–247, 1975.

[85] DC Fourguette, MG Mungal, and RW Dibble. Time evolution of the shear layer of a supersonic axisymmetric jet. *AIAA journal*, 29(7):1123–1130, 1991.

[86] T Rossmann, M Mungal, and R Hanson. An experimental investigation of high compressibility non-reacting mixing layers. In *38th Aerospace Sciences Meeting and Exhibit*, page 663, 2000.

[87] Kai Ma, Jiang Li, Qiang Li, Yang Liu, Wen Ao, and Peijin Liu. Numerical and experimental investigation of the geometrical scale effect on a confined subsonic-supersonic shear layer. *Acta Astronautica*, 173:212–220, 2020.

[88] Kai Ma, Jiang Li, Qiang Li, and Yang Liu. Experimental study on evolution characteristics of plane subsonic-supersonic shear layer. *Aerospace Science and Technology*, 100:105791, 2020.

[89] TB Davis and Rajan Kumar. Shear layer characteristics of supersonic free and impinging jets. *Shock Waves*, 25(5):507–520, 2015.

[90] Arun Kumar Perumal and Ethirajan Rathakrishnan. Scaling law for supersonic core length in circular and elliptic free jets. *Physics of Fluids*, 33(5):051707, 2021.

[91] Nicolas Suas-David, Vinayak Kulkarni, Abdessamad Benidar, Samir Kassi, and Robert Georges. Line shape in a free-jet hypersonic expansion investigated by cavity ring-down spectroscopy and computational fluid dynamics. *Chemical Physics Letters*, 659:209–215, 2016.

[92] GVR Rao. Approximation of optimum thrust nozzle contours. *ARS J.*, 30:561, 1960.

[93] Hideaki Ogawa and Russell R Boyce. Nozzle design optimization for axisymmetric scramjets by using surrogate-assisted evolutionary algorithms. *Journal of Propulsion and Power*, 28(6):1324–1338, 2012.

[94] Shuvayan Brahmachary and Hideaki Ogawa. Multipoint design optimization of busemann-based intakes for scramjet-powered ascent flight. *Journal of Propulsion and Power*, pages 1–18, 2021.

[95] Shuvayan Brahmachary, Ganesh Natarajan, and Niranjan Sahoo. On maximum ballistic coefficient axisymmetric geometries in hypersonic flows. *Journal of Spacecraft and Rockets*, 55(2):518–522, 2017.

[96] Dmitry Davidenko, Yohann Eude, and François Falempin. Numerical study on the annular nozzle optimization for rocket application. In *16th AIAA/DLR/DGLR International Space Planes and Hypersonic Systems and Technologies Conference*, page 7390, 2009.

[97] A Mason and H Broadhurst. Monte carlo modeling of rocket motor multiple nozzle designs. In *28th Joint Propulsion Conference and Exhibit*, page 3356, 1992.

[98] R Parsley and K van Stelle. Altitude compensating nozzle evaluation. In *28th Joint Propulsion Conference and Exhibit*, page 3456, 1992.

[99] M Horn and S Fisher. Dual-bell altitude compensating nozzles. *NASA CR-194719*, pages 140–147, 1994.

[100] Daniel S Jones, Trong T Bui, and Joseph H Ruf. Proposed flight research of a dual-bell rocket nozzle using the nasa f-15 airplane. In *49th AIAA/ASME/SAE/ASEE Joint PropulsionConference*, page 3954. AIAA, 2013.

[101] Gary J Harloff and Gregory E Smith. Supersonic-inlet boundary-layer bleed flow. *AIAA journal*, 34(4):778–785, 1996.

[102] W Wong. The application of boundary layer suction to suppress strong shock-induced separation in supersonic inlets. In *10th Propulsion Conference*, page 1063, 1974.

[103] B Willis, D Davis, and W Hingst. Flow coefficient behavior for boundary layer bleed holes and slots. In *33rd aerospace sciences meeting and exhibit*, page 31, 1995.

[104] M Fukuda, Eli Reshotko, and W Hingst. Control of shock-wave boundary-layer interactions by bleed in supersonic mixed compression inlets. In *11th Propulsion Conference*, page 1182, 1975.

[105] A Weiss and H Olivier. Influence of boundary layer bleed slot width onto static and total pressure recovery of a shock train. In *30th International Symposium on Shock Waves 2*, pages 1205–1210. Springer, 2017.

[106] Ali Jraisheh, Eszter Dudas, Nicolas Suas-David, Robert Georges, and Vinayak Kulkarni. Low-fidelity approach for contoured nozzle design. *Journal of Spacecraft and Rockets*, pages 1–11, 2022.

[107] George B Arfken, Hans J Weber, and Frank E Harris. *Mathematical methods for physicists: a comprehensive guide*. Academic press, 2011.

[108] Bram Van Leer. Flux-vector splitting for the euler equations. In *Eighth International Conference on Numerical Methods in Fluid Dynamics: Proceedings of the Conference, Rheinisch-Westfälische Technische Hochschule Aachen, Germany, June 28–July 2, 1982*, pages 507–512. Springer, 2005.

[109] Meng-Sing Liou and Christopher J Steffen Jr. A new flux splitting scheme. *Journal of Computational physics*, 107(1):23–39, 1993.

[110] Sergei K Godunov et al. A finite difference method for the numerical computation of discontinuous solutions of the equations of fluid dynamics. *Mat. Sb*, 47(271-290):134, 1959.

[111] Jiri Blazek. *Computational fluid dynamics: principles and applications*. Butterworth-Heinemann, 2015.

[112] Mandeep Deka, Shuvayan Brahmachary, Ramakrishnan Thirumalaisamy, Amaresh Dalal, and Ganesh Natarajan. A new green–gauss reconstruction on unstructured meshes. part i: Gradient reconstruction. *Journal of Computational Physics*, 422: 108325, 2020.

[113] Gerard Liger-Belair, Daniel Cordier, and Robert Georges. Under-expanded supersonic co_2 freezing jets during champagne cork popping. *Science advances*, 5(9):eaav5528, 2019.

[114] John D Anderson Jr. *Hypersonic and high-temperature gas dynamics*. American Institute of Aeronautics and Astronautics, 2006.

[115] Jennifer L Palmer and Ronald K Hanson. Application of method of characteristics to underexpanded, freejet flows with vibrational nonequilibrium. *AIAA journal*, 36(2): 193–200, 1998.

[116] Yumiko Otobe, Shigeru Matsuo, Masanori Tanaka, Hideo Kashimura, and Toshiaki Setoguchi. A study on characteristics of under-expanded condensing jet. *JSME International Journal Series B Fluids and Thermal Engineering*, 49(4):1165–1172, 2006.

[117] Guzman Tejeda, Belen Mate, Jose Maria Fernandez-Sanchez, and Salvador Montero. Temperature and density mapping of supersonic jet expansions using linear raman spectroscopy. *Physical review letters*, 76(1):34, 1996.

[118] Donald E Wilcox, Alexander Weir Jr, James A Nicholls, and Roger Dunlap. Location of mach discs and diamonds supersonic air jets. *Journal of The Aeronautical Sciences*, 1957.

[119] John David Anderson and Mary L Bowden. *Introduction to flight*, volume 582. McGraw-Hill Higher Education New York, 2005.

[120] Robert Georges, Eszter Dudas, Nicolas Suas-David, and Lucile Rutkowski. Infrared absorption spectroscopy in laval nozzle supersonic flows. In *Uniform Supersonic Flows in Chemical Physics: Chemistry Close to Absolute Zero Studied Using the CRESU Method*, pages 479–538. World Scientific, 2022.

[121] IE Gordon, LS Rothman, RJ Hargreaves, R Hashemi, EV Karlovets, FM Skinner, EK Conway, C Hill, RV Kochanov, Y Tan, et al. The hitran2020 molecular spectroscopic database. *Journal of quantitative spectroscopy and radiative transfer*, 277: 107949, 2022.

Publications

Peer Reviewed Journals:

- Jraisheh A, Chutia J, and Kulkarni V. **Alteration in Structure of Underexpanded Freejet Through Gas-Dynamic Perspective**. *AIAA Journal*, 59.10: 3937-3945, (2021)
- Jraisheh A, Dudas E, Suas-David N, Georges R, and Kulkarni V. **Low Fidelity Approach for Contoured Nozzle Design**. *Journal of Spacecrafts and Rockets*, 60.2: 545-555 (2023)
- Jraisheh A, Chutia J, Benidar A and Kulkarni V. **Altitude Compensating Ringed Nozzle**. *Acta Astronautica* (Accepted)

Reputed Conferences:

- A. Jraisheh, and V.Kulkarni. Examining The Equivalence Between Sonic Free-Jet and The Supersonic Free-Jet, ***Proceedings of the 16th Asian Congress of Fluid Mechanics***, JNCASR, Bengaluru, India, 13-17 December, (2019)
- A. Jraisheh, and V.Kulkarni. Numerical Investigations towards the Near-Field Structure of a Sonic Orifice Jet, 25^{th} ***National and*** 3^{rd} ***International ISHMT-ASTFE Heat and Mass Transfer Conference (IHMTC-2019)***, IIT Roorkee, Uttarakhand, India, 28-31 December, (2019)
- A. Jraisheh, J. Chutia, A. Pathak, and V.Kulkarni. Laminar Shear Layer Growth in Supersonic Underexpanded Flows, ***Proceedings of the*** 9^{th} ***International and*** 49^{th} ***National Conference on Fluid Mechanics and Fluid Power (FMFP)***, IIT Roorkee, Uttarakhand, India, 14-16 December, (2022)
- A. Pathak, P. Khare, A. Jraisheh, and V.Kulkarni. Effect of upstream energy deposition on flow characteristics of a Scramjet engine, ***Proceedings of the*** 9^{th} ***International and*** 49^{th} ***National Conference on Fluid Mechanics and Fluid Power (FMFP)***, IIT Roorkee, Uttarakhand, India, 14-16 December, (2022)
- A. Jraisheh, J. Chutia, and V.Kulkarni. The Influence of Upstream Configuration on The Free Supersonic Nozzle Jet, ***Proceedings of NAPC-2022 National Aerospace Propulsion Conference***, IIT Bombay, Mumbai, India, 19-20 December, (2022)